ULTRAVIOLET-VISIBLE NANOPHOTONIC DEVICES

A DISSERTATION
SUBMITTED TO THE DEPARTMENT OF ELECTRICAL
AND ELECTRONICS ENGINEERING
AND THE INSTITUTE OF ENGINEERING AND SCIENCES
OF BİLKENT UNIVERSITY
IN PARTIAL FULFILLMENT OF THE REQUIREMENTS
FOR THE DEGREE OF
DOCTOR OF PHILOSOPHY

By
Bayram Bütün
July, 2010

I certify that I have read this thesis and that in my opinion it is fully adequate, in scope and in quality, as a dissertation for the degree of Doctor of Philosophy.

_____

Prof. Dr. Ekmel Özbay (Supervisor)

I certify that I have read this thesis and that in my opinion it is fully adequate, in scope and in quality, as a dissertation for the degree of Doctor of Philosophy.

_____

Prof. Dr. Levent Gürel

I certify that I have read this thesis and that in my opinion it is fully adequate, in scope and in quality, as a dissertation for the degree of Doctor of Philosophy.

_____

Assoc. Prof. Dr. Vakur B. Ertürk

I certify that I have read this thesis and that in my opinion it is fully adequate, in scope and in quality, as a dissertation for the degree of Doctor of Philosophy.

_____

Assist. Prof. Dr. Fatih Ömer İlday

I certify that I have read this thesis and that in my opinion it is fully adequate, in scope and in quality, as a dissertation for the degree of Doctor of Philosophy.

_____

Assoc. Prof. Dr. Hamza Kurt

Approved for the Institute of Engineering and Sciences:

_____

Prof. Dr. Levent Onural

Director of the Institute of Engineering and Sciences

ABSTRACT

ULTRAVIOLET-VISIBLE NANOPHOTONIC DEVICES

Bayram Bütün

Ph. D. in Department of Electrical and Electronics Engineering

Supervisor: Prof. Dr. Ekmel Özbay

July, 2010

Recently in semiconductor market, III-Nitride materials and devices are of much interest due to their mechanical strength, radiation resistance, working in the spectrum from visible down to the deep ultraviolet region and solar-blind device applications. These properties made them strongest candidates for space telecommunication, white light generation, high power lasers and laser pumping light emitting diodes. Since, like other semiconductors, there have been material quality related issues, ongoing research efforts are concentrated on growing high quality crystals and making low p-type ohmic contact. Also, in light emitting device applications, similar to the visible and infrared spectrum components, there are challenging issues like high extraction efficiency and controlled radiation. In this thesis, we worked on growth and characterizations of high quality (In,Al)GaN based semiconductors, fabricating high performance photodiodes and light emitting diodes. We studied different surface modifications and possibilities of obtaining light emitting diode pumped organic/inorganic hybrid laser sources.

Keywords: GaN, AlGaN, Photodiode, Light Emitting Diode, LED, Metal-organic Chemical Vapor Depositon, MOCVD, Photoluminescence, Organic polymer, MeLPPP.

ÖZET

MORÖTESİ-GÖRÜNÜR BÖLGE NANOFOTONİK AYGITLAR

Bayram Bütün

Elektrik ve Elektronik Mühendisliği Doktora

Tez yöneticisi: Prof. Dr. Ekmel Özbay

Temmuz, 2010

Sağlamlıkları, yüksek enerji radyasyonlarına dirençleri, morötesi dalgaboylarında çalışacak aygıtların üretimine olanak sağlaması gibi özelliklerinden dolayı III-Nitrat tabanlı malzeme sistemleri son yıllarda büyük ilgiyle araştırılmakta olan bir alan olmuştur. Üstün özellikleri sayesinde özellikle uzay uygulamalarında, morötesi aygıtların üretilmesinde, beyaz ışık oluşturulmasında, düşük dalgaboylarında yarıiletken lazer, ve lazer pompalama sistemlerinin geliştirilmesinde bu malzeme sistemleri üzerinde yoğun bir şekilde çalışılmaktadır. Diğer yarıiletken teknolojilerinde de karşılaşılan sürekli daha mükemmel kristal kalitesine sahip malzemenin büyütülmesi ve üretilmesi, özellikle AlGaN yapılarında karşılaşılan yüksek p-tipi Ohmik kontak kalitesi problemleri üzerinde yoğunlaşılmıştır. Buna ek olarak özellikle ışık saçan diyotlarda bulunan ışığın yapının dışına çıkarılması, halen değişik yöntemlerin denendiği bir çalışma konusudur. Bu tezde, yüksek kalitede nitrat tabanlı malzeme üretilmesi, bu malzemelerden yüksek performansa sahip fotodetektörler ve ışık kaynaklarının üretilmesi üzerinde çalışılmıştır. Buna ek olarak, diyotların üzerinde değişik yapılar üzerinde çalışılmış ve ışık saçan diyotla elektriksel olarak pompalanabilen inorganik/organik hybrid lazer sistemlerinin geliştirilmesi konusunda çalışmalar yapılmıştır.

Anahtar kelimeler: GaN, p-i-n, Fotodiyot, InGaN, fotoışıma, ışık saçan diyotlar, LED, Metal-organik kimyasal buhar yoğuşturması, MOCVD, organic polimer, MeLPPP

ACKNOWLEDGMENTS

It was my sheer luck and a privilege to be a graduate student of Ekmel Özbay, and being met with him is perhaps one of the few extraordinary incidences I have come across up to now. He said several times during my fellow co-workers' thesis defenses that, the relationship between a Ph.D. student and his advisor is only second to the relationship between a person and his wife. This was quite the case for me, perhaps more than anyone else in our more than ten years old research group. Whenever I lost my way in my research, many times, and in my he listened to me without judging, guided me and tried to make me solve my problems. He always took responsibility for ones under his guidance. Beside his academic curiosity, working discipline and unending motivation; I am always trying to imitate his pragmatist worldview, if I am not already mistaken for what this view means. Looking back now, I wish I produced much more original and complete work. This is my only regret which will always come back to me.

I would like to appreciate thesis monitoring process of Prof. Dr. Orhan Aytür and Assist. Prof. Dr. Fatih Ömer İlday. Both of them were truly inspiring although my interaction with them was not as long as I wished for. I want to thank Prof. Dr. Levent Gürel, Assoc. Prof. Dr. Vakur B. Ertürk and Assoc. Prof. Dr. Hamza Kurt very much for being in my jury.

There are numerous people I would like to mention in Bilkent community. I am grateful to department secretary Mürüvet Parlakay for her second-to-none patience, coolness, kindness and laughs. I feel so much happy for I am finishing my Ph.D. before she retires. I am sure she also feels the same.

I learned almost what I know about fabrication and measurement from the first members of Özbay Group; Necmi Bıyıklı, İbrahim Kimukin and Turgut Tut.

The Photonic Crystals and Metamaterials people, Mehmet Bayındır, Ertuğrul Çubukçu, Cömert Kural, İrfan Bulu, Koray Aydın and Hümeyra Çağlayan inspired us, detector group, for publishing more and more papers.

M. Deniz Çalışkan, my office mate, deserves special thanks for his kindness, benevolence, very practical and wide electronics experience. Almost every day, I have been learning something from him.

I would like to thank Dr. Mutlu Gökkavas for all his helps. I also learned a lot from his step-by-step reasoning and "better be safe than sorry" experimentalist approach. I also thank İ. Evrim Çolak, Serkan Bütün, Neval Yılmaz, Erkin Ülker and Tolga Yelboğa for their friendship and helps. Our secretaries Gamze Seğmenoğlu and Nursel Aşıcı were always very kind and helpful. Past and present members of NANOTAM and Özbay Group were always helpful and kind, I appreciate all their efforts and assistance.

Contents

List of Figures

List of Tables

Chapter 1

Introduction

Our everyday life is surrounded by state-of-art semiconductor based components and devices. From televisions and full-color displays to our laptops, from our cars to our mobile phones, we are using light emitting diodes (LEDs), photodetectors (PDs), modulators, laser diodes (LDs), and almost all kinds of other optoelectronic devices every now and then. The Internet has been growing very fast since the 1990s, thanks to the rapid advancements in these semiconductor devices and, of course, fiber-optic cables. There have been huge research and industry efforts put forth into making all these devices smaller, more energy efficient, and with increasingly more functionalities. These efforts are now paying back. Today, the worldwide telecommunications industry revenue is approx. $3.85 trillion [1], and the estimated annual growth rate is approx. 10%. In addition to this, the driving force of the defense industry should not be underestimated because it is one of the major contributors to research funding worldwide.

When we speak about smaller and more efficient devices, nanotechnology comes into the picture immediately, because it is the enabling technology today. It is counted among one of the most important technological breakthroughs recently,

which has the potential to change how we live, similar to how silicon and the Internet did in the past. It is possible to manufacture nanometer size features on LEDs and PDs easily, and fabricate nanometer size LDs. It enables to exploit novel phenomena in a more controllable manner, compared to the microfabrication techniques. Devices, fabricated with nanotechnological means, are smaller and more efficient because the material properties are controlled and manipulated almost at the molecular level, and the surface effects become more important than bulk properties. Having submicron or sub-100 nm features, nanophotonic devices employ, for example, nano-plasmonics (coupled modes of photons and electron oscillations in dielectric/metal interfaces) and nano-photonic crystals (periodic nanostructures for photons, similar to semiconductor crystals for electrons). They are integrated into semiconductor photonic devices.

"In the ongoing development and application of new technologies, every so often there appears a fundamental technology that can shift the way the world operates. The development of silicon semiconductor materials, which enabled transistors, integrated circuits, microprocessors, the computer, and the information age, has influenced virtually every aspect of modern life. In a similar manner, III-Nitride (III-N) semiconductor materials are poised in such a way to fundamentally change our lives. These materials, which include aluminum nitride (AlN), gallium nitride (GaN), and indium nitride (InN), will enable new capabilities in semiconductor devices and will make the reinvention of existing technologies possible. While there are many possible and even likely applications for these materials, their impact over the next decade will focus on two main applications: light generation and the control of electrical power" [2].

Group III – Nitrides (GaN, AlN, InN) have undergone decades of surprises [3]; from the initial breakthroughs (metal-organic chemical vapor deposition growth of nucleation/buffer layers and achieving reliable p-type doping) with visible LEDs to LDs, solar-blind ultraviolet (UV) PDs to microwave power electronics, and then to solid-state UV light sources and white lighting. Today, nitride based LEDs have

found applications in displays, lighting, indicator lights, advertisements, and traffic signs. Nitride based UV LDs are the most important component of high density optical read and write technologies. Solar-blind UV sensors that operate in the solar blind region (below ~290 nm) have found very critical applications, such as ozone layer and environmental monitoring, or military applications such as missile warning [4].

Recently, the band gap of InN was determined to be closer to 0.7 eV rather than the value of 1.9 eV that has been accepted for many years, extending the spectrum coverage of this material system from 200 nm up to 1.7 μm.[5] Along with high electron mobility, direct band gap, material hardness, and radiation resistance, nitrides are believed to be the most important semiconductors in recent modern technology, after silicon. Its future looks even brighter as we see the advances towards solid-state lighting and high-power electronics applications. In Science Citation Index (SCI) journals, the number of papers published annually on nitrides reached the level of gallium arsenide (GaAs) related papers, as can be seen in Figure 1.1.

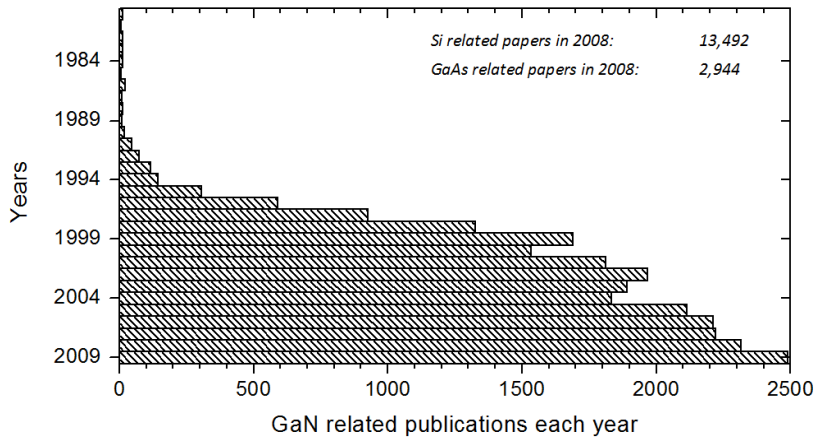

Figure 1.1: GaN related SCI publications from 1980 to 2009, from Thomson Reuters ISIKnowledge [6].

GaN crystals were grown by Johnson et al. in 1932, who passed ammonia over very hot gallium [7]. By this method, small platelets were produced randomly over the gallium [8]. Then, almost in each decade thereafter there were growth trials for GaN crystals with small successes. There has been one extreme trial, for example, conducted in an empty missile capsule with an explosion to reach the very high temperatures that are necessary for crystallization. Today, the mass production of III-Nitrides is realized by metal-organic chemical vapor deposition (MOCVD) systems with very high quality.

A noteworthy example of scientific persistence took place in the 1990s that was related to nitride research. Efforts to grow high quality p-type nitride ceased because of an enormous number of trials and no satisfactory results. At that time, arsenide and phosphorus based semiconductors were providing red-yellow-green light and there was a need for true blue emission. The only candidates were SiC, which has already been abandoned due to its indirect band gap and low efficiency, and GaN. S. Nakamura, who was then at Nichia Laboratories, was working to grow p-type GaN, employing thermally activated magnesium as an acceptor, and InN/GaN quantum wells for efficient electron-photon conversion. He was successful in fabricating high efficiency blue and UV LEDs and LDs. As can be seen in Figure 1.2, his several published papers opened the door to today's rush to conduct nitride research.

Today, more than 20% of all world energy consumption is due to lighting, mostly from incandescent and fluorescent lighting. It is expected that III-Nitrides-based LEDs might replace traditional light bulbs and fluorescent lights in order to realize a revolution in lighting and change all of human life in this century, similar to Edison's invention of the electric light bulb more than one-hundred year ago [9].

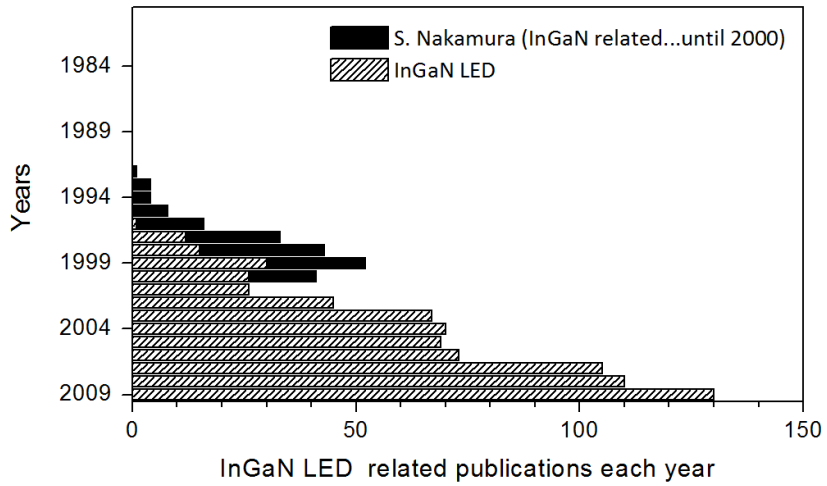

Figure 1.2: InGaN light-emitting diode related publications [6]. No publications before 1992.

In the present thesis, we studied highly efficient PDs and LEDs with optimized performances starting from material growth. There has been an inherent challenge here, ever since the first fabricated LED, in extracting light from light emitters due to the total internal reflection and self-absorption. In the literature today, there are non-stop efforts put forth to maximize the external efficiency of light emitters by numerous methods. Here, we worked on fabricating nanophotonic features utilizing plasmonic and photonic crystal phenomena for efficient light extraction.

In Chapter 2, the properties of III-Nitrides and the basic theory of semiconductor detectors and light emitting devices are given, which is essential for the later chapters and our motivation.

In Chapter 3, the microfabrication of PDs and LEDs in NANOTAM clean rooms will be presented with the basic processing steps.

In Chapter 4, devices' further nanolithography processes and performance measurements will be presented. This chapter contains GaN based photodetectors, InGaN based light emitting diodes with plasmonic nanoparticles, and pillar structures

for light extraction from LEDs. The last part of this chapter consists of hybrid light emitting device studies containing InGaN based LEDs and conjugated polymer based 2D circular waveguide and gain region.

The appendix contains MATLAB code for the TMM analysis of one dimensional periodic dielectric structures.

Chapter 2

Theory of Semiconductor Detectors and Light Sources

In this chapter, properties of GaN based semiconductors will be summarized. Electrical and optical parameters of GaN, $In_xGa_{1-x}N$ and $Al_xGa_{1-x}N$ compounds which are subject to our work will be given. Then, basic operating principles of semiconductor detectors and designs of our structures, focusing especially on p-i-n type diodes, will be explained.

In Figure 2.1, the part of the periodic table is shown which consists of elements in current semiconductor world. In our research, we have worked with (Al,Ga,In)-N binaries and $Al_xGa_{1-x}N$ and $In_xGa_{1-x}N$ ternaries as shown in Figure 2.2. The elements Mg and Si are used as p- and n-type dopants respectively in III-Nitride growths.

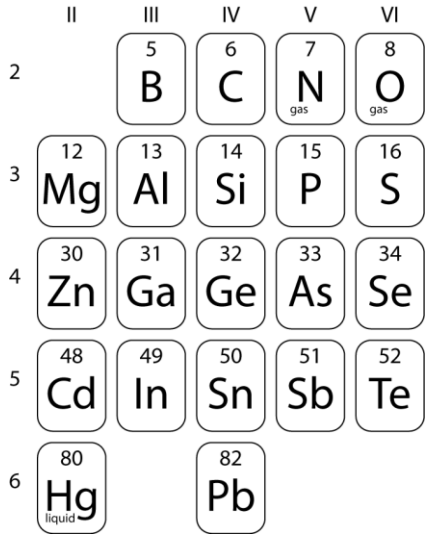

Figure 2.1: Part of the periodic table related to the semiconductors. All these elements, except N, O and Hg, are solid at room temperature.

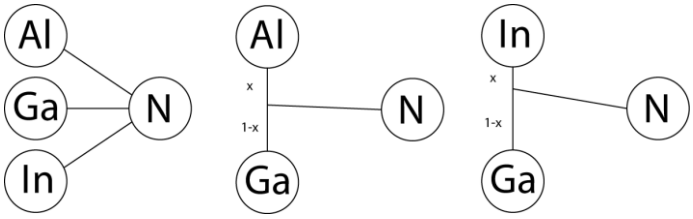

Figure 2.2: The semiconductor binary and ternary compounds used in current work.

Usually, undesirable and unintentional impurities would incorporate into the structures, such as C, N,O, Si and Mg, coming from the previously grown structures' pollution. Their effect would be lower resistivity of otherwise intrinsic layers (high dark current and noise) in photodiodes, and extra peaks, spreading of spectrum in light emitting diodes and lasers. Since our work in light emitters is related to the direct bandgap materials (all nitrides are direct bandgap, see Figure 2.3), we are not interested in impurity related transitions to increase efficiency of devices, like GaP related ternary light emitting diodes. Therefore, we try to prevent these impurities

during the growths but in any case these impurities are corporated into the devices, due to successive growths of different structures, imperfect vacuuming and deposited residues in chamber. It is possible to see these impurities and dopants in low temperature photoluminescence measurements, because all of them have distinct energy levels in nitride semiconductors.

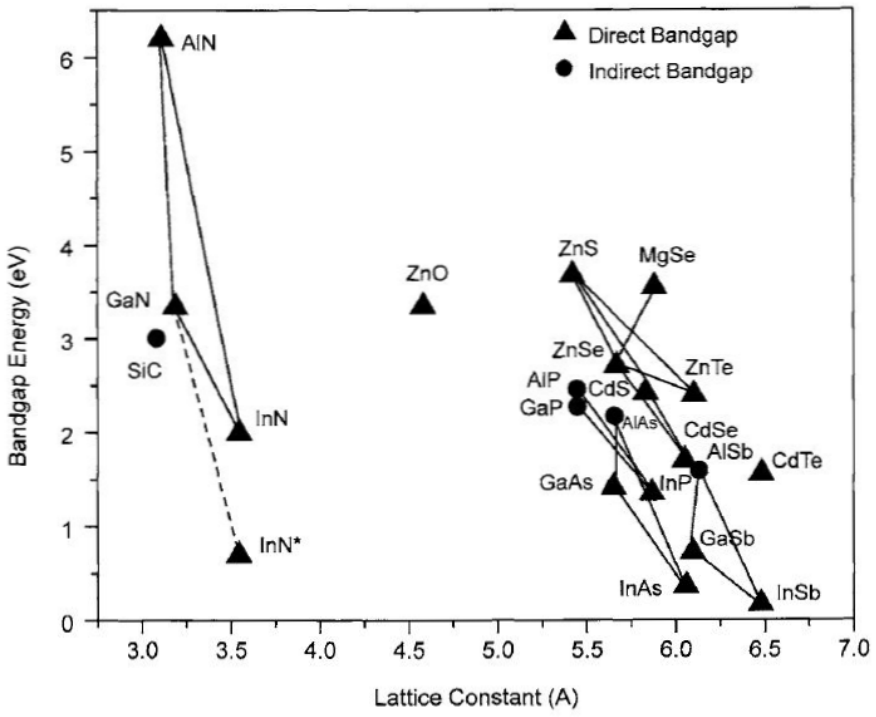

Figure 2.3: Bandgap energy versus lattice constant of various semiconductors, including III-nitrides. The bandgap energy of InN was recently reported to be 0.7 eV (after [10]).

Bandgap line-ups of different nitride compounds are given in Figure 2.4. Although these values are important and used in analyzing heterostructures, without considering spontaneous piezoelectric fields they are almost useless. These fields

considerably disturb band diagrams [11]. Considering these effects, recommended valence band offset values are given in Table 2.1.

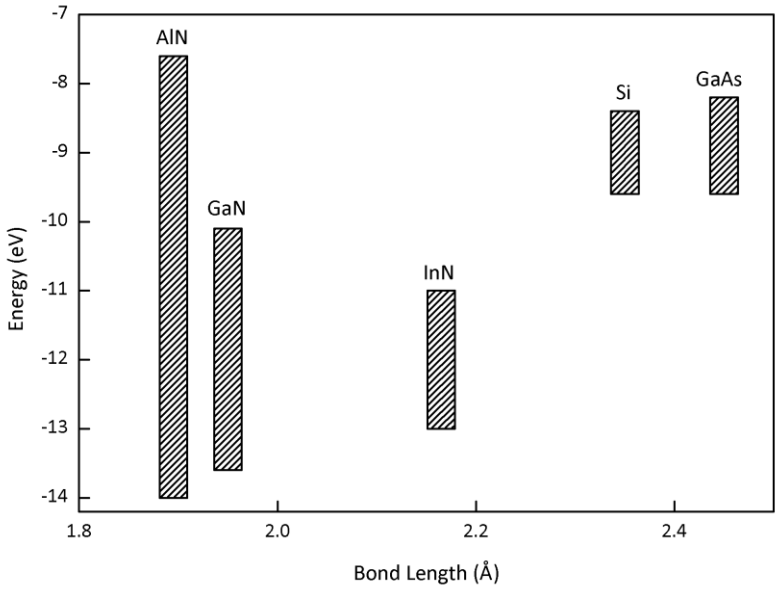

Figure 2.4: Band line-ups of several bulk compound semiconductors [12,13].

Heterojunction	VBO (eV)
AlN/GaN (0001)	-0.20
GaN/AlN(0001)	0.85
InN/GaN (0001)	0.50
GaN/InN(0001)	-0.50

Table 2.1: Recommended valence-band offsets (including strain and polarization effects) for the various binary wurtzite interface combinations. A positive VBO corresponds to higher valence band maximum in the first material than in the second (after [14]).

2.1 Properties of GaN based Semiconductors

GaN based materials are high bandgap materials, which means working from visible to deep ultraviolet spectrum region. Material properties of AlN, GaN and InN are given in Table 2.2. Wavelength span starts about 200 nm up to near infrared region, covering almost all visible spectrum. This is one of the most important properties of nitrides. In addition they are very resistant to radiation damages.

	AlN	GaN	InN
E_g (eV) at 300 K	6.2	3.44	1.93
λ (nm)	200	360	1770 (643)
Lattice constant, a (Å)	3.112	3.189	3.545
Lattice constant, c (Å)	4.982	5.186	5.703
Lattice Mismatch with GaN (%) $(a_{GaN}-a_{sub})/a_{sub}$	2.47	0	-9.82
Electron Eff. Mass, m_e	0.4*	0.2	0.11
Hole Eff. Mass, m_h	3.53(m_{hhz})10.42 (m_{hhx}) 3.53 (m_{lhz})0.24 (m_{lhx}) †	0.8	0.5 (m_{hh}) 0.17 (m_{lh})
Refractive Index, n	2.2 (0.60 µm) 2.5 (0.23 µm)	2.35 (1.0 µm) 2.60 (0.38 µm)	2.56 (1.0 µm) 3.12 (0.66 µm)
ε(0)	9.14	10.4 (E‖c) 9.5 (E_I_c)	
ε(∞)	4.84	5.8 (E‖c) 5.4 (E_I_c)	9.3
Melting Point (°C)	3000	>1700	1100
Thermal Conductivity κ (W/cm K), (Al_2O_3:0.3)	2.0	1.7-1.8	4.9

Table 2.2: Physical properties of III-Nitride materials [10]. AlN electron effective mass (*) is from [15], hole effective masses (†) are from [16].

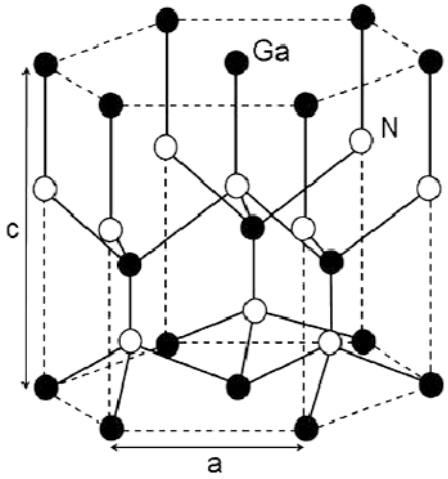

Figure 2.5: Crystal structure of wurtzite GaN (c-plane, 0001).

In Figure 2.5, the crystal structure of GaN and related materials is given. Here, due to the Ga-N and N-Ga bond nonsymmetry on c-plane, this crystal suffers from strong piezoelectric fields on compound interfaces, heterostructures and quantum wells.

2.2 Semiconductor Detectors

2.2.1 Basics

In this part, operation of a p-i-n photodiode will be presented. Then Transfer Matrix Method (TMM), which is used at epitaxial design and antireflection coating steps will be explained. In the last section, design of photodetector together with material properties will be described [17].

Photodetectors can be broadly defined as devices that measure optical power by converting the energy of the absorbed photons into a measurable form [18], [19]. Generally, output of the detector is an electrical signal in response to or as a replica of the input light signal [19]. They are the key elements in virtually any optoelectronic system and application, paralleling in importance the role of sources [19]. Detectors can be classified according to the generation of electrical output

signal as thermal detectors and photoelectric detectors. Thermal detectors operate using the heat generated by the photon absorbed by the detector material. Since temperature change requires much longer times comparing the absorption effect, and involvement of phonon interactions, this kind of detectors, such as thermocouples, bolometers, pyroelectrics are rather inefficient and relatively slow. The operation of photoelectric detectors is based on the photoeffect, in which the absorption of photons by the material results mobile charge carriers, namely electrons and holes. Under the effect of electric field, generated by material itself, or by an outside bias voltage, these carriers are transported and a measurable electric current is generated. In other words, the photodetection process can be schematized by the following sequence [19]:

1. Absorption of photons resulting the generation of charge carriers,
2. Drift of charge carriers under a suitable internal electric field,
3. Collection of carriers through the ohmic contacts by external circuit.

2.2.2 Design and Structures

A photodiode is basically a p-n junction operated under reverse bias. Depending on the junction type, p-i-n photodiode is a member of diode family that includes p-n junction diode, p-i-n diode, metal-semiconductor diode, and heterojunction diode [20]. This classification is based on the junction types forming the diode.

The p-i-n photodiode is one of the most common photodetectors, because the depletion region thickness can be engineered to optimize the quantum efficiency (QE) and the frequency response. Figure 2.6 shows the structure of a basic diode and energy-band diagram. An intrinsic layer is stacked between p and n layers. If the intrinsic layer is depleted completely with reverse bias, photogenerated carriers are separated by electric field and they contribute to the external current if they can reach to the ohmic contacts. Speed of the devices, here, depends on the transportation of the carriers from the far edge, n contact for holes and p side for electrons, for example. However, if the light is also absorbed inside p and n regions, another component comes into the picture, which is diffusion current. Diffusion current may

slow down the device considerably, depending on the lifetime of the photogenerated carriers, with tens of nanoseconds [20], [21] in GaAs, for example. This drawback can be eliminated by allowing absorption only in the i-region, by using heterojunctions. So there is no diffusion related contribution to the output current. Therefore, with heterojunction p-i-n photodiodes, high efficiency and high speeds can be achieved at the same time.

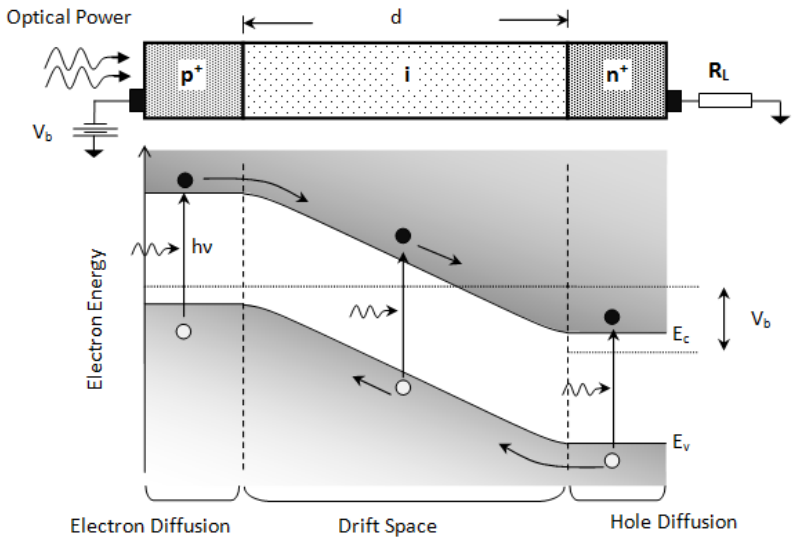

Figure 2.6: Diode structure and energy band diagram under reverse bias.

The advantages of the p-i-n photodiode over the p-n junctions are as follows: [19]

1) The thickness of the absorption region is determined by the geometry of the device, independently from V_b, which has very little effect on the spectral response. Therefore, even with low bias, a good efficiency can be obtained.

2) With depletion region in i-region much longer than depletion regions at p+ and n+, the diffusion contributions can be kept small, which can be

achieved via doping concentrations. Thus, we can obtain the frequency response independent of λ.

3) Since electric field, E, is constant in the active layer, the intrinsic speed of response (i.e. overall drift time for photogenerated carriers) is optimized.

When reverse bias is applied to the device, as shown in Figure 2.7, intrinsic layer will have a continuous and constant electric field. When an optical input at a wavelength λ (corresponding to a photon energy hν higher than the bandgap of the material) reaches to the depletion region, electron hole pairs are generated. The carriers are swept away by electric field; electrons moving towards n- contact, and holes moving to p- contact. Transport of the carriers induces an output current, I_{out}, at the terminals of the device. The number of electrons generated per incident photon is defined as the quantum efficiency, η [20]:

$$\eta = \frac{I_p / q}{P_{opt} / h\nu} \tag{2.1}$$

where, I_p is the current generated by absorption of incident photons, P_{opt} is the optical power at a wavelength of λ (corresponding to a photon energy of hν).

Another figure of merit of a photodiode is the responsivity, $\Re$, which is the ratio of the photogenerated current to the optical power:

$$\Re = \frac{I_p}{P_{opt}} = \frac{\eta q}{h\nu} = \frac{\eta\lambda(\mu m)}{1.24}(A/W) \tag{2.2}$$

Assume that, at $t = 0$, a narrow optical pulse generates carriers with a total charge of q, at a distance x_0, from p- contact.

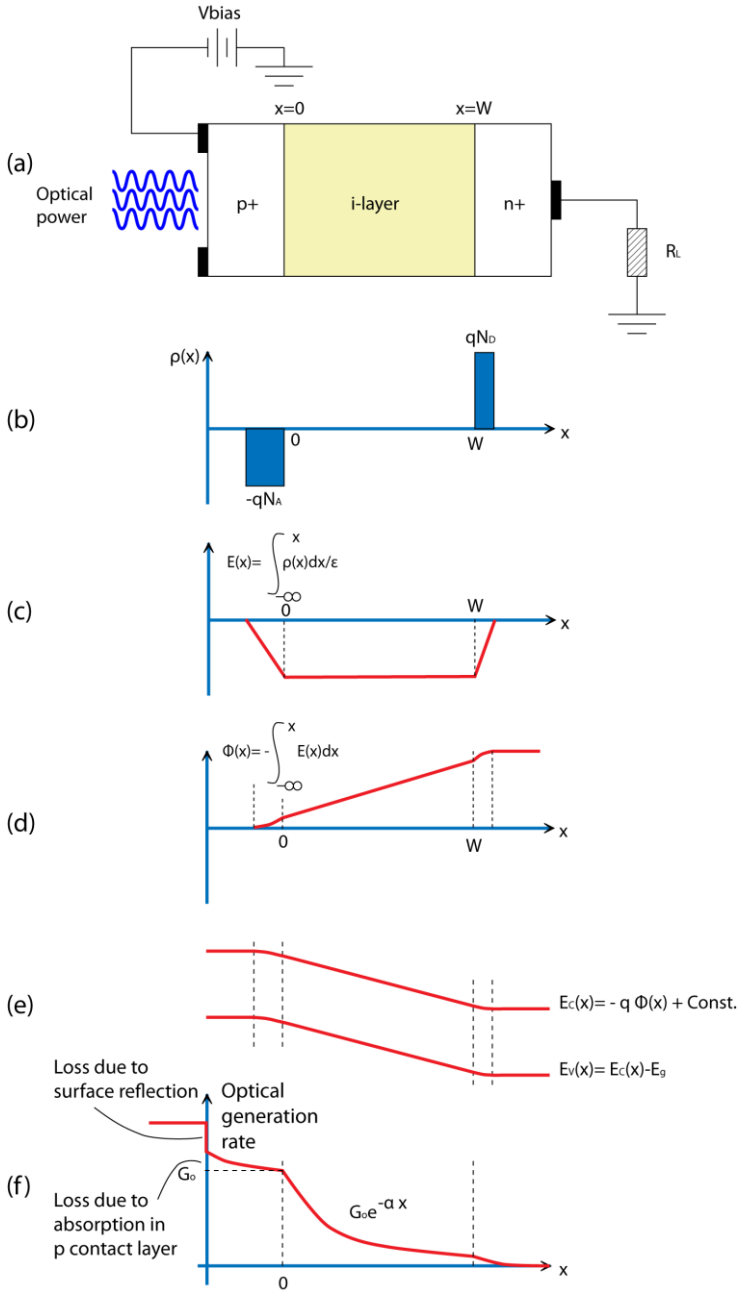

Figure 2.7: (a) A p-i-n photodiode under optical illumination from the p-side, (b) the charge density ρ(x) under depletion approximation, (c) the static electric field profile E(x), (d) the electrostatic potential Φ(x), (e) the conduction and valence band edge profiles, and (f) the optical generation rate G(x) within the i-region, including the losses from the surface reflection and absorption loss in the p-region (adapted from [22]).

Due to electric field in depletion region, positive and negative sheet of charges, with surface charge density $\sigma = q/A$, are forced to move in opposite directions, with velocities v_h and v_e, respectively. Each sheet contributes to the electric field formed between sheets:

$$E_\sigma = \frac{\sigma}{\varepsilon} = \frac{q}{A\varepsilon} \tag{2.3}$$

where ε is dielectric constant of the semiconductor. Direction of this extra electric field is opposite to the depletion region electric field, which results in a voltage drop across the depletion layer, as the sheets move away from each other [23]. This voltage drop can be expressed as:

$$V_\sigma(t) = \int_{x_h(t)}^{x_e(t)} E_\sigma dx = E_\sigma[x_e(t) - x_h(t)] \tag{2.4}$$

where $x_e(t)$ and $x_h(t)$ are the time dependent coordinates of the sheets. These coordinates can be expressed as:

$$x_e(t) = x_0 + v_e t \qquad 0 < t < t_e \tag{2.5}$$

$$x_h(t) = x_0 - v_h t \qquad 0 < t < t_h \tag{2.6}$$

where $t_e = (d - x_0)/v_e$ and $t_h = x_0/v_h$ are electron and hole transit time. Assuming $t_e > t_h$, we can write time dependent voltage drop as:

$$V_\sigma = \begin{cases} \dfrac{\sigma}{\varepsilon}(v_e + v_h)t & ,0 < t < t_h \\ \dfrac{\sigma}{\varepsilon} v_e t & ,t_h < t < t_e \end{cases} \tag{2.7}$$

We can write the output current $I_{out}(t)$ as:

$$I_{out}(t) = \frac{dQ(t)}{dt} = \frac{d}{dt}\left[CV(t)\right] \tag{2.8}$$

Here, $C = \varepsilon A/d$, which is independent of bias voltage for a p-i-n diode, and $V(t) = V_0 - V_\sigma(t)$, then time dependent current is:

$$I_{out}(t) = \begin{cases} I_1 = \dfrac{q}{d}(v_e + v_h) & ,0 < t < t_h \\ I_2 = \dfrac{q}{d} v_e & ,t_h < t < t_e \end{cases} \tag{2.9}$$

This expression is plotted in Figure 2.8.

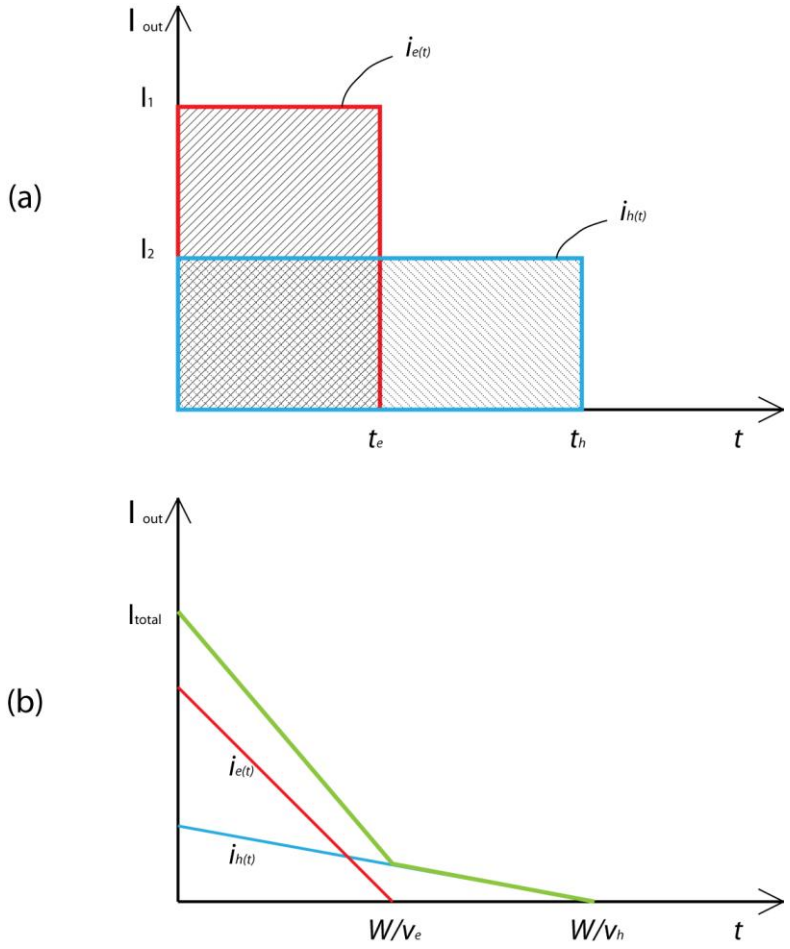

Figure 2.8: (a) The induced current as a function of time, where photogeneration took place only at sheet in the active region. (b) Output current for uniformly illuminated diode, where electron drift velocity is larger than hole drift velocity.

The performance of photodetectors that are investigated in this work are efficiency and speed. Quantum efficiency of a detector, in which light partly transmits from the front surface and passes through the active layer once, is expressed as:

$$\eta = (1-R)(1-e^{-\alpha d}) \tag{2.10}$$

where R is the reflectivity of the front surface, α is the absorption coefficient, and d is the thickness that light travels in the region which absorbs. Looking to this equation, the ways to maximize efficiency are minimizing surface reflection, increasing layer thickness or playing with material to change absorption coefficient, or the effective absorption coefficient.

Another figure of merit is the bandwidth, or equivalently speed, of the diodes. The factors which limits the speed are transit time of the carriers and RC time constant of the photodiode, which results from intrinsic nature of material and structure of the device.

Photodiode can be electrically modeled as in Figure 2.9.

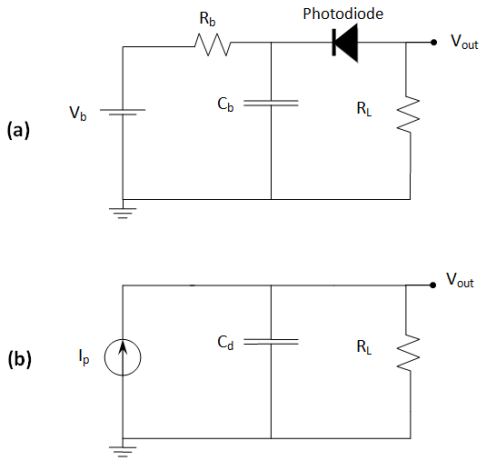

Figure 2.9: Schematics of photodiode circuitry under reverse bias (a) and equivalent high speed model for frequency analysis (b).

For transit time limited case, the -3 dB frequency can be expressed as:

$$f_{tr} = 0.45\frac{v_e}{d} \tag{2.11}$$

For the RC limited case, same frequency is expressed as:

$$f_{RC} = \frac{1}{2\pi R_L C_d} \tag{2.12}$$

For continuing to the growth and fabrication of diodes, it necessary to use a simulation method for structures. We used transfer matrix method (TMM), which provides a simple technique to calculate electric field distribution, transmission, reflecton and absorption in the epitaxial structures. However, this method requires some assumptions, and idealizes the structure. Interfaces are assumed to be completely flat, which is not always the case in semiconductor growth techniques. Materials are assumed to be defect free, so that extra scattering factors within the structure are omitted.

We can think successive layers as repetition of two basic building blocks. First one is an interface of two different mediums, Figure 2.10, and second is a homogeneous slab of one material, Figure 2.11. Simulation method simply combines these two and repeats the procedure for each successive layer.

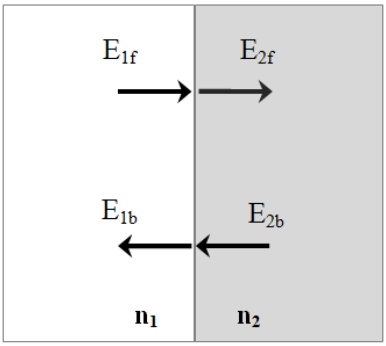

Figure 2.10: First building block of optical multilayer films; electric field is transferred from one side of a boundary to the other side.

Using continuity of electric and magnetic fields, electric fields at the left and right of any interface can be expressed as follows:

$$\begin{pmatrix} \mathrm{E}_{1\mathrm{f}} \\ \mathrm{E}_{1\mathrm{b}} \end{pmatrix} = \frac{1}{t_1}\begin{pmatrix} 1 & r_1 \\ r_1 & 1 \end{pmatrix}\begin{pmatrix} \mathrm{E}_{2\mathrm{f}} \\ \mathrm{E}_{2\mathrm{b}} \end{pmatrix} \tag{2.13}$$

where; $r_1 = (n_1 - n_2)/(n_1 + n_2)$ and $t_1 = 2n_1/(n_1 + n_2)$. Refractive index is defined as the square root of the dielectric constant; $n = \sqrt{\varepsilon - j\varepsilon'}$, where imaginary part is due to absorption in the medium. Using above equality, we have transferred fields at the left of interface to the right.

Electric field traveled in the second medium can be found using the propagation of plane wave.

$$\begin{pmatrix} \mathrm{E}_{2\mathrm{f}} \\ \mathrm{E}_{2\mathrm{b}} \end{pmatrix} = \begin{pmatrix} e^{jkx} & 0 \\ 0 & e^{-jkx} \end{pmatrix}\begin{pmatrix} \mathrm{E}_{2\mathrm{f}}(\mathrm{x}) \\ \mathrm{E}_{2\mathrm{b}}(\mathrm{x}) \end{pmatrix} \tag{2.14}$$

where $k = 2\pi n/\lambda$.

Combining these two building blocks, we can evaluate the transfer matrix of electric fields from start of a layer interface to the next layer's interface as follows:

$$\mathbf{T}_i = \frac{1}{t_i}\begin{pmatrix} e^{j\delta_i} & r_i e^{j\delta_i} \\ r_i e^{-j\delta_i} & e^{-j\delta_i} \end{pmatrix} \tag{2.15}$$

where $r_i = (n_i - n_{i+1})/(n_i + n_{i+1})$, $t_i = 2n_i/(n_i + n_{i+1})$, and $\delta_i = k_i d_i$. Cascading these matrices for N layers, total transfer matrix for the multilayer system becomes:

$$\mathbf{T}_{\mathrm{total}} = \mathbf{T}_0\mathbf{T}_1\cdots\mathbf{T}_{\mathrm{N-1}}\mathbf{T}_{\mathrm{N}} \tag{2.16}$$

Electric field before and after any stack of arbitrary layer combination becomes:

$$\begin{pmatrix} E_{\mathrm{bf}} \\ E_{\mathrm{bb}} \end{pmatrix} = \mathbf{T}_{\mathrm{total}} \times \begin{pmatrix} E_{\mathrm{af}} \\ E_{\mathrm{ab}} \end{pmatrix} \tag{2.17}$$

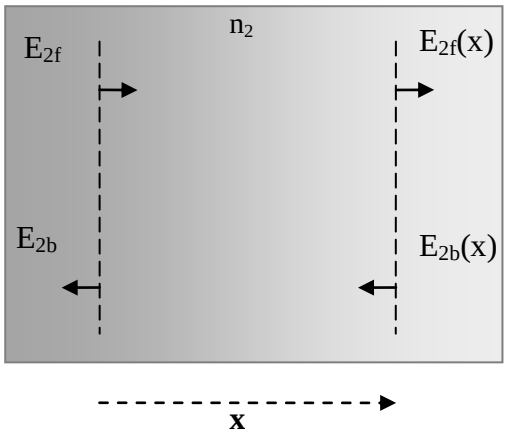

Figure 2.11: Second building block of optical multilayer films: Electric field is transferred, or propagated, inside a homogeneous medium.

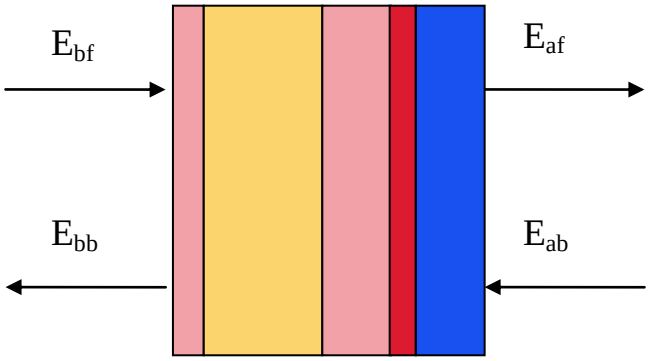

Figure 2.12: A general multilayer film, with electric fields before and after the stack.

We need to find reflected power, since measurement devices detect power not electric field. Power can be found using:

$$\vec{S} = \vec{E} \times \vec{H}^{*} \tag{2.18}$$

For a plane wave

$$\vec{H} = \frac{1}{\omega\mu} \vec{k} \times \vec{E} \tag{2.19}$$

From these equations, it is apparent that power is proportional to the square of electric field and the refractive index of the medium. Reflectivity and transmittivity can be found using:

$$R = \frac{\left|E_{\text{bb}}\right|^2}{\left|E_{\text{bf}}\right|^2} \tag{2.20}$$

$$T = \frac{\left|E_{\text{af}}\right|^2 n_{\text{final}}}{\left|E_{\text{bf}}\right|^2 n_{\text{incident}}} \tag{2.21}$$

Absorption in any medium, which we use when simulating quantum efficiency, can be found using power going inside the medium and power getting out of the medium.

2.3 Light Emitting Diodes

After thousands of years of incandescence (heat glow) for lighting, about 100 years ago first solid state material with light emission using electrical power source has been reported [24]. In 1891 E. G. Acheson established a process for new man-made material silicon carbide (SiC, then called *carborandum*) using glass (a-SiO_2) and carbon (C) in an electrical high-temperature heater environment. Since this material was very hard (hardness index diamond:10.0, carborandum:9.0 and pure SiC:9.2-9.5) it was long used to prevent corrosions in industry. Later in 1907, H. J. Round checked and showed that such crystals can be used as electrical rectifiers. He also noticed that crystal was also emitting yellow light with applied potentials of 10 V for some specimens and up to 110 V for others. These first light-emitting-diodes (LEDs) were made of crystal-Schottky metal contact junctions and it was later

understood that light was generated through charge recombinaton from metal to semiconductor under forward bias (10 V case) and avalanche effect under reverse bias (up to 110 V case).

Although SiC was first ever LED material, it was not a competitor for soon-coming III-V semiconductors. It was an indirect bandgap semiconductor, and this property prevented it from improving over the decades.

In 1950s, III-V compound semiconductor research started. It was seen that these materials were very suitable for optical applications. In 1954, first bulk growth of GaAs from melt has been achieved, first infrared LEDs and laser diodes (LDs) reported and a huge research effort was invested on AlGaAs/GaAs devices.

The wavelength of light usually dictates the semiconductor material to be used via the bandgap energy. It is also equally important that these materials allow to be doped n- and p-type. For band aligning, and for charge trapping and other phenomena, the electron affinity (energy for an electron in bottom of conduction band to reach vacuum level), work function (from Fermi level to vacuum level), and band offsets (in the case of heterojunctions) should be known for an effective device design.

Then highly frequent use of AlGaAs and GaAsP based green and red LED usage started. LEDs at those times have been used as indicators in telephone sets, displays, calculators and wristwatches.

Discovery of GaN based LEDs is rather interesting. In the late 1960s, at Radio Corporation of America's (RCA) central research laboratory in Princeton, J. Tietjen wanted to build a flat panel television, which can be mounted on a wall, similar to today's TV sets. For true color display, red and green LEDs were already available on the market. He needed a blue LED as bright as others, and GaN was to be grown as a single crystal. He delivered the challenge to P. Maruska in his research group, who was very experienced on GaAsP red LED growth using metal-halide vapor phase epitaxy (VPE) method. In 1969, Maruska, finally achieved the job; first ever

single crystal film GaN was grown after many failures [25]. Three years later, electroluminescence at 475 nm was reported from GaN with surface probe contacts. As-grown GaN films were always n-doped, with some work researchers achieved to make it semi insulating but failed to find an effective p-doping material. As a result, devices were inefficient. Ironically, "Tietjen, who had stimulated the work, now terminated it by ordering "stop this garbage" – words that Maruska still vividly remembers" [24].

After RCA team cut the efforts, research on GaN was almost ended. For example, in 1982 only one single paper was appeared in literature. However, I. Asaki and his group from Japan did not give up, and in 1989 they managed to make first p-type doping in GaN using magnesium (Mg) activated by electron-beam irradiation [26] and later, others, by post-growth anneal [27]. These works paved the road to today's all nitride-based LEDs and LDs.

In this part, basic physics that is relevant to our work will be given, followed by a brief explanation of LED structures incorporating luminescent coatings. Then, the calculation of CIE color space parameters related to apparent color and finally our LED structures will be presented.

2.3.1 Basics

Light emitting diode is simply a forward biased p-n junction. Carriers are injected into the structures through n- and p-sides, and majority carriers are recombined in the junction.

At any time, light can be emitted from a semiconductor material as a result of electron-hole recombination [28]. However, emitted light is so dim that, practically these materials do not glow at room temperature. For example, for a slab of GaAs at room temperature (radiative recombination rate $r_r = 10^{-10}$ cm^3/s, intrinsic carrier concentration $n_i=1.8x10^6$ cm^{-3}), electroluminescence rate is 374 photons/cm^3-s. Whereas for GaN ($r_r = 10^{-10}$ cm^3/s, $n_i=1.8x10^6$ cm^{-3}), this number is approximately 361 x 10^{-30} photons/cm^3-s, or practically zero. This is why GaN is superior in this

aspect; there are no electrons wandering in the crystal. For this reason, if a discernible light (not counting the blackbody radiation) is to be extracted from the material, extra carriers have to be injected into the semiconductor in some way, for example via forward biasing the diode and injecting carriers through external circuit.

When the p-n junction is forward biased, the current flowing across the junction has two components: holes are injected from p-side to n-side and electrons are injected from n-side to the p-side (or, to be exact on the process, high energy electrons in conduction band are injected from n-side and low energy electrons in valence band are collected from p-side). At the beginning, this minority carrier injection disturbs the equilibrium condition. Extra carriers, which otherwise should not be there recombines with the majority carriers around until equilibrium (thermal equilibrium under steady state) is reached. As long as the current continues to flow, minority carrier injection continues [29] and steady state carrier distribution is achieved, so that the recombination rate is equal to the injection rate.

Minority carrier recombination is not instantaneous; rather, the carriers have to find proper conditions for recombination. Both energy and momentum must be conserved. Energy conservation is easily satisfied because to-be-radiated photon takes the energy of electron-hole pair, but the photon does not contribute to momentum issues very much. Therefore, an electron can recombine with a hole of almost identical and opposite momentum, and this condition is not easily met, resulting a delay. In other words, minority carriers have a finite lifetime (τ_n and τ_p), and also they have finite diffusion lengths (L_n and L_p).

The average time to recombine radiatively through the emission of light can be visualized as the average time it takes an injected minority carrier to find a majority carrier with the right momentum to allow radiative recombination without violating momentum conservation [29].

In Figure 2.13(a,b), a typical p-n junction under zero and forward bias is shown. As it is seen, the recombination takes place throughout a wide region of the structure, which means more distance carriers takes resulting an increase in heat

generated. Making the device shorter means, carriers come in and goes out from the device, and wasted. To decrease device length effectively, heterostructures are proposed (Figure 2.13(c)), in which, carriers are confined in a small bandgap material sandwiched between two high bandgap materials. This way, long $L_{n,p}$ distance is reduced to W_D, which can be fine tuned with appropriate designs.

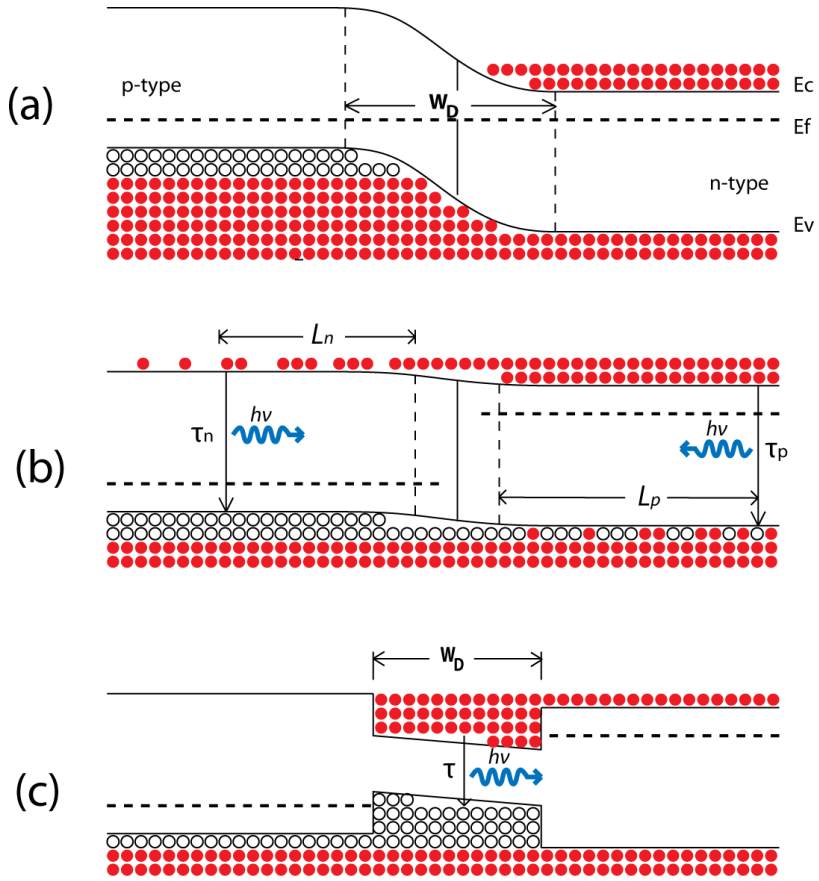

Figure 2.13: p-n homojunction under zero (a), forward bias (b). p-n heterojunction in forward bias. In homojunctions, carriers diffuse, on average, over the diffusion lengths L_n and L_p berfore recombination. In heterojunctions, carriers are confined by the heterojunction barriers (after [24]).

Radiative recombination rate $\tau_{n,p}$ can be increased if wavefunctions of electrons and holes could in a way coincides with each other. This is possible, if confined carriers in a heterojunction could be confined further, by quantum wells. This is depicted in Figure 2.14. For a normal p-n junction, carriers are distributed over a distance, but in a quantum well, they are all confined in a single well, and ready to recombine with holes in valence band, whose wavefunctions overlap with corresponding electrons easier compared to the first case.

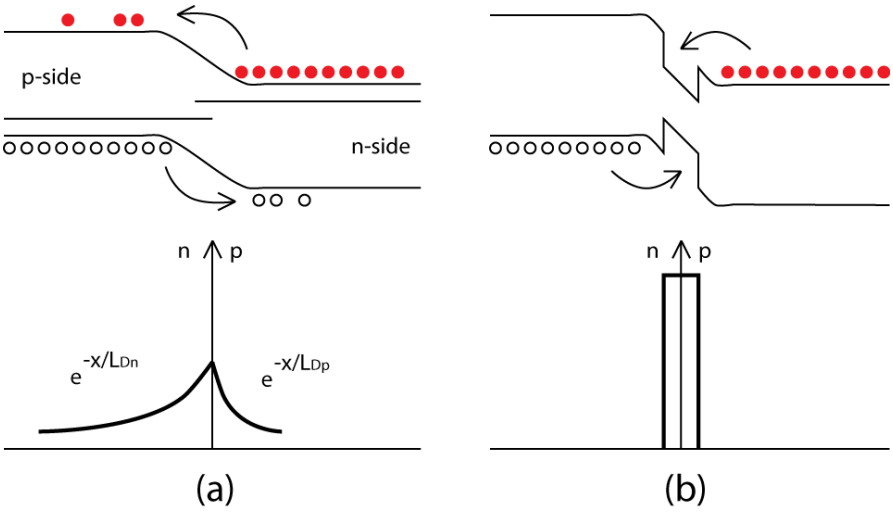

Figure 2.14: For a given carrier flux, the density of electron hole pairs is far greater in a heterojunction (b) than a homojunction (a) where these carriers can diffuse more readily (after [30]).

For electrons and holes, radiative recombination is not the only recombination path . There are also crystalline defects, impurities, dislocations and surface states, all of which can trap the injected minority carriers. This type of recombination process may or may not generate light. Energy and momentum conservation are met through the successive emission of phonons. Again, the recombination process is not instantaneous because the minority carrier first has to diffuse to a recombination site.

This nonradiative recombination processes are characterized by their specific lifetimes.

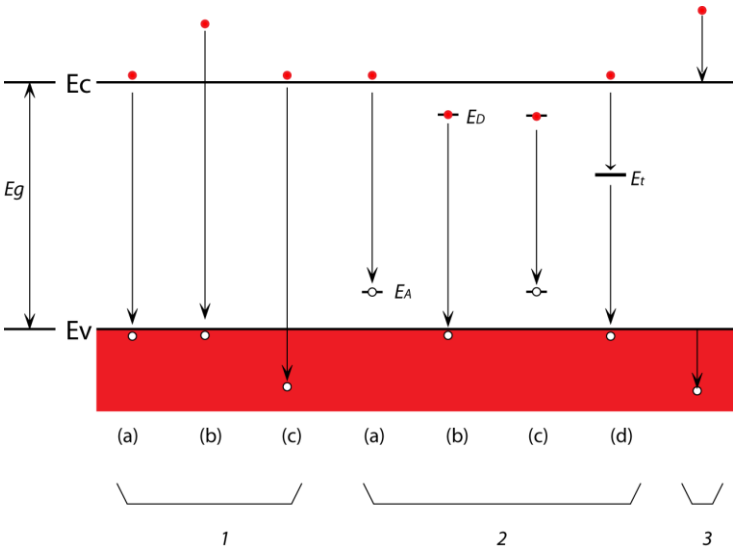

Figure 2.15: Basic recombination mechanisms in semiconductors, E_D, E_A, and E_t are donor-type, acceptor-type, and deep level traps respectively (after [31]).

In Figure 2.15, basic recombination mechanisms of excess carriers are depicted. The classification is as follows [31]:

1) Interband transition:
    a. Intrinsic emission corresponding very closely in energy to the bandgap
    b. Higher energy emission involving energetic or hot carriers, sometimes related avalanche multiplication
2) Transitions involving chemical impurities or physical defects:
    a. Conduction band to acceptor-type defect
    b. Donor type defect to valence band
    c. Donor-type to acceptor type defects (pair emission)
    d. Band-to-band via deep level traps

3) Intraband transition involving hot carriers, sometimes called deceleration or Auger process.

In this picture, not all transitions can occur in the same material or under the same conditions, and not all transitions are radiative. It was shown that band-to band recombination (1-a) is the most probable radiative process.

So far, a broad and qualitative introduction has been given. Lastly, we will introduce the basic diode structure that was used in the present thesis work.

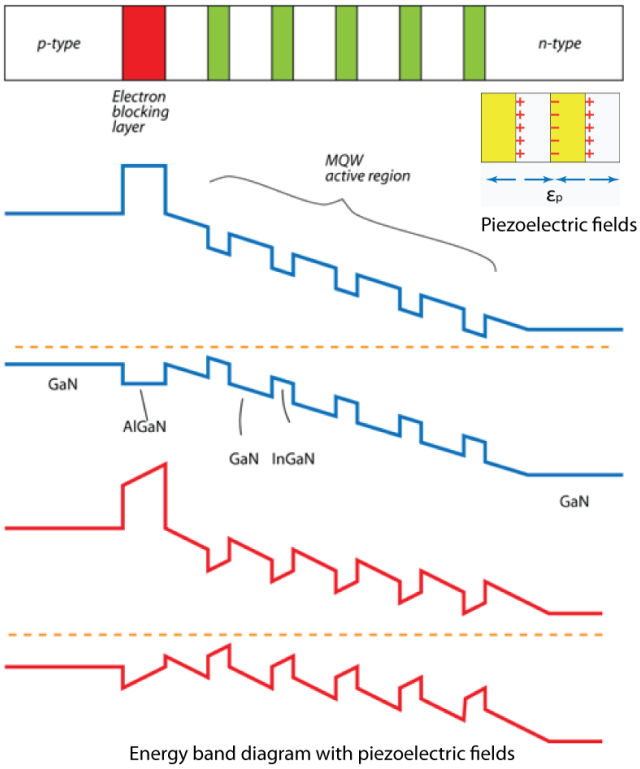

Figure 2.16: InGaN/GaN LED with MQW structure under zero bias. High bandgap electron-blocking layer further confines electrons to MQW region.

As it is seen in Figure 2.16, a little more complex (and evolved through years by researchers) heterojunction is used. In this structure, electrons are injected from the n-side (GaN) and it is desired that they recombine with other injected holes in the multi-quantum-well (MQW) region (InGaN/GaN). They are confined in this region

by several quantum wells (QWs) (5 wells in our structure). Several wells are used for operation in high power, or high charge injection conditions, in case density of states in one QW does not suffice. Charges are distributed over a distance and are recombined. Despite this length, carriers may still reach to the other side of the device (GaN) and get out of the diode to external bias circuit. To prevent that condition, one larger bandgap (AlGaN) semiconductor slab was sandwiched between MQWs and p-type contact, for electrons not to reach p-contact by hopping through QWs. This layer is also p-doped to prevent electrons jump over (rise barrier, though leaving some trap points for holes in the valence band) and also made thick enough so that electrons does not tunnel through (for example >10 nm).

2.3.2 Light Emitting Diodes with Luminescent Coatings

Today almost all of the white LEDs consist of a pumping LED and a white light flourescent coating (phosphor) on top of it, which is the simplest structure. Due to the emission band structure of these coatings, emitted light is not very pleasant to the eye; it is bluish and cool, not like day-light. The red component in the emission spectrum of coating material is insufficient for a true white light.

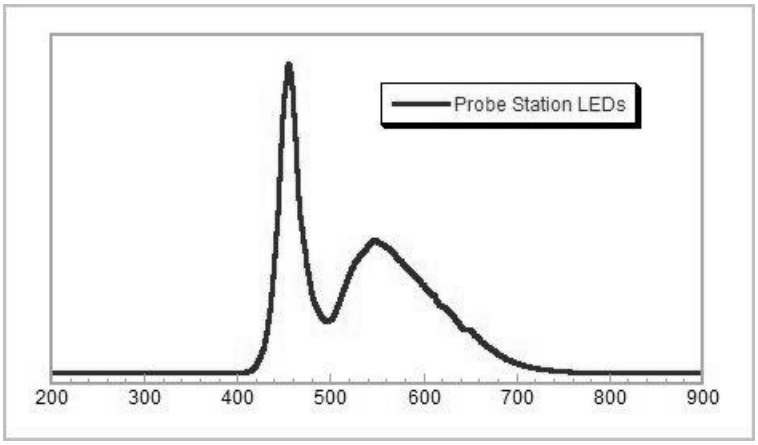

Figure 2.17: Electroluminescence of white light LEDs which were mounted on the probe station.

Figure 2.17 shows one of the simplest white light LEDs used commercially. Blue-green LED, which emits at 460 nm pumps a phosphorous coating and coating

re-emits in longer wavelengths. As it is also clear in the spectrum, red component is low, compared to a daylight spectrum. That means, if this LED is to be used in a lighting application, red or orange colored textures will be seen darker than their daylight appearances, which is visually disturbing (low color rendering). There are other parameters related to the quality of a light source, like color coordinates in a chromaticity diagram, parameters like color rendering, color temperature and color mixing. These are determined by The International Commission on Illumination (CIE for its French name, Commission internationale de l'éclairage) [32] and they need to be optimized for a high quality white light source application.

Chapter 3

Device Processing

3.1 MOCVD Growth of Wafers

Metal Organic Chemical Vapor Deposition (MOCVD) is a method for growing compound semiconductor epitaxial layers. In this method, precursors are carried into a well-controlled chamber in a carrier gas, H_2. In high temperature and low pressure conditions, atoms are deposited one by one on a substrate by well controlled manner. Precursors are carried into the chamber. Wafer is heated on wafer holder and precursors are dissociated on hot temperature zone, III-V elements are reacted and deposited on the wafer. Substrate, called as wafer in our case, is rotated by several rotations per minute for uniform deposition throughout the growth. Schematics of the system and photograph of the chamber are shown in Figure 3.1 and 3.2.

An interferometer is located above the quartz chamber, which has an opening window on top. During the epitaxial growth process, the film thickness, growth rate, surface roughness, growth temperature, gas flow rate parameters etc. are all monitored through electronic controller and in-situ measurement tools. So,

depending on the feedback taken from the measurements, growth can be fine-tuned in real time in extreme cases.

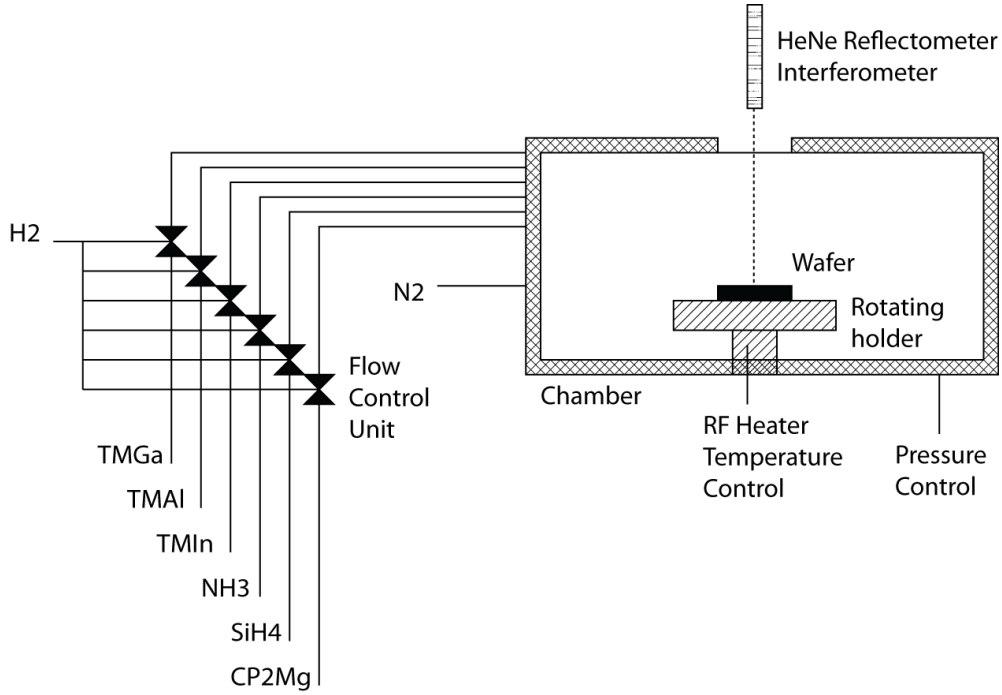

Figure 3.1: Schematic diagram of MOCVD system.

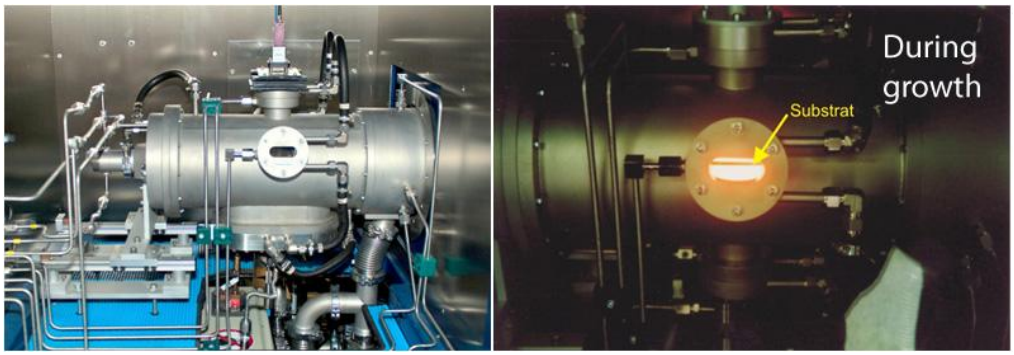

Figure 3.2: Photographs of MOCVD reactor in NANOTAM.

Since GaN has no bulk crystal, as in silicon or GaAs, they are grown on sapphire substrates, usually, which is the most suitable material in terms of lattice match and hardness compared to other options. Due to the lattice mismatch (Figure

3.3), crystal quality GaN can not be grown directly on sapphire. Stress does not allow long range order. Therefore, growth starts with nucleation and buffer layer growths, which were two major breakthroughs in growth development of thick III-Nitride crystals. Instead, at the beginning, crystal islands are grown in a 3D manner, as in Figure 3.4, which is called nucleation. This process is observed in interferometric graph as a reflection minimum. Nucleation temperature is generally much lower, e.g. ~500-600 °C, than actual above-1000 °C growth temperatures. After islands grow large enough and they start to merge, 2D and 1D growth begins, as in Figure 3.5. After this, a buffer region is grown to relax stresses and lower dislocation density. After the buffer, normal GaN or AlGaN crystal growth can be done as long as needed. Depending on growth parameters, the crystal defects and dislocations can propagate up to the wafer surface, as shown in Figure 3.6. These defects might not be seen with naked eye or hardly with optical microscope just after the growth. However, they can be quite visible after an etch process which has anisotropy and selectivity for certain crystal directions and crystal defects. In Figure 3.6, a sample surface is shown and as it is clear on metal coated areas, these defects are present before and after any etch steps.

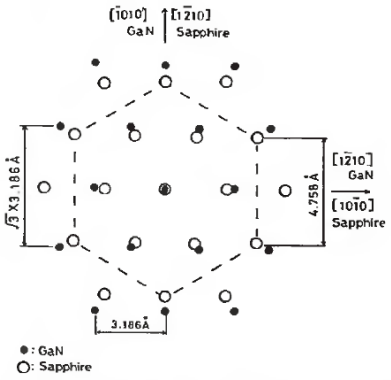

Figure 3.3: Lattice mismatch between sapphire and GaN crystals looking in c-direction (after [33]).

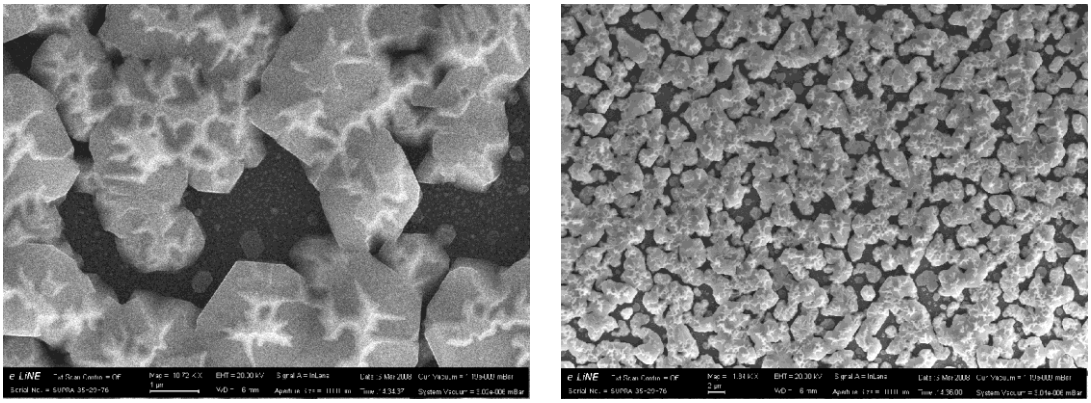

Figure 3.4: Initial 3D growth of GaN on sapphire substrates.

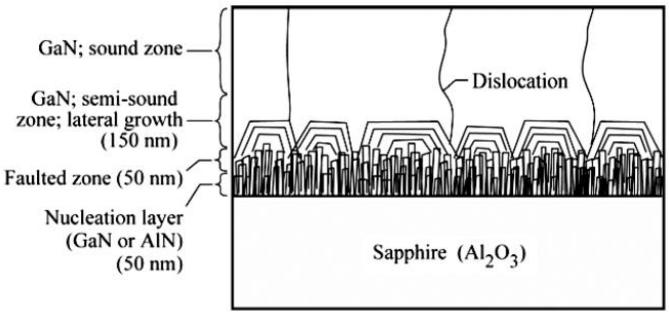

Figure 3.5: Nucleation, buffer and dislocation structure of GaN growth (after [33]).

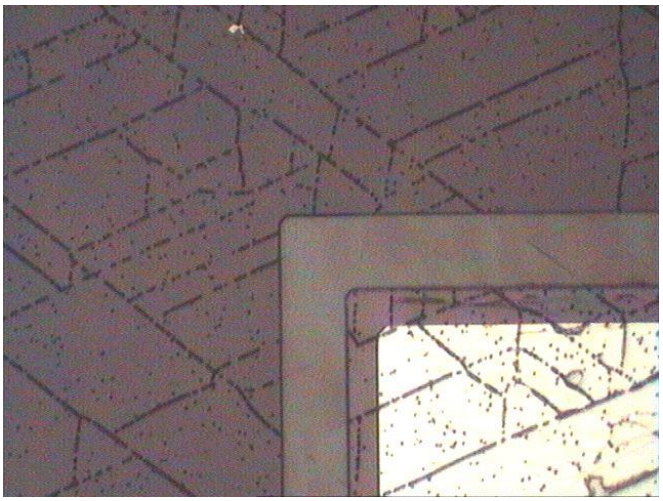

Figure 3.6: Crystal defects propagated up to the surface of crystal during the growth.

After growth is completed, the crystals are investigated using photoluminescence (PL), transmission, Hall effect measurement, Nomarsky microscope and Atomic Force Microscope (AFM) for surface roughness, and X-Ray Diffraction (XRD) for crystal structure characterization. PL and transmission gives the bandgap of grown materials and quantum wells. XRD gives crystal quality, type and crystal structure.

3.1.1 Detector Structure Growth

The GaN p-i-n structure used in this work was grown on double-side polished c-plane sapphire (Al_2O_3) substrates by low-pressure MOCVD system, in NANOTAM. First, the wafer surface was cleaned by desorption in an H_2 environment at 1080 ºC. Then, ~1000 Å AlN nucleation layer was grown at 500 ºC by trimethylaluminum (TMAl) and ammonia (NH_3). The wafer surface was recrystallized by annealing at 970 ºC. After recrystallization, a high temperature GaN buffer layer of 2500 Å was grown with trimethylgallium (TMGa) and high flow NH_3 at 1160 ºC. An n-layer with a thickness of 5000 Å was grown with silane (SiH_4), resulting the free carrier concentration of 10^{18} cm^{-3}. The growth continued with a 5000 Å thick i-layer. In the last step, an 800 Å p-layer with Mg doping by biscyclopentadienylmagnesium (Cp_2Mg) was grown [34,35]. In all of the steps, the carrier gas was H_2 and the chamber pressure was kept at 200 mBar.

In Figure 3.7 and 3.8, the photodiode epitaxial structure and PL measurements are shown. A ~5-6 nm full width at half maximum (FWHM) of PL spectrum peak indicates a good GaN growth, of course together with absolute intensity. In addition, at 550 nm with a broad spectrum, yellow luminescence is often seen, which is the result of N-related defects, i.e. vacancies and interstitials. This luminescence can generally be seen under weak pumping conditions, in which all trap states are not completely filled.

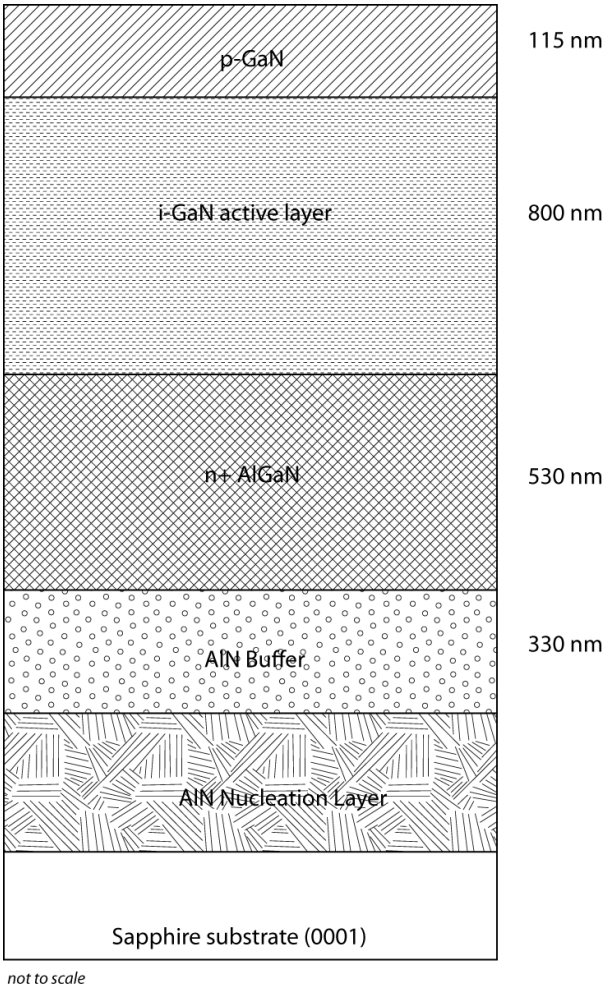

Figure 3.7: GaN p-i-n photodiode epitaxial structure.

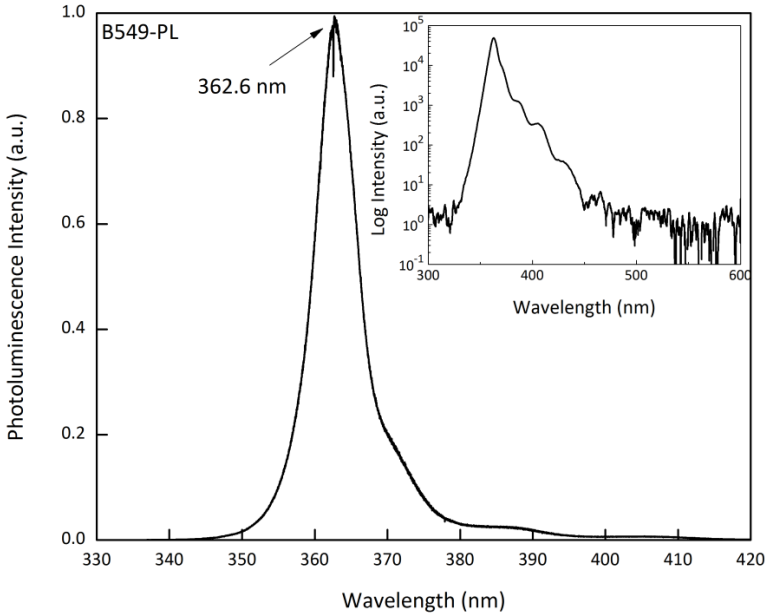

Figure 3.8: Photoluminescence measurement after growth. No yellow luminescence was observed because measurement was taken by microscope objective. Under high photo injection conditions, yellow luminescence centers are saturated and are suppressed in the output.

3.1.2 LED Structure Growth

Light emitting diode (LED) structures were again grown on a c-plane (0001) sapphire surface by same AIXTRON RF200/4 MOCVD system. The wafer structure consists of a top layer p+ GaN, AlGaN blocking layer (in later growths), 5 pairs of InGaN/GaN quantum well-barrier (QW) pairs, which are stacked between the n+ GaN layer and the AlGaN barrier layer. The large bandgap AlGaN blocking layer is for confining charges close to the InGaN/GaN pairs so that more charges are recombined to generate photons, in which it considerably enhances LED output.

From the previous growth runs, we optimized the emission wavelength of LEDs, which depends on the well thickness, barrier thickness, and growth temperature.

In the following Figures 3.9 and on, several LED structures are given which are used in this work.

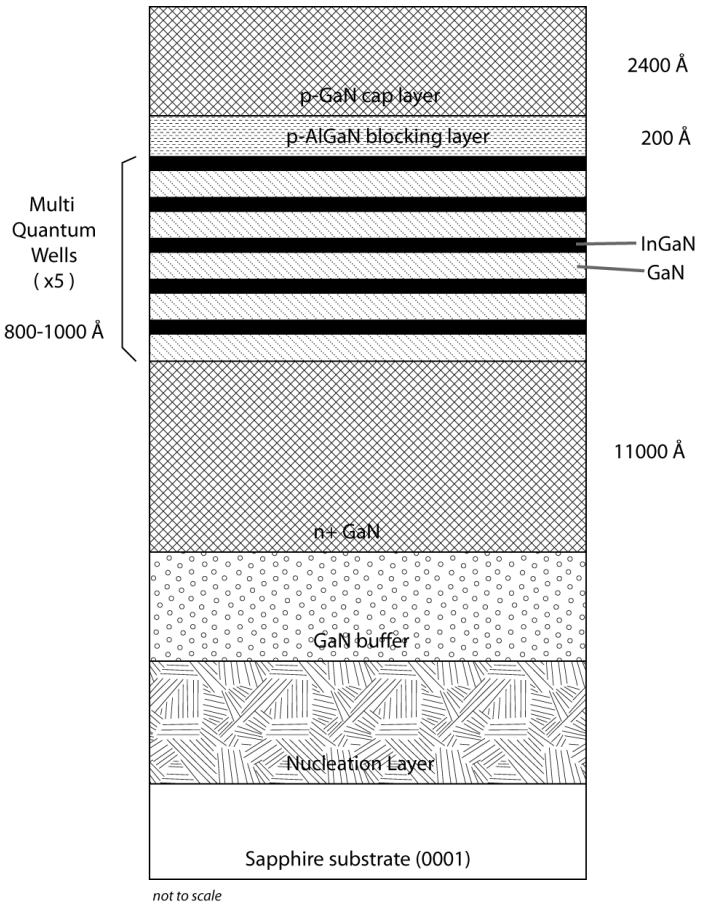

Figure 3.9: General epitaxial structure of LEDs.

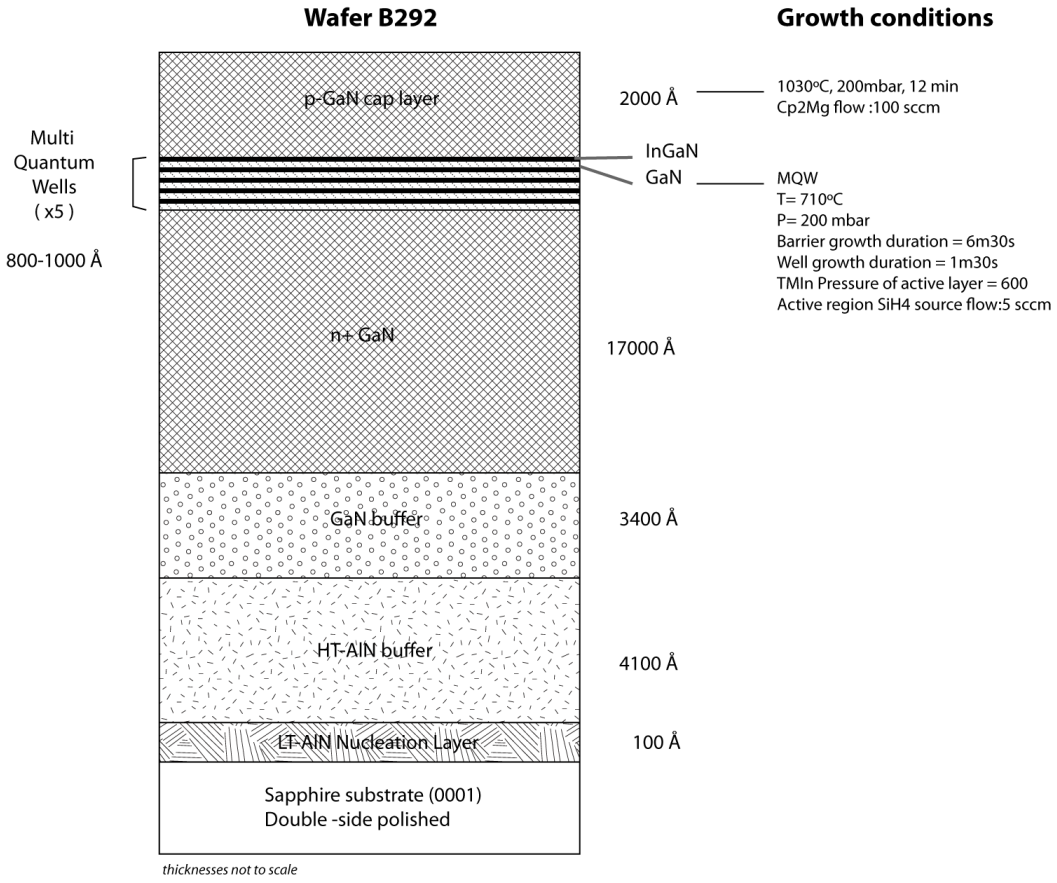

Figure 3.10: Wafer B292 epitaxial structure and growth conditions.

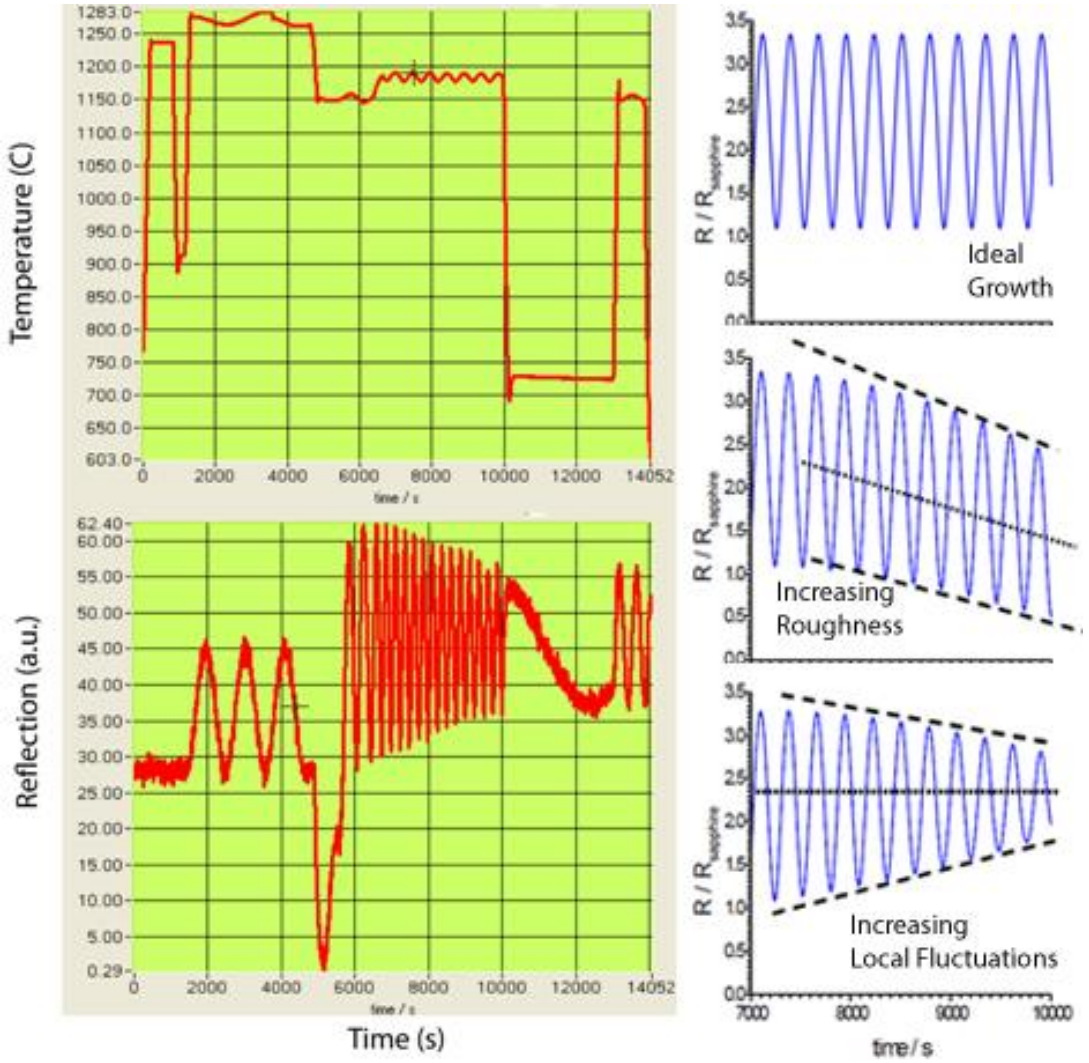

Figure 3.11: Typical temperature and reflection in-situ measurements during the growth and typical reflection behaviors.

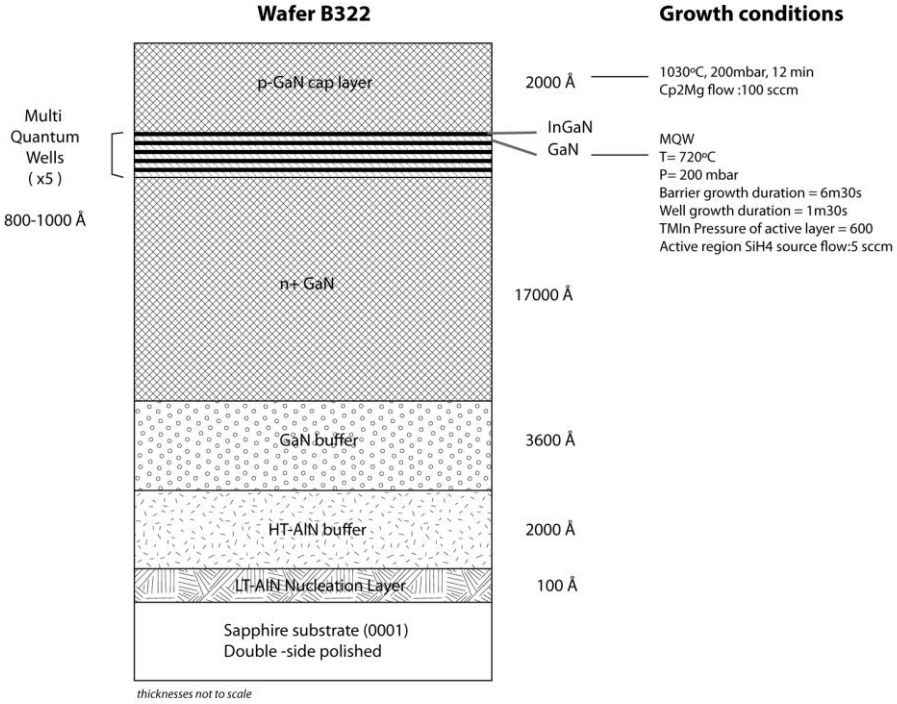

Figure 3.12: Wafer B322 epitaxial structure and growth conditions.

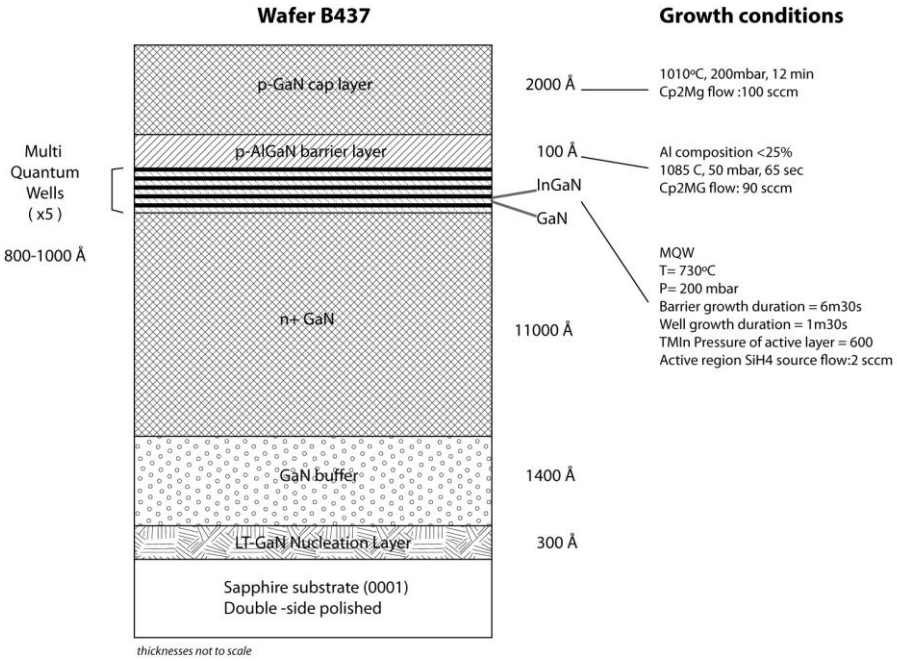

Figure 3.13: Wafer B437 epitaxial structure and growth conditions.

Three structures are investigated for LED wafer characterization given in Figures above and Table 3.1.

Wafer no	**x ($In_xGa_{1-x}N$)**
B292	14
B322	9
B437	6

Table 3.1: In compositions of three structures used in the work. The values are calculated using a transmission-matrix-method simulation code. Spontaneous piezoelectric fields are accounted in the process.

These compositions are extracted from emission wavelengths and thicknesses by using Transmission Matrix Method (TMM) code written in MATLAB. The piezoelectric fields are accounted and these parameters are taken from the literature.

The epitaxial structures of these three wafers are shown in Figures 3.10-13. In Figure 3.11, the growth parameters which are measured during the actual growth are given. During the growth, surface temperature of wafer (where deposition occurs) was measured by a thermal detector. Also surface reflection is measured by means of a white light source (halogen lamp). That way, as the growth time progress, at each moment, reflection of wafer is taken between 276.1 nm and 779.7 nm at 30 different wavelengths. Using this data, it is possible to estimate layer thickness, composition, refractive index and absorption coefficient. Also amplitude of fluctuations gives the qualitative information about how the surface was grown, which is given in Figure 3.11. As shown in Figure 3.4 and 3.5 nucleation and 3D-2D-1D growth transitions can be observed in this reflection figure, although these are not always that apparent. For example, the dip in the reflection graph represents the submicron or micron size 3D islands and also transition from AlN buffer to the GaN buffer. At this point reflection drops for GaN islands are formed on AlN buffer.

The most important issue in LED material growth is the non-radiative dislocations, as shown in Figure 3.14. These centers trap electrons and holes, and act as deep and shallow level trap centers for carriers. This is the main reason which increases the non-radiative transition probability in the device operation.

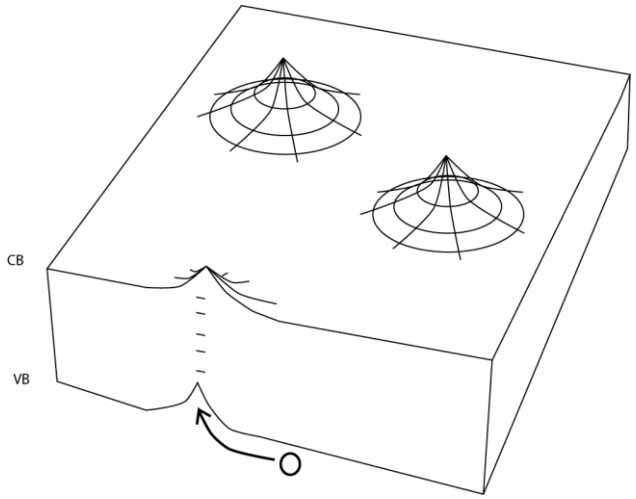

Figure 3.14: Band diagram of semiconductor having negatively charged dislocations. Holes are attracted to these dislocations where they must ultimately recombine with electrons (after [24])

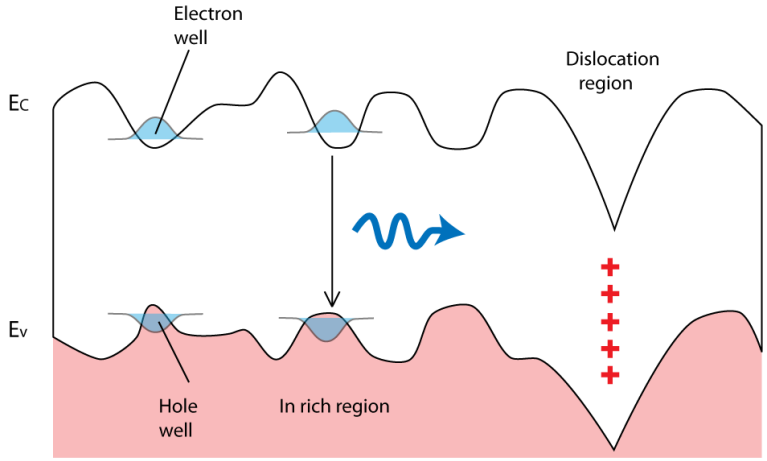

Figure 3.15: Band diagram of InGaN having clusters of In rich regions which spatially localize carriers and prevent them from diffusing to locations (after [24]).

Also this kind of centers in photodiode epitaxies result in trapped charges which reduces the speed of device (frequency response worsens). Similarly, in LEDs, they decrease modulation bandwidth, and decrease radiative recombination rate. The indium (In) growth for QW structures suffers from clustering effect as shown in Figure 3.15. These In rich regions are easily seen and their energy levels are calculated using the low temperature PL measurements. They occur due to imperfections in temperature distribution for very short time interval during the QW growth.

Temperature dependent PL measurements were carried out with the samples placed in a close-cycle cryostat in the temperature range of 10–300 K. The excitation source was a 200 mW, 325 nm He-Cd laser. The luminescence was collected by lenses, fed to a monochromator and detected by a Peltier-cooled CCD. The electroluminescence (EL) spectra were measured using a multimode fiber probe, which is directly connected to a spectrometer controlled by a computer. The DC current was supplied by a standard current source.

The active layers of the diodes consist of 5 periods of InGaN/GaN MQWs with a 5 and 15 nm quantum well and barrier thicknesses typically. As mentioned in growth section, the In compositions of the wells were calculated as 0.14, 0.09, and 0.06 for samples B292 (sample 1), B322 (sample 2), and B437 (sample 3), respectively. With these samples, we studied the effects of In composition on the optical properties of InGaN/GaN MQW LED structures by considering the different carrier localization effects.

To study the effect of the In composition of the active layers on the emission properties of these three devices, we performed temperature-dependent PL measurements. The redistribution of carriers within the localized states, due to the transfer between different localized states and the thermal escape of carriers from the higher energy states, leads to the occurrence of the ‘S-shaped’ temperature dependence of the luminescence peaks. Figure 3.16 shows the evolution of PL spectra for the MQW structures over a temperature range of 10 K to 300 K.

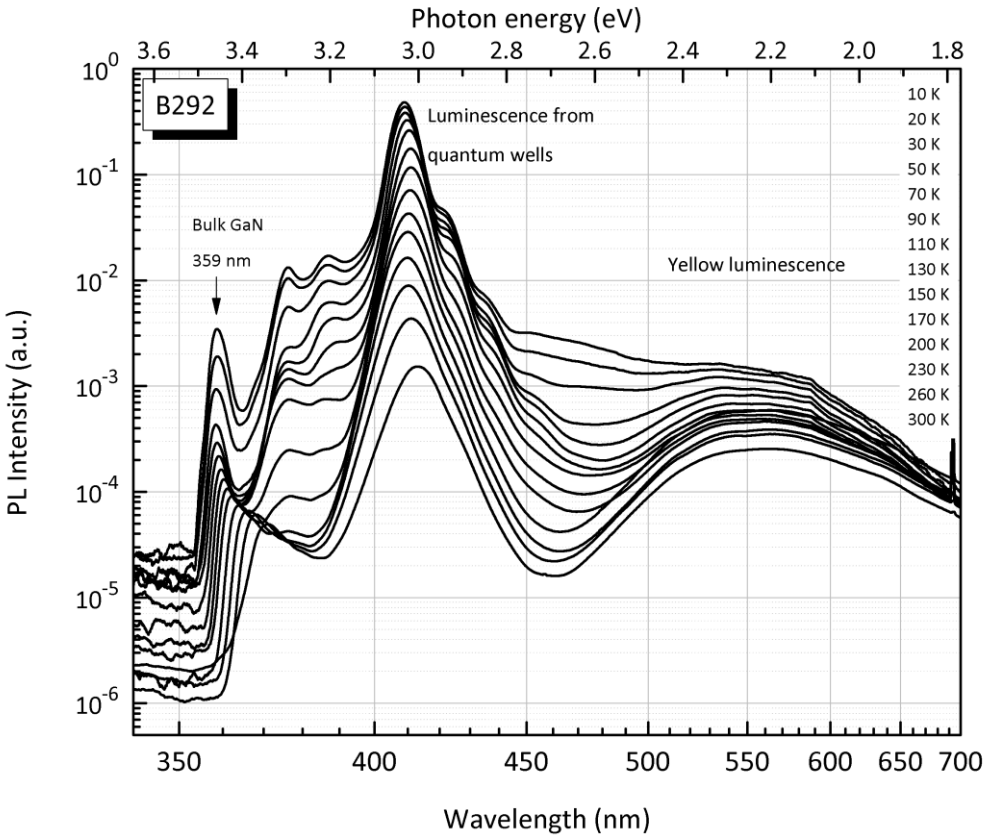

Figure 3.16: B292 PL intensity vs. temperature, notice S shape in LED emission peak.

The laser excitation density was maintained at approx. 0.7 W/cm^2 to prevent the effects of high excitation densities. At 10 K, the PL spectra peak at 2.751 eV, 3.031 eV, and 3.186 eV for samples 1, 2, and 3, respectively, were dominated by the transitions in the InGaN/GaN MQWs. The first and higher order phonon replicas of the main peaks were also observed at the low energy sides of the spectrum. Additional peaks related to the GaN band edge within the energy range of 3.44-3.47 eV, donor-acceptor-pair (DAP) and band-to-acceptor transitions at approximately 3.2-3.3 eV and yellow luminescence at approx. 2.2 eV, together with their phonon replicas, were also observed at the low temperature PL spectra. The “S” shape

behaviour of sample 1 is shown in Figure 3.17. Similar behaviour is also seen in other samples.

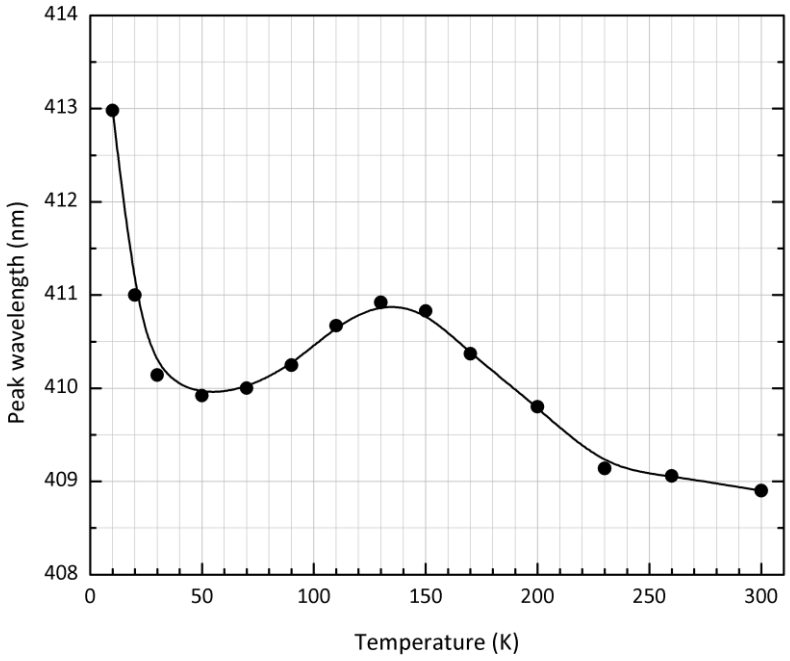

Figure 3.17: B292 Peak wavelength shift as a function of temperature (S shape).

The PL measurements with changing excitation intensity for sample 1 is shown in Figure 3.18. It is possible to extract (though qualitative) the respective density of states in radiative recombination centers.

In Figure 3.19, electroluminescence (EL) measurement of sample 1 is shown with changing injection current. Here we observe the reverse of the behaviour observed in non-polar LED structures (like AlGaAs based ones). As current increase the transitions seem to occur from lower energy centers. This is considered to be from aligning of electric fields with injected carriers (decreasing the piezoelectric field).

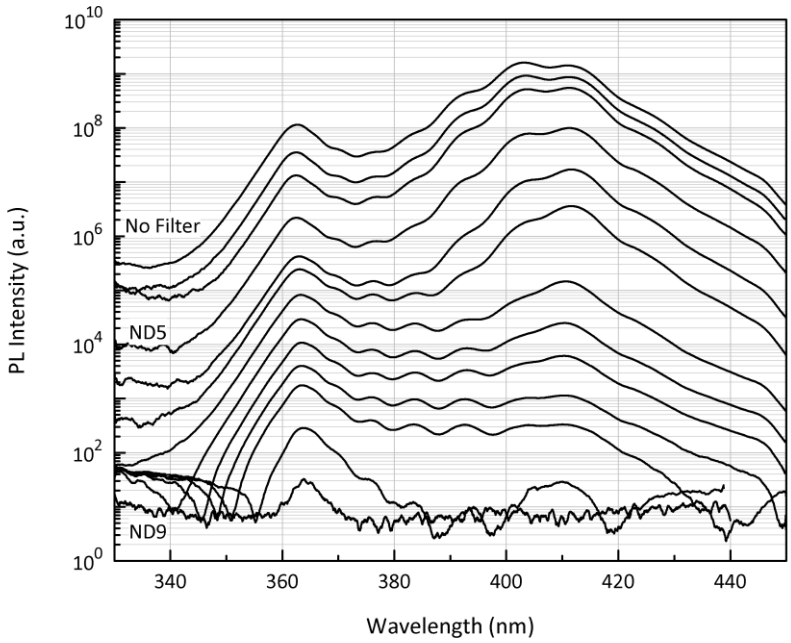

Figure 3.18: B292 InGaN LED wafer excitation intensity vs. wavelength ND filters from ND0 (no filter) to ND5+ND3+ND1=ND9.

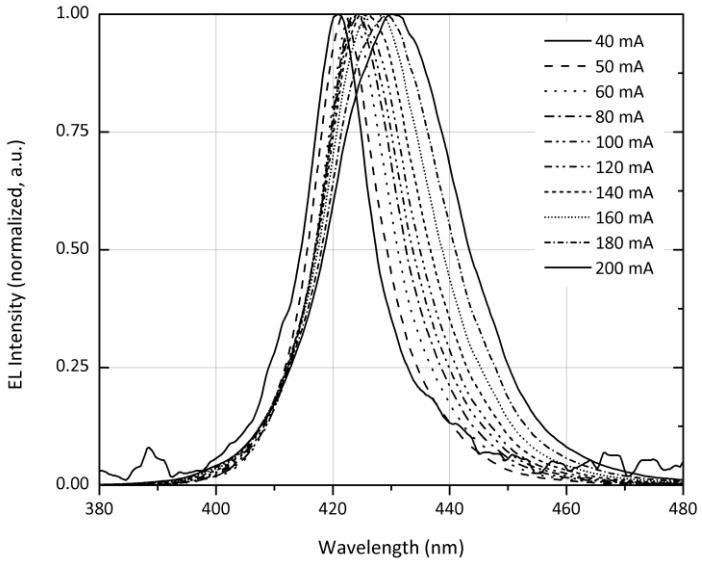

Figure 3.19: B292 wafer current vs EL intensity shift, peaks normalized.

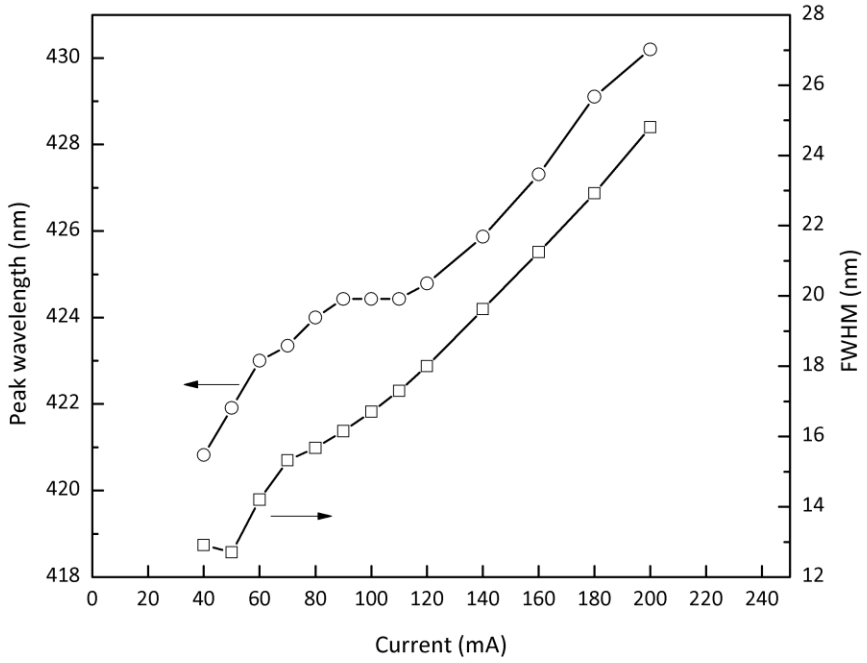

Figure 3.20: Injection current vs shift in peak wavelength of EL emission and FWHM of spectrum

The peak wavelength shift and increase in FWHM as a function of injection current in EL spectrum is shown in Figure 3.20.

In the following figures, PL measurements of other two samples, from B322 and B437 wafers, are shown. Especially in Figure 3.21, the magnesium (Mg) doping level is seen in low temperatures at about 3.2 eV with phonon replicas. This figure shows that though not necessarily electrically active, the p-type doping is very large compared to the other samples. This results in better Ohmic contact performance of the LEDs.

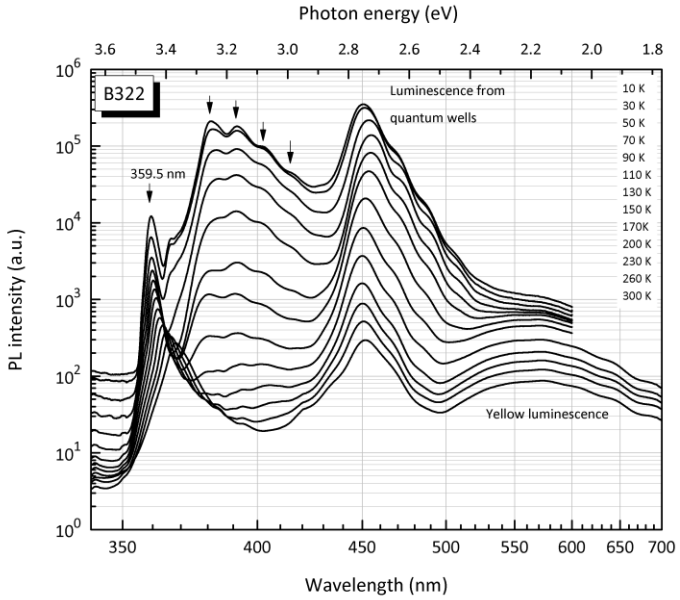

Figure 3.21: B322 Photoluminescence spectrum as a function of temperature from 10 K to 300 K. Notice S shape in QW peaks, and also transitions due to impurities (donor-acceptor) and LO phonons (arrows).

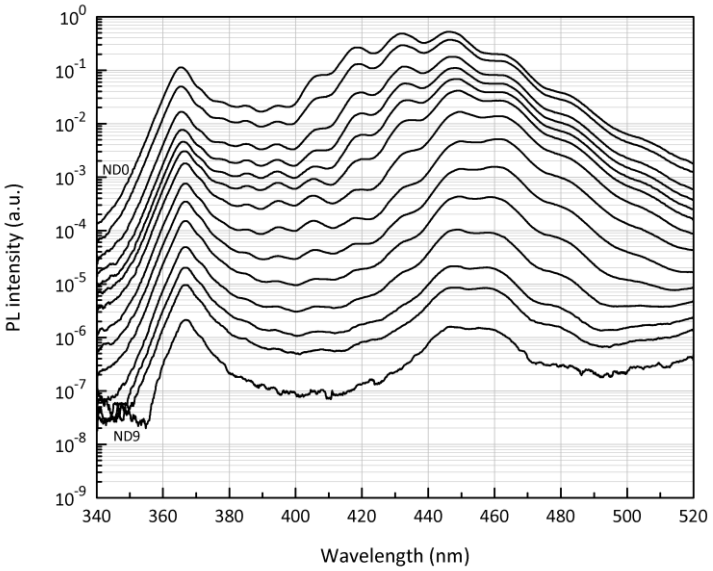

Figure 3.22: B322 Excitation Intensity vs PL spectrum. ND filters change from ND0 (no filter) to ND9.

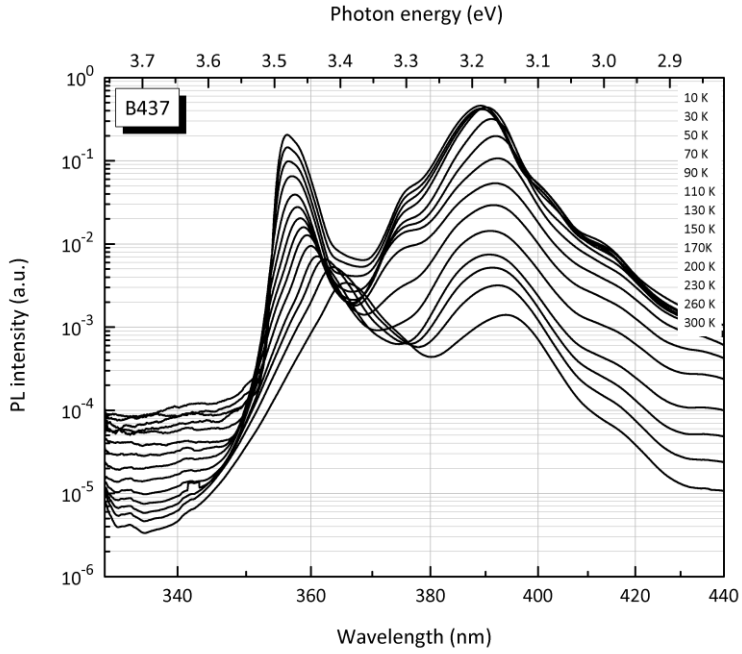

Figure 3.23: B437 Temperature vs. PL intensity.

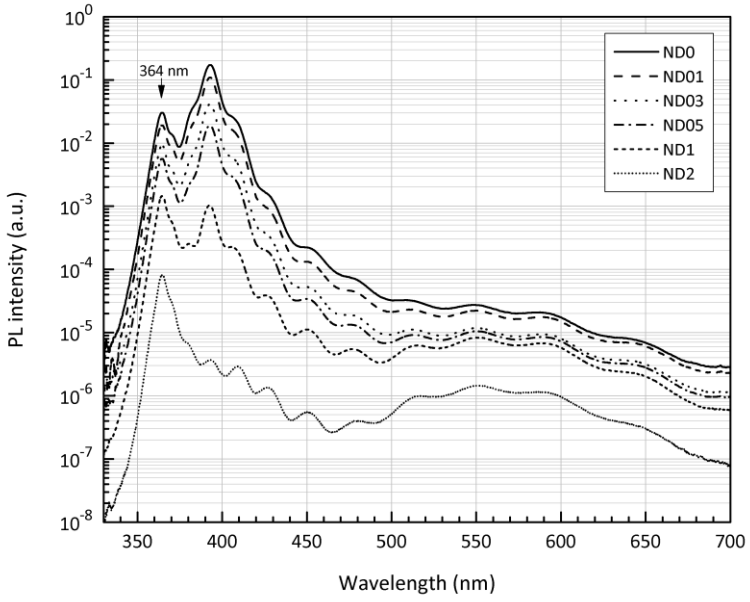

Figure 3.24: B437 PL spectrum as function of excitation intensity – wide spectrum, including (barely seen) yellow luminescence.

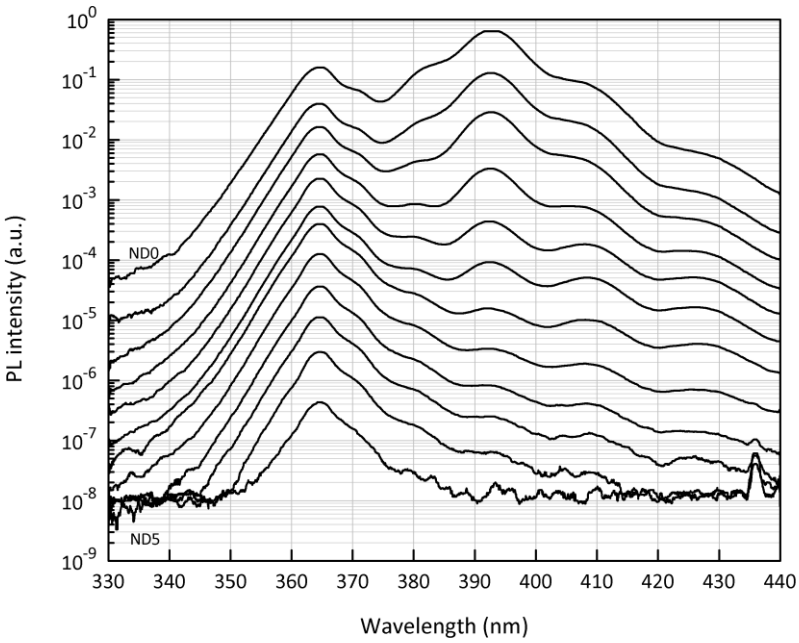

Figure 3.25: B437 PL spectrum of LED wafer as a function of excitation intensity, ND filters from 0 to ~ND5.

3.2 Clean Room Processing: Microfabrication

In this part the fabrication process, "hands-on" part of the work for photodiodes and LEDs will be presented. All process steps are completed in Nanotechnology Research Laboratory (NANOTAM) and Advanced Research Laboratory (ARL) clean rooms at Bilkent University.

3.2.1 Sample Preparation: Cleaving and cleaning

The wafers are grown on 2-inch diameter and 300 μm thick sapphire substrates. To use them more efficiently and to make more processes from one wafer for further characterizations, they are divided into ~8x8 mm^2 "samples", each containing about a hundred devices depending on the designed lithography mask layout. It is possible

to cleave wafers by hand using a diamond-tip scriber by first scribing hardly, and breaking manually, or by a dicer. In the first case, due to hardness of substrate and complex crystal structure and cleaving planes, samples are hardly rectangular, and cleaving needs care.

The III-Nitrides are very hard materials and it is very difficult to scratch wafer surfaces with mechanical cleaning approaches. It is of course better not to touch the samples with anything other than tweezers, but most of the time cleaning by a q-tip in acetone gives very clean wafer surfaces without any scratches.

After cleaning in acetone, for removing dust particles, samples are dipped into isopropyl-alcohol (ISO) for removal of acetone from surface. Then ISO is removed by rinsing into the flowing deionized (DI) water for 30 seconds. The more sample is kept in rinsing water the more it is cleaned from particles. Then, the water on the sample is removed by nitrogen gun. During these cleaning steps, extreme care is taken not to allow any liquid solvent (even water) and acid drop vaporize completely on the sample. Each solvent and water should be removed away by either another solvent or by nitrogen gun (in the last step). After that, samples are baked at 120 °C for 2 minutes on the hot-plate to evaporate very thin water layer on the hydrophilic sample surface, which happens in semiconductors with polar crystal surfaces, like silicon.

After each process steps, cleaning with acetone, ISO and rinsing in DI-water is performed for removing any residuals from previous steps. Acetone is used for cleaning photoresist after each lithography steps. If any organic based contaminant is present on the sample (for example from naked fingers or tweezers which were used elsewhere), before acetone, sample should be immersed into the boiling trichloroetane for 2 minutes.

3.2.2 Photolithography and Development

Photolithography is transferring patterns on the sample. For this process a photomask is used, having transparent and opaque regions designed and fabricated beforehand. The mask design image is given in Figure 3.26.

The opaque or transparent regions are transferred on the sample which is covered by a photoactive compound called photoresist. The choice for which pattern to be transferred is selected by two lithography flow cases: one is positive lithography, and the other is image reversal lithography. These processes are shown in Figure 3.27.

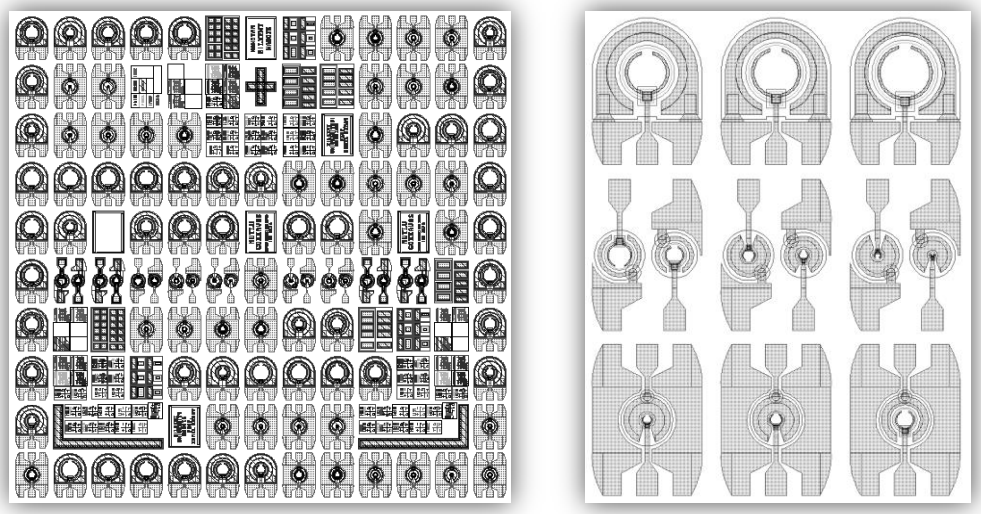

Figure 3.26: Photomask for large area photodiodes, area of 6x6mm^2 (left) and close-up view of the mask with i) large area diodes for quantum efficiency measurements, ii) test diodes and iii) smaller area diodes suitable for high speed measurements (from top to bottom on the right).

3.2.3 Etching

Etching is removal of material from selected areas on the sample. By this way, different epitaxial layers are accessed for contacts. The process is shown in Figure 3.28. Wet (acids and bases) or dry etching techniques (reactive ion etching or

sputtering) methods can be used. For III-Nitrides, dry etching is used in our processes.

3.2.4 Metal Film Deposition and Lift-off

For Ohmic or Schottky metallization, which are two most common metal-semiconductor interface situations are put onto the sample either by metal lift-off or etching of metal after blanket deposition to whole surface. The process is given in Figure 3.28. Typical coating materials are titanium/gold (Ti/Au), nickel/gold (Ni/Au) and titanium/aluminum (Ti/Al) for nitride compounds. Ti is used for material adhesion to the surface and for diffusion barrier for metals and semiconductors.

3.2.5 Thermal Annealing

Rapid thermal annealing (RTA) is required to make metal coating as low resistive as possible. This is possible by having an alloy on the surface and diffusion into the surface, just to lower the metal-semiconductor barrier, which is a result of different work functions of two materials. Although it depends on materials, the alloy temperature is 500-600 °C for GaN, n-type-AlGaN and ~800 °C for AlGaN. These temperatures depend highly on doping concentrations.

3.2.6 Dielectric Film Deposition

Dielectric films are used for passivation of surfaces and isolation of devices and contacts. Typically SiO_2, Si_3N_4, silicon oxy-nitride (SiO_xN_y) and TiO_2 films are deposited using plasma enhanced chemical vapor deposition (PECVD) and sputter coating equipments. After the dielectric lithography, they are etched by inductively coupled plasma reactive ion etching (ICP-RIE) using CHF_3 gas or wet etch. Typical etch rates are ~100 nm/min with flow rates 60 standard cubic centimeter per minute (sccm), ICP power 200 W, and RF power 100 W. Resist is removed by acetone or oxygen plasma. In extreme burned resist cases, it is removed by AZ100 remover mixed 1:1 with water and left on 60 °C hotplate for 5 minutes. Remover also

interacts with contact metals (especially Al) therefore keeping samples long period of time deteriorates the metal coatings.

We measured refractive index in a spectrum ranging from 300 to 700 nm by an ellipsometer, so that we know exactly what the index is at 494 nm or other wavelengths of interest.

The SiO2 growth parameters are as follows:

SiH_4 flow rate: 200 sccm.
N_2O flow rate: 20 sccm.
Argon (Ar) flow rate: 100 sccm.
Temperature: 300 °C.
RF power: 50 W.
Pressure: 80 Pascal.
Time: 12:00 min, giving film thickness of 575 nm.
Refractive index: 1.467 at 494 nm, 1.46 at 633 nm.

Deposited SiO2 films are etched using ICP-RIE with parameters given below:

CHF_3 flow rate: 60 sccm
RF Power: 80 W
ICP power: 200 W

Resulting etch rates are ~100 nm/min for SiO_2.

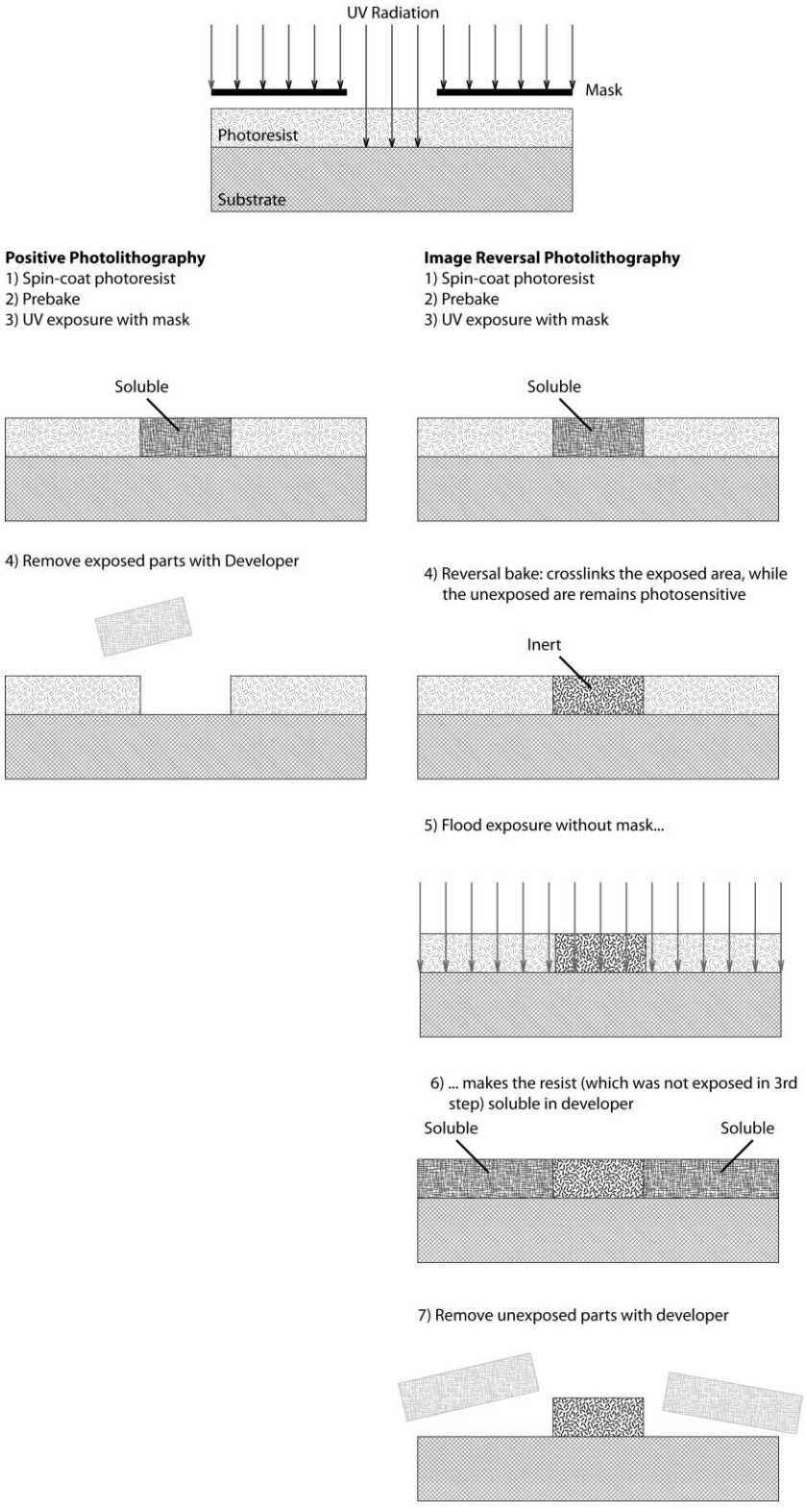

Figure 3.27: Positive and image reversal photolithography using AZ5214 photoresist.

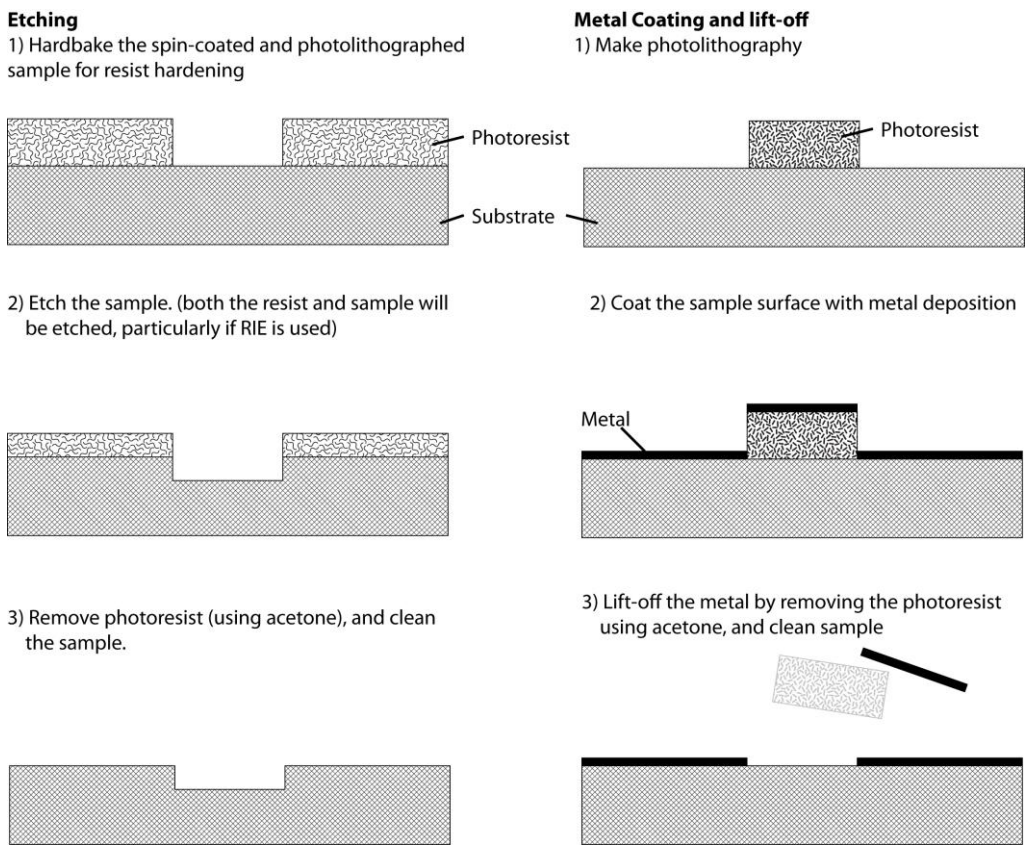

Figure 3.28: Etch and lift-off processes.

Chapter 4

Devices and Measurements

4.1 (Al)GaN Based Photodetectors

The recent developments in high quality GaN/AlGaN material growth technology have led to the realization of high performance solar/visible-blind photodetectors operating in the ultraviolet (UV) spectral region. Some applications in which GaN/AlGaN-based photodetectors are utilized include engine/flame monitoring and detection, plant/vegetation growth monitoring, UV astronomy, and gas detection [36,37,38,39,40,41]. These photodetectors are also chemically inert and suitable for harsh environments. GaN-based solid-state photodetectors with breakdown voltages ~100 V [42,43,44], responsivities of 0.18 A/W at 360 nm [45] (for Schottky type photodetectors) and 0.2 A/W at 355 nm (for back illuminated GaN based p-i-n photodetectors) corresponding to 70% quantum efficiency at zero bias [46], 3-dB bandwidth of 16 GHz (for metal-semiconductor-metal type photodetectors) [47] and 1.6 GHz (for p-i-n type photodetectors) [48] have been previously reported. In this work, we report our experimental results on high performance GaN photodetectors. Our GaN photodetectors have higher breakdown voltage, lower current density, and

higher responsivity when compared to the previously published GaN photodetector results in the literature.

4.1.1 Design and Fabrication

The samples were fabricated by a six-step microwave-compatible (having coplanar waveguide interconnect metal pads with 50 Ohm impedance) fabrication process [49,50,51] in class-100 clean room environment. The dry etching was accomplished by reactive ion etching (RIE) under CCl_2F_2 plasma, 20 standard cubic centimeter per minute (sccm) gas flow rate, and 200 W RF power conditions. Mesa structures of the devices were realized using an RIE process, by etching all of the layers (> 1.2 μm) down to the nucleation layer for mesa isolation. After an Ohmic etch of ~ 0.74 μm, Ti/Al (100 Å/1000 Å) contacts and Ni/Au (100 Å/1000 Å) contacts were deposited by thermal evaporation and left in acetone for the lift-off process. The Ohmic contacts were annealed at 750 °C for 45 s. Then, a 300 nm thick Si_3N_4 was deposited via plasma enhanced chemical vapor deposition (PECVD) for passivation. Finally, a ~0.4 μm thick Ti/Au interconnect metal was deposited and lifted-off in order to connect the n-type and p-type Ohmic contact layers to the coplanar waveguide transmission line pads. The finished device structure is shown in Figure 4.1 schematically and in Figure 4.2 as optical microscope images.

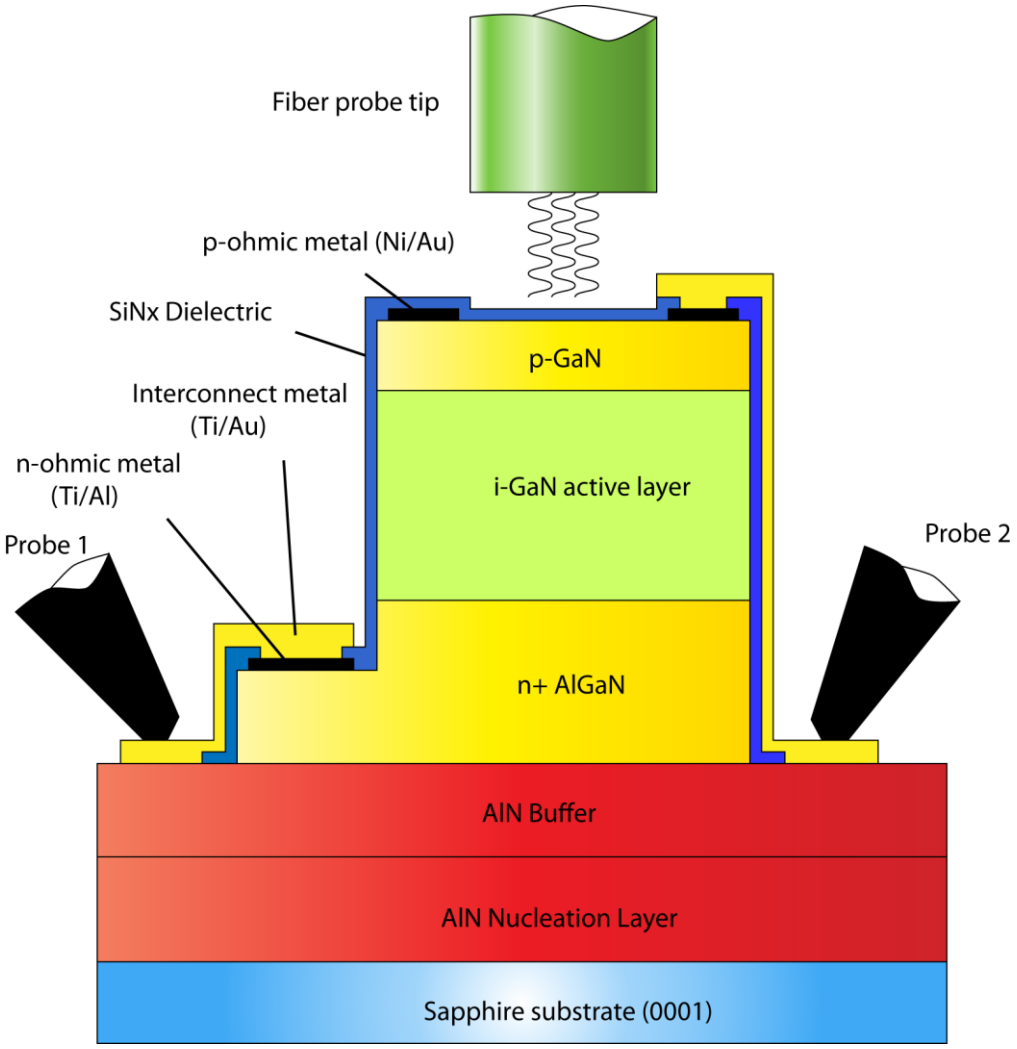

Figure 4.1: Photodetector lateral view after fabrication is finished. Probes and fiber tip during quantum efficiency measurement.

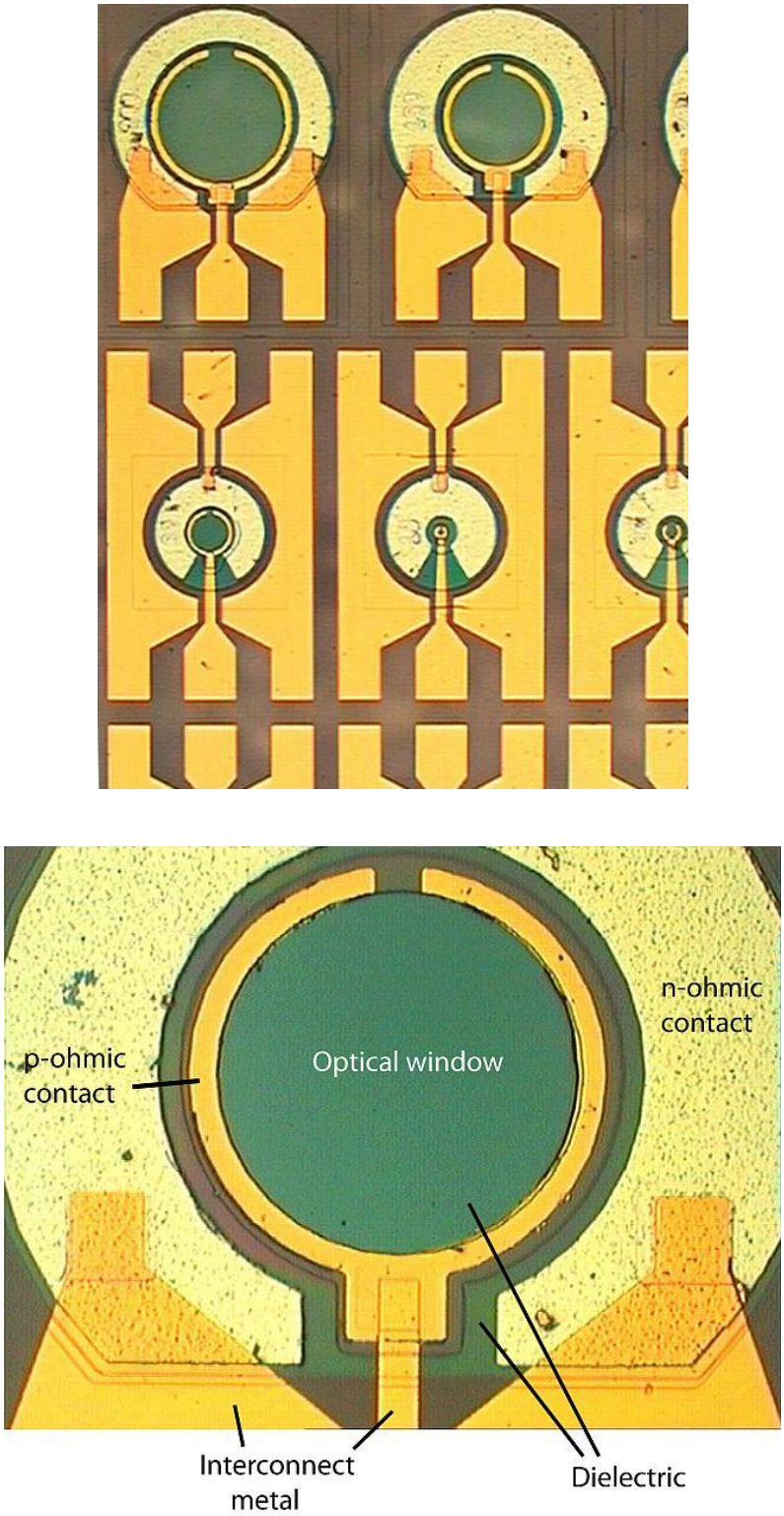

Figure 4.2: Optical photographs of completed devices.

4.1.2 Measurements and Results

For characterization, current-voltage (IV), quantum efficiency (QE), capacitance-voltage (CV) and high speed measurements were performed. IV characterization of the fabricated photodetectors was carried out by using a Keithley 6517A high resistance electrometer with low noise triax cables. QE measurements were performed using a Xenon arc lamp, monochromator, UV-enhanced fiber, and Stanford Research Systems (SRS) lock-in amplifier. The capacitances of diodes were measured by an Agilent 4980A LCR-meter. The consistency of the measured current levels, in the dark and illuminated cases, was confirmed by all the three current measurement made by these different experimental set-ups.

The IV measurement results in Figure 4.3 show that the zero bias dark current of a 200 μm diameter photodetector was 14 fA, and corresponding current density of 44 pA/cm^2. This current level corresponds to the background noise floor of the electrometer used for the experiments. At 1 V reverse bias, the dark current of the device was 20 fA and at 5 V it was 1.6 pA. The breakdown voltages of the photodetectors were measured to be higher than 120 V.

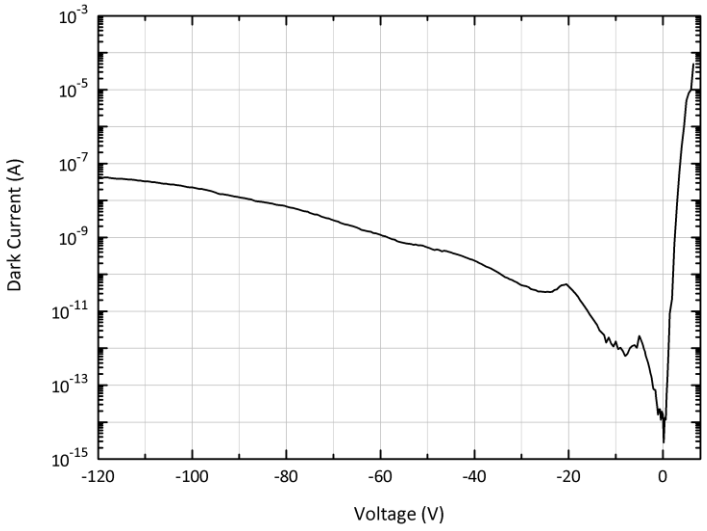

Figure 4.3: IV measurements of a photodetector with a 200 μm diameter.

The turn-on voltage of the fabricated device was around 3 V. The current level of the device for biases below 0.2 V was below the measurement limit. Therefore, a linear fit to the IV curve of the device was made for bias values from 0.2 V to 0.7 V. Using this linear fit, the ideality factor of the photodiode was calculated as n=1.97. The contact resistances were 0.75 kΩ for n-type contacts and 15.0 kΩ for p-contacts with 100 μm x 200 μm contact pads.

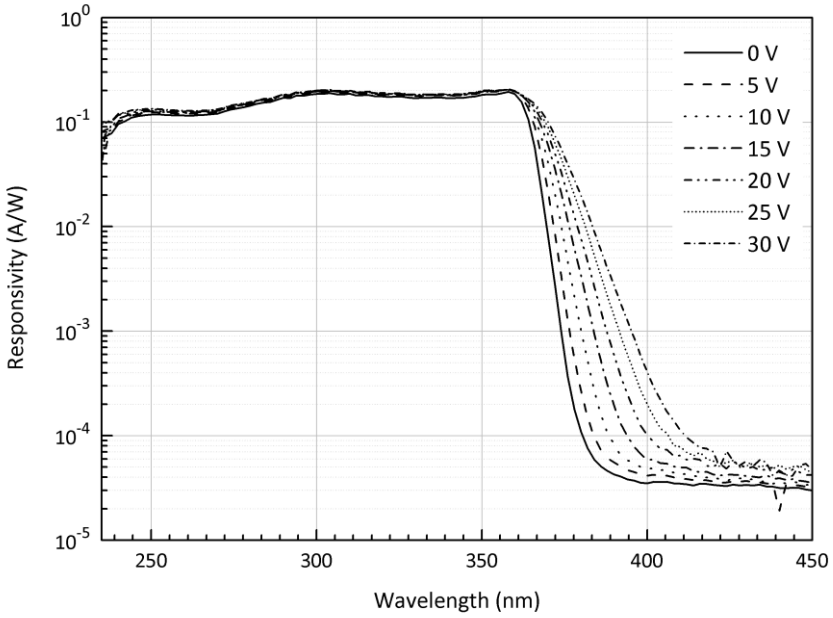

Figure 4.4: Responsivity of a 100 μm diameter photodetector for different reverse bias voltages.

We measured responsivity of 100 μm diameter diodes for bias voltages up to 30 V and observed a maximum UV-visible rejection ratio of 6.7×10^3 for wavelengths longer than 400 nm (Figure 4.4). Responsivity at 358 nm was 0.20, which corresponds to 70% quantum efficiency. For wavelengths below 360 nm, the responsivity of the devices did not significantly change with applied reverse bias

voltages larger than 5 V. Apparently, the diodes were depleted for small voltages, and to confirm this effect we performed CV measurements of the fabricated devices.

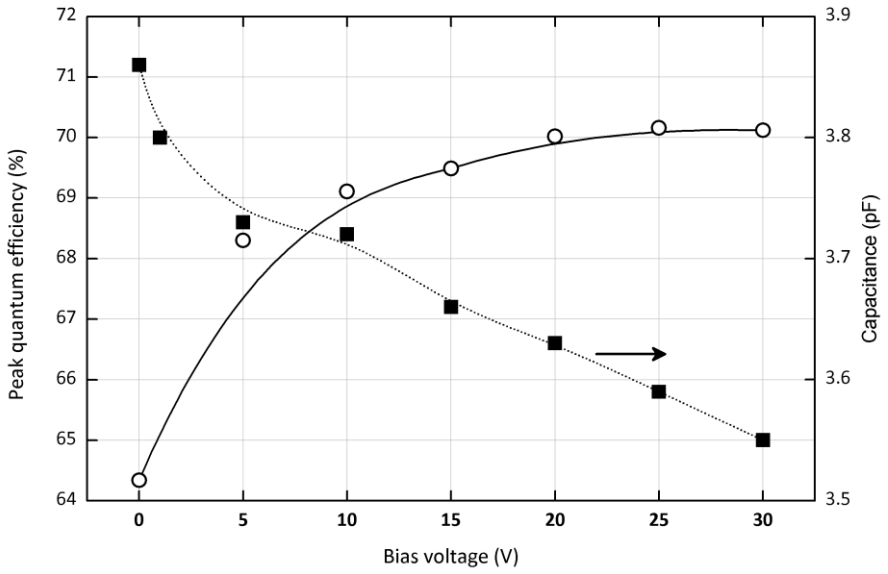

Figure 4.5: Voltage dependence of the quantum efficiency and capacitance for 100 μm diode.

Figure 4.5 shows the QE (at 358 nm) and the capacitance measurements of a 100 μm diameter device as a function of applied reverse bias. The QE quickly increased from 64% at 0 V reverse bias to 68% at 5 V reverse bias. For applied reverse biases larger than 5 V, the QE stayed almost constant with a maximum of 70 % at 30 V applied reverse bias. The capacitance of the 100 μm diameter device also had a similar dependency on applied reverse bias. The capacitance quickly dropped from 3.86 pF at 0 V applied reverse bias to 3.7 pF at 5 V applied reverse bias. Afterwards, the capacitance of the device slowly decreased to 3.55 pF as the reverse

bias voltage was changed to 30 V. This data clearly showed that most of the intrinsic region was already depleted at very low voltages.

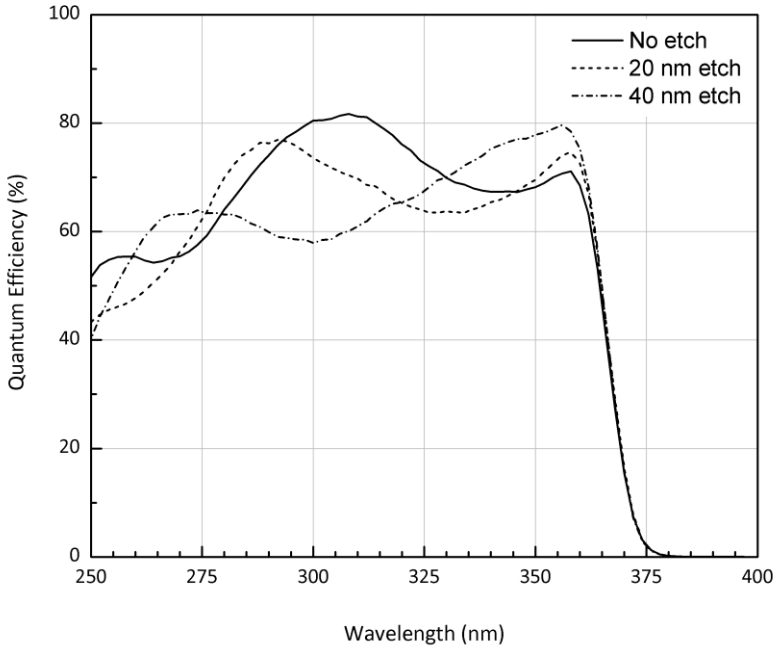

Figure 4.6: Spectral quantum efficiency of the photodetector after 0 nm, 20 nm and 40 nm recess etch of the top dielectric film.

Figure 4.6 shows that the peak QE of the fabricated device was at 300 nm under 5 V bias. This was in contradiction with the normally expected peak wavelength of 360 nm due to the band gap of GaN. This shift in peak QE wavelength can be explained with the additional optical phase coming from the finite thickness of the deposited dielectric layer. A similar shift was also observed in transfer matrix method (TMM) simulations of the QE for devices with varying top dielectric thicknesses. In order to confirm this explanation by experiments, the top Si_3N_4 layer was etched 20 nm with diluted HF:H_2O (~3ml:500ml) solution. Figure 4.6 shows the QE measurements after 0 nm, 20 nm and 40 nm recess etch of the top dielectric film.

After a total etch of 40 nm, the peak QE was measured to be 80.1 %, while the peak responsivity was 0.23 A/W under 5 V bias at 356 nm. To our knowledge, the 0.23 A/W responsivity value corresponds to the highest responsivity for the front illuminated GaN based p-i-n photodetectors reported in the scientific literature.

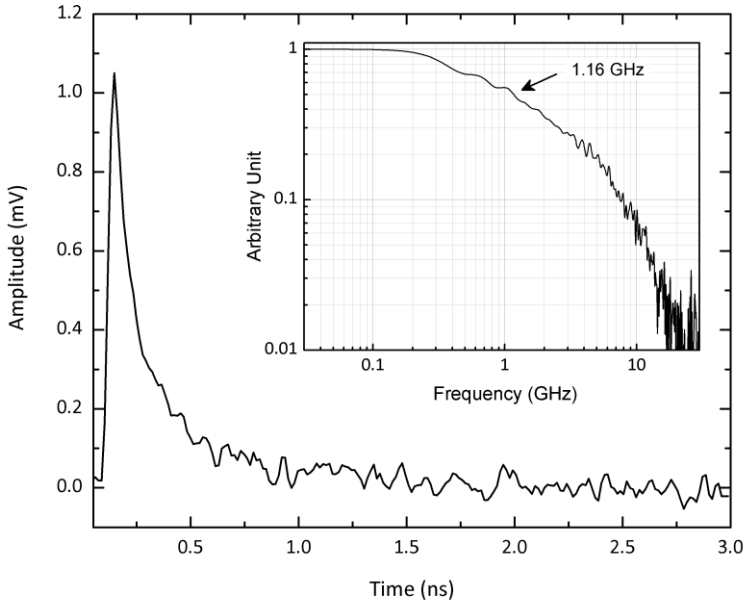

Figure 4.7: Temporal pulse response of the 100 μm diameter p-i-n photodiode under 5 V reverse bias voltage and the corresponding frequency response (inset).

Using an ultrafast mode-locked fiber laser module with output pulses at 266 nm and 10 ps full-width at half maximum (FWHM) pulse width, we performed the high speed (i.e. frequency response) measurement of fabricated p-i-n photodiodes. Figures 4.7 shows the temporal pulse response and the fast Fourier transform (FFT) of the p-i-n photodetectors. We measured 48 ps rise time, 351 ps fall time and 109 ps FWHM from a 100 μm diameter device under 5 V reverse bias voltage. From the FFT data, the corresponding 3-dB bandwidth was found to be 1.16 GHz. This performance is

close to the best 3-dB bandwidth of 1.6 GHz reported in the literature for GaN based p-i-n photodetectors.

With p-i-n structure, we have grown, fabricated and characterized high performance GaN based photodetectors. The optimized MOCVD growth conditions resulted in epitaxial samples that yielded high performance devices. A maximum 80.1% QE corresponding to 0.23 A/W responsivity at 356 nm, was achieved. The dark current of a 200 μm diameter circular diodes was measured to be 14 fA, along with a breakdown voltage larger than 120 V.

4.2 InGaN Light Emitting Diodes with Plasmonic Nanoparticles

GaN based light emitting devices are attracting attention due to several reasons which were mentioned before. In addition to them, the large bandgap property together with the InAlGaN compositions enable the scanning of the entire visible spectrum. At the same time, the strong chemical bonds make the material system very stable and resistant to high currents and intense illuminations [52]. Among these devices, InGaN based light emitting diodes (LEDs) have led to applications such as next-generation high density optical storage, solid-state lightning [53], various displays, traffic signals, backlighting for cell phones, exterior automobile lightning, and optoelectronic computer interconnects [54]. However, due to nonradiative recombinations, internal quantum efficiency in InGaN LEDs is well below 100 % [55], which is being increased by way of the development of growth techniques [56]. Another serious problem is the low efficiency of extracting the light outside the device, mostly due to the total internal reflection on the semiconductor-air interface. Unlike internal efficiency, the second problem requires more than one solution, and therefore, much work has been focused on enhancing external quantum efficiency

[57]. The first trivial solution was to build the LEDs with a hemispherical surface [58], which solves the total internal reflection problem but makes the device bulky. Recent works have focused on changing the surface properties of devices to couple more light to air, such as micro- and nano-roughening of the surface [54, 55], building nano-ring structures [59], texturing [57] and nano-patterning top metal [60], depositing metal islands on top surface [61], processing the devices by undercut sidewalls [62], and using nanoplasmonic structures on LEDs [63, 64, 65,66]. Apart from confining light to very small dimensions, plasmonics also offers new mechanisms in generating and manipulating light through surface plasmons (SPs) [67]. When these nanostructures are placed close to quantum wells (QWs) they significantly increase the density of the states and spontaneous emission rate [63, 64, 67].

In the present work, we focused on growing and fabricating high quality LEDs with InGaN/GaN QWs and depositing metallic nano-particles on top in order to increase their efficiency. The metal chosen was silver (Ag) for its relatively lower plasma frequency in optical wavelengths [68, 69].

4.2.1 LED Fabrication

The first step in the fabrication of LED epitaxy was to etch all the samples down to n+ layer, and then to deposit n-contacts with Ti/Al metals. Then, from n+ down to sapphire, the areas outside the devices were etched. This step is omitted in the some of the later fabrications, because we observed that this step creates extra current paths and recombination centers, decreasing LEDs' performance.

Subsequently, p-contact Ni/Au or indium-tin-oxide (ITO) with a thicknesses total of 800 Å (down to 100 Å possible) and 750 Å, respectively, was evaporated onto the lithographed samples. ITO coating is done with sputtering. This metal covers the entire top surface of the LED so that the metal must be transparent and thin, and then the touch pads with Ti/Au metals are deposited. The contacts are annealed at 550 ºC for 5 minutes for Ni/Au and at 650 ºC for 2 minutes for the ITO

contacts. After the touch metal, the dielectric is coated on the samples, and the openings for interconnects are etched. Dielectric material affects the plasmon resonance properties and adhesion strength of metallic particles [70]. Considering this, we chose to work with SiO_2. The last fabrication step is depositing Ti/Au metal in order to probe for electrical measurements (which may also be omitted for characterization).

The device areas in an optical lithography mask ranges from 160x160 μm^2 to 480x480 μm^2, which are actually quite large for later e-beam lithography. Mask and finished devices are shown in Figure 4.8 and 4.9. In e-beam lithography, the processed areas are smaller than the total emitting surface.

In Figure 4.10, the I-V characteristics of fabricated diodes are shown for different top p-contacts. It is clearly seen that devices with an Ni/Au top contact pass through more current at a given voltage than do devices with ITO top contact. This is due to Ni/Au contact to p+ GaN being more ohmic compared to an ITO contact. However, at these wavelengths, ITO is more transparent. Therefore, there is a trade-off between the contact quality and transparency for LED operation. As a solution, ITO contacted diodes have been processed for nanoparticle deposition. The turn-on voltages are around 2-3 V and the diode currents reach milliamperes around 5 V. Low temperature photoluminescence measurements show good InGaN QWs with transitions from n=1 and 2 electron levels to heavy hole level, as shown in Figure 4.11. In higher temperatures, the second transition disappears gradually since electron energy is transferred to nonradiative phonon scatterings from n=2 to the n=1 level. At room temperature charges at n=2 level does not make radiative recombination and we do not see this peak**.** This kind of behavior confirms the optimized growth during the QWs, as is clearly seen by the quantized energy levels in the InGaN layers. An atomic force microscopy (AFM) image of a grown wafer, Figure 4.12, indicates that all the crystalline imperfections during growth are gone, as the root-mean-square (RMS) roughness is at the atomic level of 0.11 nm. We conclude that InGaN LEDs were successfully grown and fabricated.

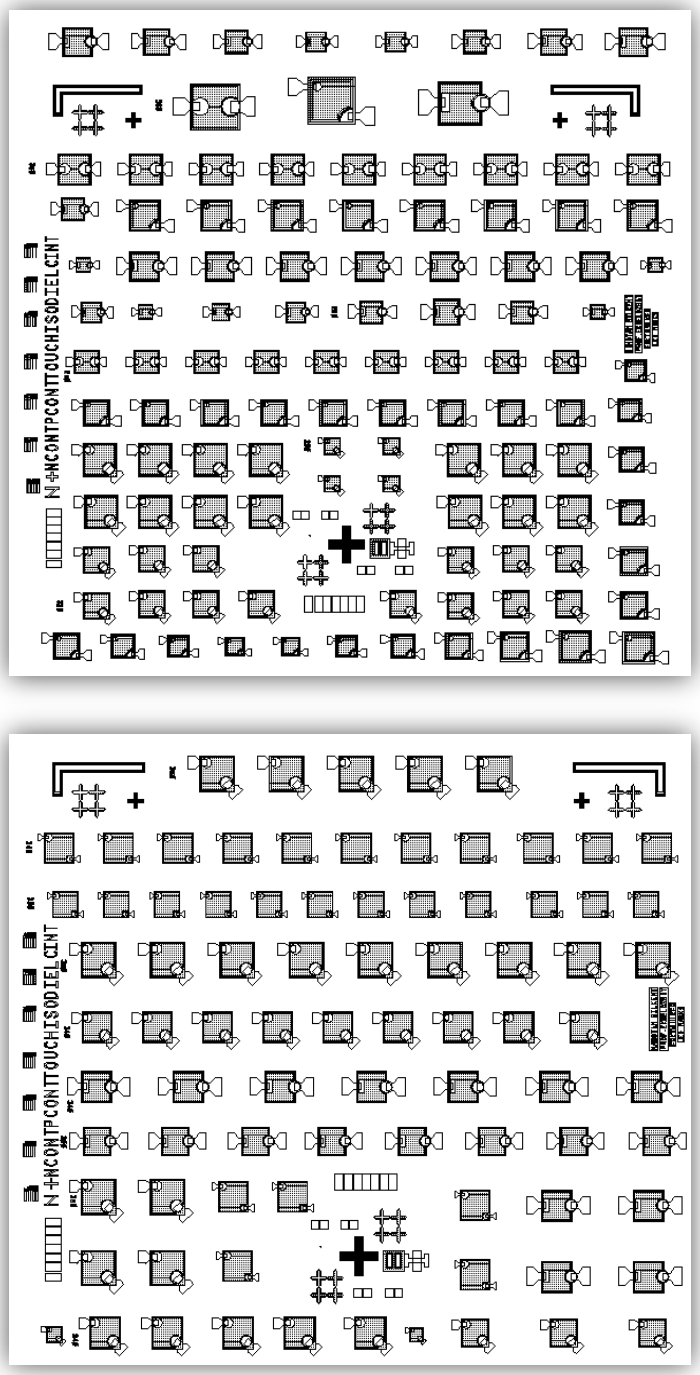

Figure 4.8: Two LED masks used in device processing.

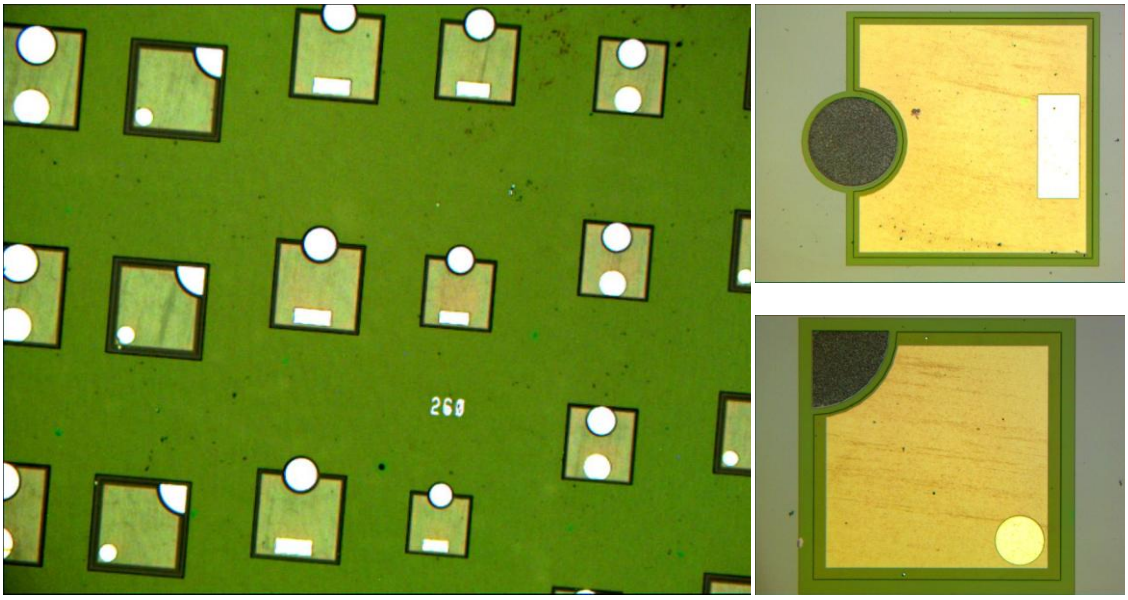

Figure 4.9: Fabricated LEDs.

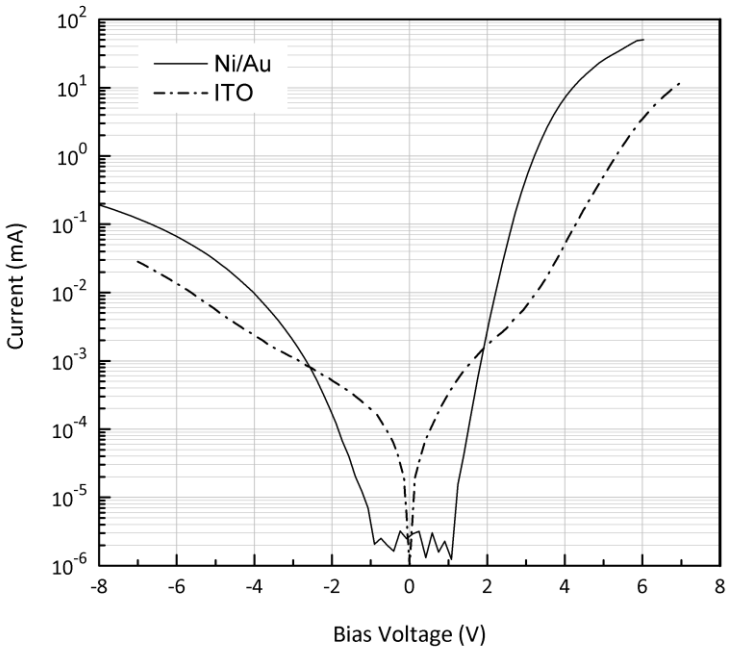

Figure 4.10: IV measurement of diodes with Ni/Au and ITO top metal contacts.

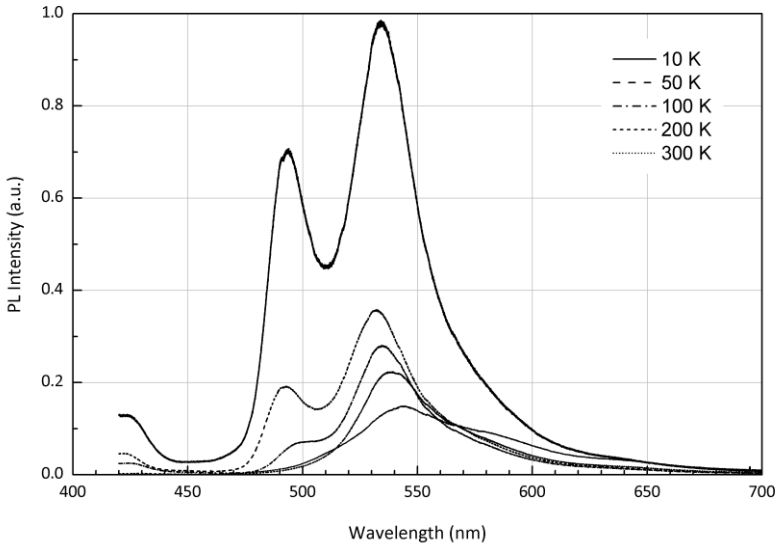

Figure 4.11: Low temperature photoluminescence measurement of InGaN/GaN LED wafer.

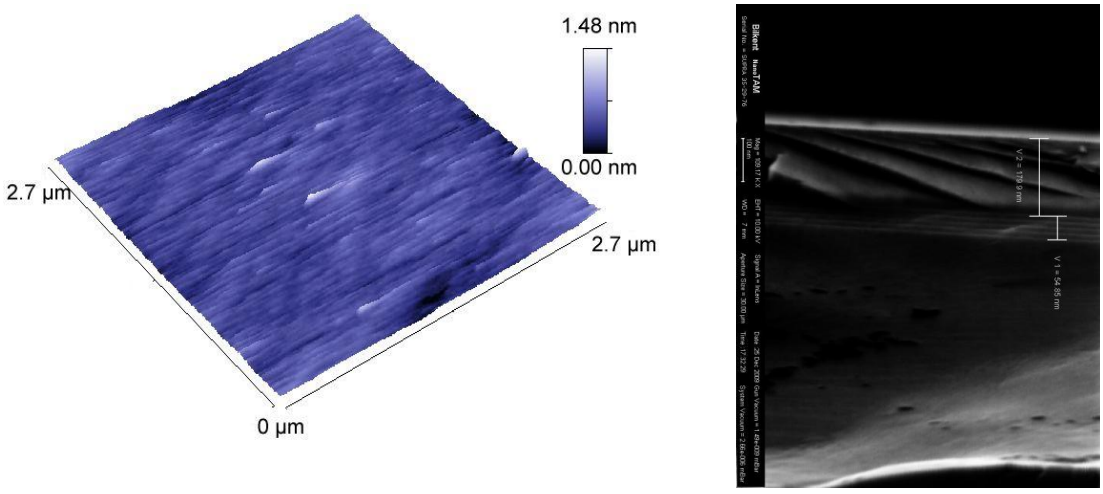

Figure 4.12: AFM and SEM images of the grown wafer. RMS of surface corrugations is approximately 0.11 nm.

4.2.2 Nanoparticle Design

Exploiting plasmon properties at very short wavelengths, typically shorter than 500 nm, is very challenging since this is well below the Localized Surface Plasmon (LSP) band of the usual noble metals used in plasmonics. Silver (Ag) was chosen over gold (Au) because of its shorter wavelength plasmon resonance. It is also possible to use aluminum (Al) or indium (In) for lower wavelengths.

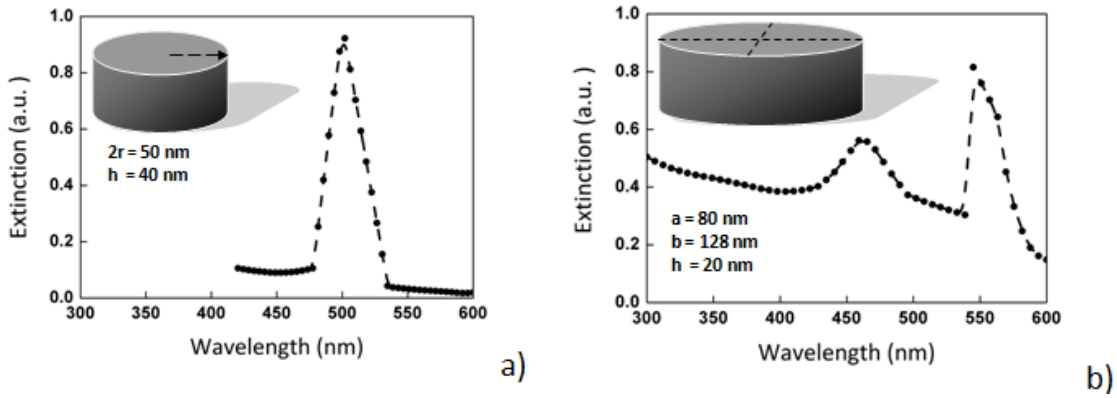

Figure 4.13: Simulation of extinction spectra of silver nanocylinders using Fourier Modal Method. Particles are on SiO_2 substrates. There is only one dipolar LSP resonance at 490 nm for a cylinder with circular base(a), and there are two resonances: dipolar at 560 nm and quadrupolar at 455 nm for a cylinder with elliptical base (b).

In order to design the Ag particles and optimize their resonant properties, simulations were performed using the Fourier modal method (FMM), which has been long plagued when metals are considered in optics [70]. In order to obtain reliable modeling, one should include the last refinements of the method. On the one hand, the scattering matrix algorithm prevents the difficulties linked to the growing evanescent waves, while on the other hand, the proper use of Fourier factorization rules allows for the proper writing of the boundary conditions, and therefore, faster

convergence. Without these recent ameliorations of the method, the modeling of the bi-periodic grating of Ag particles would have been intractable. The extinction spectrum of Ag nanocylinder grating on a SiO_2 substrate was simulated. In order to obtain the lowest resonance wavelength, we considered dimensions practical for our e-beam lithography set-up: cylinders with 50 nm diameter and 40 nm height. For InGaN LEDs with emission wavelengths at approx. 435 nm, the resonance of these particles were far from the diode emission wavelength, since for these parameters the localized surface plasmon (LSP) band is centered on 490 nm. Because smaller dimensions cannot be reasonably considered from the fabrication point of view, we opted for the use of nano-ellipsoidal particles and longer wavelength LEDs. By using the elongated particles, we expected to exploit the quadrupolar LSP resonance rather than the dipolar one. We ran the simulations for nano-ellipsoidal gratings, i.e. the cylinder with an ellipse base, lying on the SiO_2 substrate. Those ellipses are 20 nm high with an 80 nm long short axis and are 128 nm (=1.6×80) for the long axis. These parameters can be achieved with good reproducibility. In that case, it can be seen in Figure 4.13 that the extinction spectrum includes both a dipolar resonance, at 560 nm, and a quadrupolar one, at 455 nm. Although the higher order resonance is significantly weaker than the dipolar one, it may be sufficient to enhance the diode emission provided that the emission wavelength can be tuned down to this range.

4.2.3 Nanoparticle Deposition Process: E-Beam Lithography

In the first step of the e-beam process, Figure 4.14, a 120 nm Poly-methyl methacrylate (PMMA) layer is spin coated on top of the LED and baked for 1.5 hours at 170 ºC in an oven. Arrays of lines with period 300 nm and a total size of 100x100 μm^2 are exposed on top of the emissive areas. Different doses are considered in order to obtain ellipses with different aspect ratios, and therefore, the maximization of the probability overlapping the LSP band with the LED emission wavelength. Before depositing the 40 nm Ag, a thin 2 nm Ti layer is used to increase its adherence on SiO_2.

The dimensions of the ellipses obtained after the lift-off range from 140 nm to 170 nm for the long axis and from 70 nm to 80 nm for the short one as shown in the Scanning Electron Microscope (SEM) images in Figure 4.15 and Figure 4.16. Optical images taken under the transmission and reflection modes of an array of silver ellipsoids fabricated on top of one LED showed that we have faced some difficulties in obtaining full matrices. This is attributed to the challenge of obtaining small features with limited exposure parameters over rather large arrays.

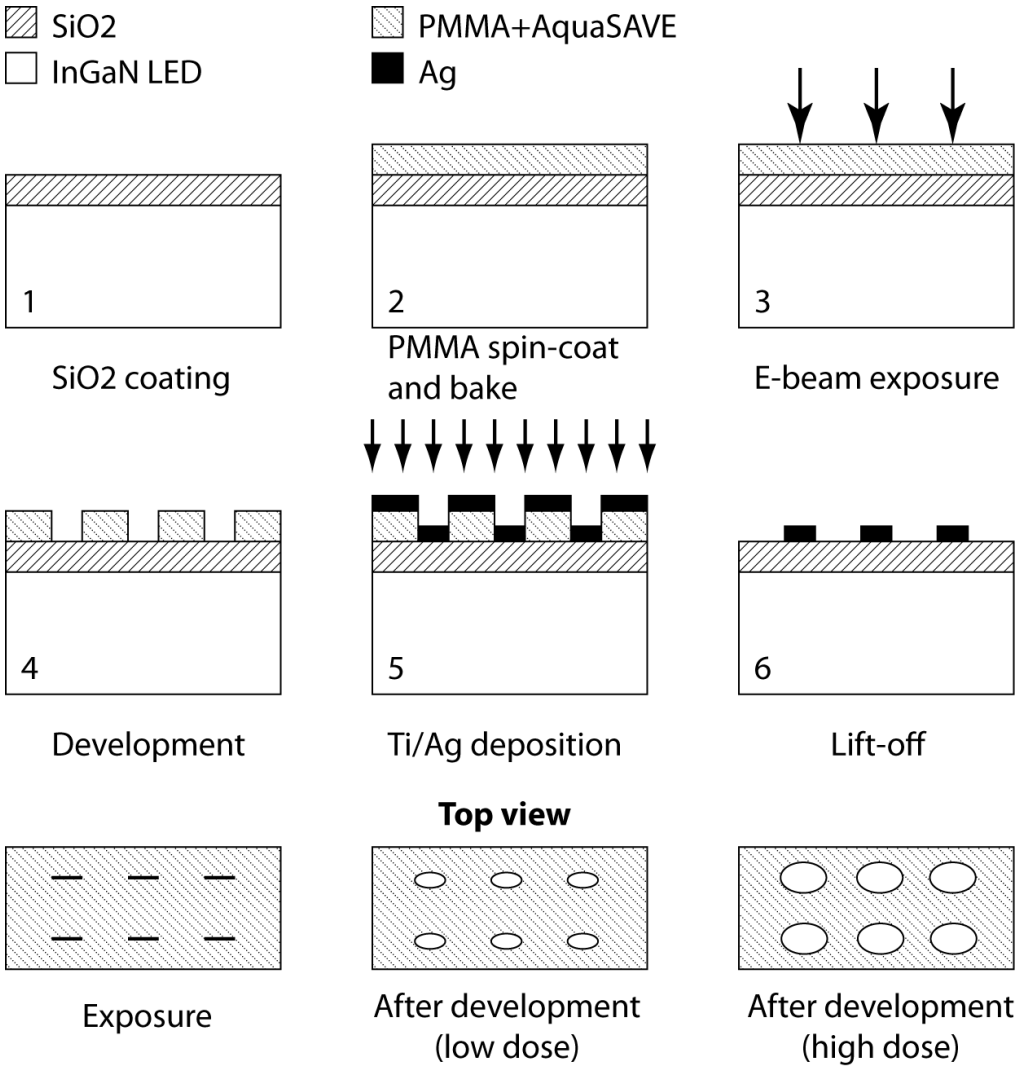

Figure 4.14: E-beam lithography steps.

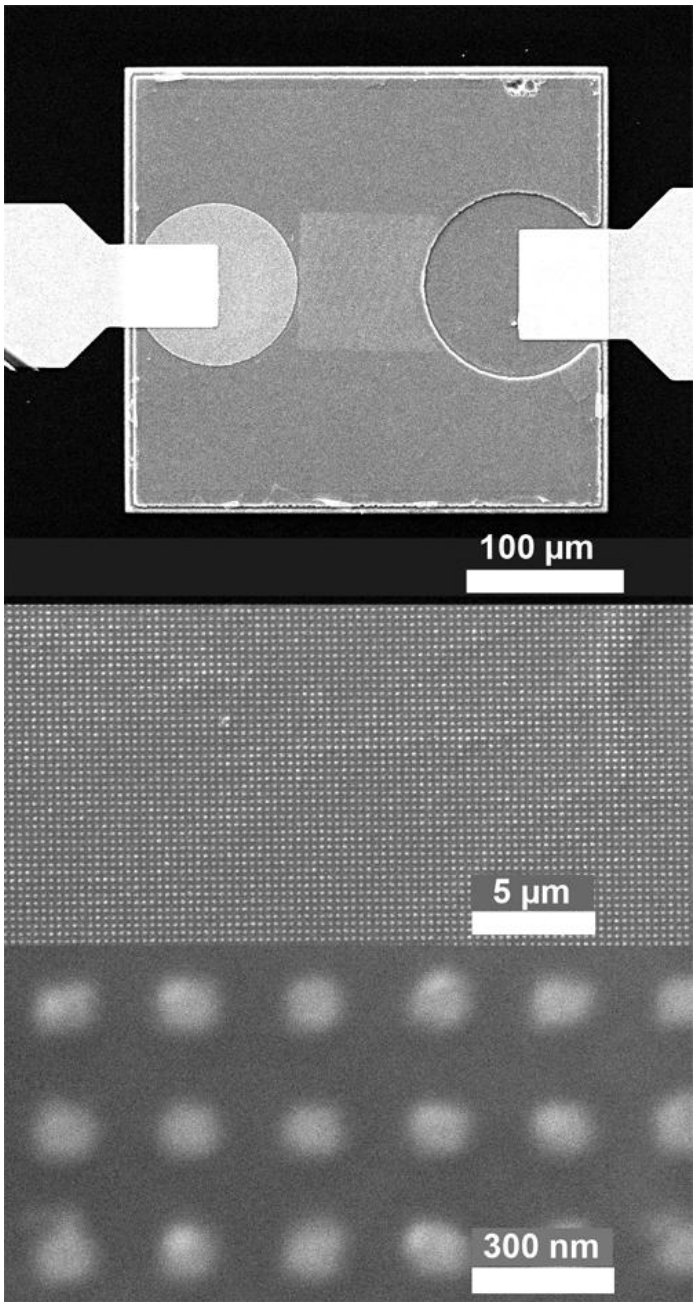

Figure 4.15: SEM image of fabricated LED and deposited nanoparticles in an area of approximately 100 µm x 100 µm.

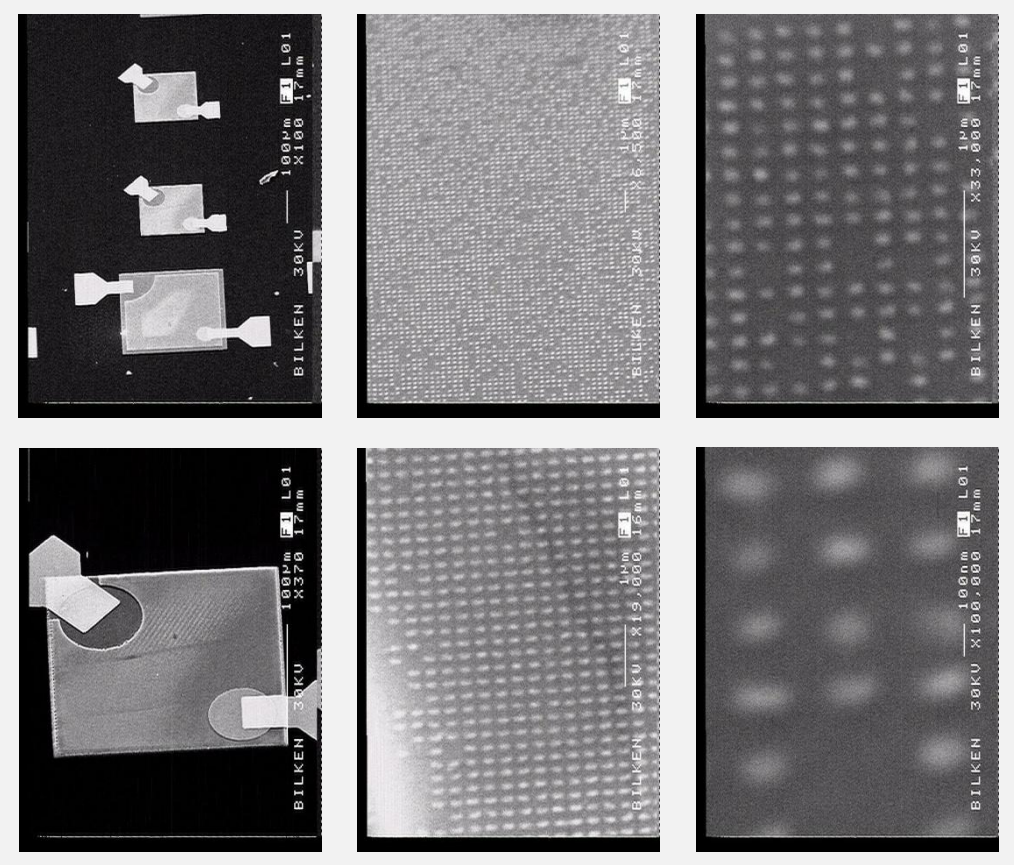

Figure 4.16: SEM images of particles and LEDs with gradually increasing zoom.

4.2.4 Results

The evolution of the light reflected by one nano-particle matrix as a function of the polarization of the incident white light illustrates the dependence of the LSP resonance of the nano-elliposoidal particles with regard to the incident field polarization as shown in Figure 4.17. This is confirmed by reflection spectroscopy measurements performed for two samples exposed with different doses where the dip is the signature of the resonance band. Note that the quadrupolar resonance seems to be too weak in the reflection, as change in the reflected light intensity as a function of polarization does not change much at 450 nm. On the other hand, the dipolar resonance with the shortest wavelength is observed in longer wavelengths than was

predicted with simulations. From 450 nm to 675 nm, the reflection aspect ratio increases gradually, which is an indicator of the fact that the resonance peak is predicted in higher wavelengths with the simulation.

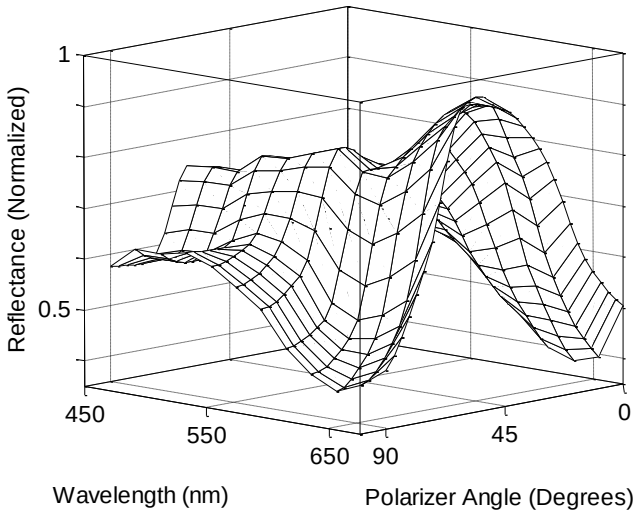

Figure 4.17: Change of reflection from nano-particle arrays as a function of incoming light in different polarizations and different wavelengths.

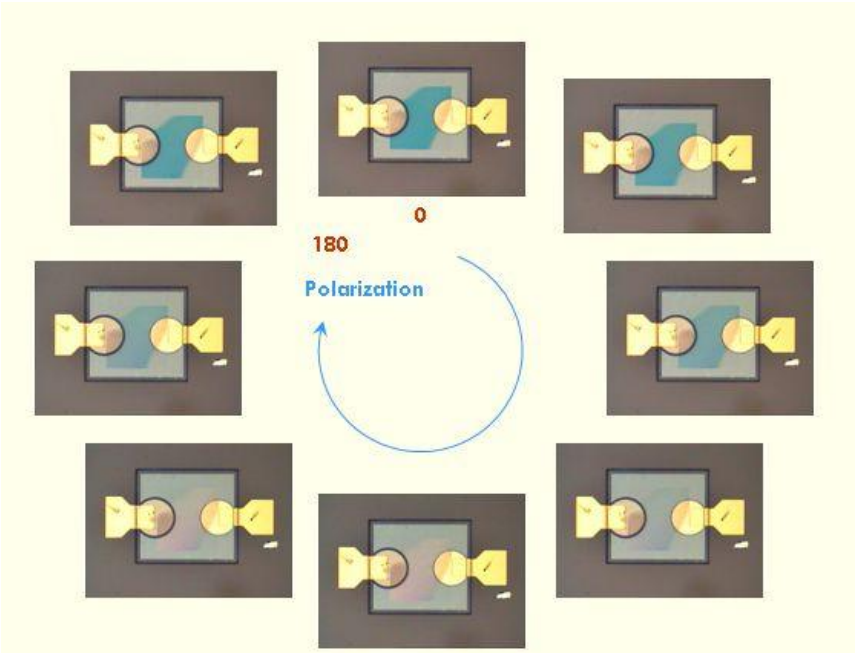

Figure 4.18: Changing of reflection with changing polarization.

We concluded that particle distribution, size, or particles to QWs distance [64] may not be as they should be, and that these together resulted in this shift. The electroluminescence of LEDs with nano-particles also did not show the enhancement on the patterned areas at moderately low emissions. We measured PL spectra at areas without particles and with particles. The luminescence peaks exhibited slight red shift in areas with particles; however the amount of shift is not large enough to conclude that particles are affecting the emission wavelength.

We successfully fabricated high quality LEDs and metallic nano-particle arrays with nano-level controllable shapes. We also investigated the possibility of integrating the periodic arrays of nano-particles in the UV-visible range. Polarization measurements on the fabricated samples illustrated the dependence of the LSP resonance of the nano-elliposoidal particles with regard to the incident field polarization. These results show the feasibility of plasmon-assisted LED emission enhancement.

We grew an InGaN/GaN based light-emitting diode (LED) wafer by metal-organic chemical vapor deposition (MOCVD), fabricated devices by optical lithography, and successfully deposited ellipsoidal Ag nano-particles by way of e-beam lithography on top. The diodes exhibited good device performance, in which we expected an enhancement of the radiated intensity by the simulations and emission measurements. The obtained results showed the feasibility of plasmon-assisted LED emission enhancement.

4.3 Nanopillar Light Emitting Diode Process for Light Extraction

The motivation behind this work was to fabricate nanopillar light emitting diodes (LEDs) and investigate the effect of size distribution and interparticle distance (pitch or period) to the emission spectrum. Also, the extra reflection from pillar sidewalls would enhance extraction, though we lost some of the emitting area in the etching process.

The general structure of LEDs are as in Figure 4.19. The quantum wells are etched through down to n+ layer so that each LED is isolated from others electrically. It is also possible to stop etch before quantum wells to use all emission area, however that way only surface corrugation effect would be seen. This is one of the plans for future work, but this kind of work, surface corrugation, was already been studied. In our case, we have been trying to fabricate nanosize LEDs and LED arrays.

We want pillars having as high aspect ratios as possible. In the bottom of Figure 4.19, the actual profile after etching is shown. The reason for this will be given later. Typical pillar width dimension of an LED was designed to be more than 90 nm, which is half the optical wavelength of emitting light inside GaN structures, so that guiding is achieved. In addition to that, the pillars in the vicinity will reflect lateral modes in the nano pillar area. The periodicity of array will behave as a photonic band gap for LED's emission wavelength by a careful design. These can be seen in Figures 4.20 and 4.21.

Another effect we try to observe is the narrowing of the radiation spectrum, due to sizing effects. This can be considered analogous to widening of pulses due to the dispersion in multimode fibers. In a way we are trying to make LEDs spatially single mode.

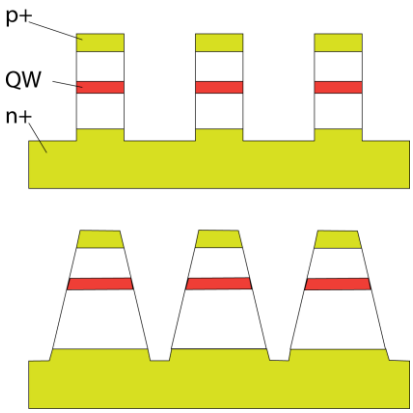

Figure 4.19: Schematic for pillar LED structures. The actual pillar profile becomes as in bottom figure due to the nature of reactive ion etching.

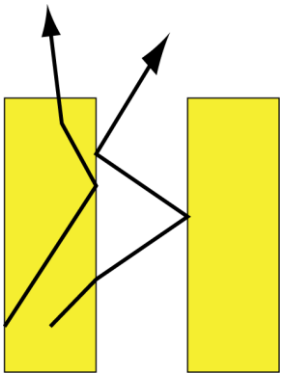

Figure 4.20: Two mechanism of light extraction in pillars: reflection from own sidewalls, and neighbor pillar's sidewalls.

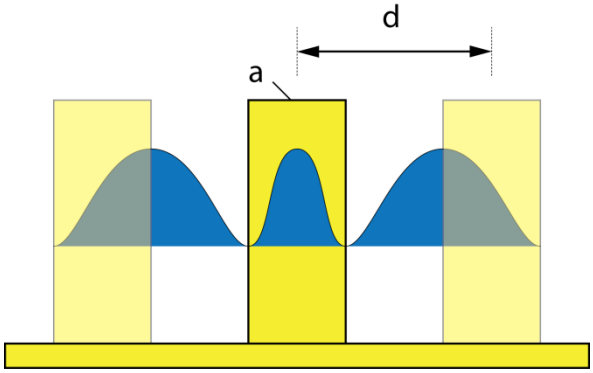

Figure 4.21: Mode distribution inside and outside of a single pillar, with size a, considering the effect of the interpillar distance, d, on coupling.

First we have tested whether it will be possible to obtain the desired aspect ratio. By aspect ratio, we roughly thought that, while width of pillar is in the range of 100 nm, height should be at least 300 nm so that both top p+ layer and QWs would be etched away. This is necessary if we like to make each pillar an electrically driven LED, which we still need to figure out how to do. We patterned LED surface with 1-2 μm square features by e-beam lithography, chrome (Cr) coating and lift-off processes. Then we etched the surface by Reactive Ion Etching (RIE) using freon (CCl_2F_2) gas as etchant. We have tried two different RF power levels and two different pressures, as these are the most effective parameters of anisotropy. As you

can see in Figure 4.22, low RF power level and low pressure resulted the steepest features. This process would be further optimized, however for now, this quality is enough for our preliminary purposes.

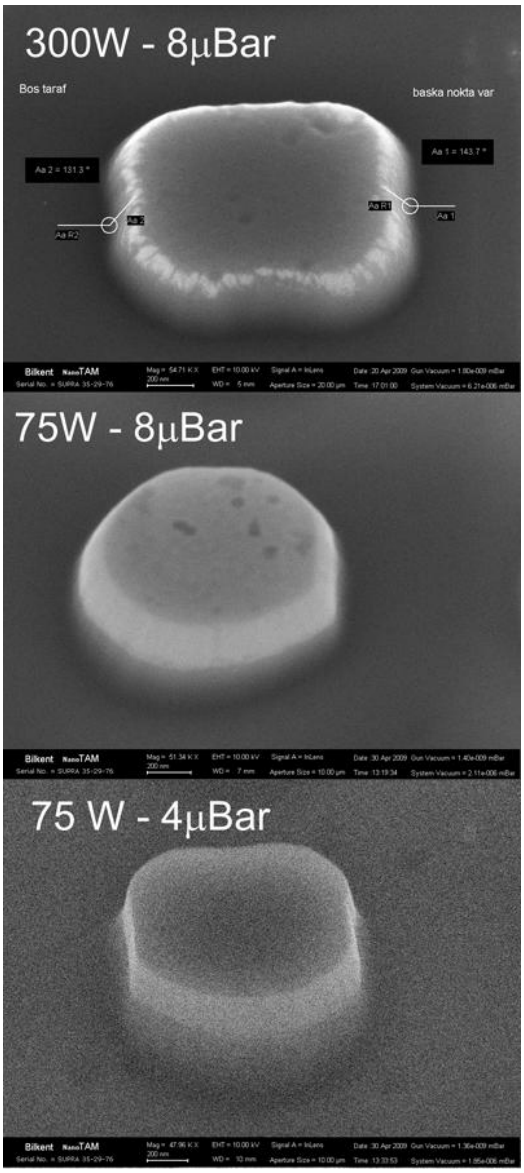

Figure 4.22: Etch profiles of 2 μm (top) and 1 μm size features with 2 different RF power and pressure levels. CCl_2F_2 flow rate was 20 sccm, and etch depth with 20 min duration was about 500 nm.

Then we designed an e-beam lithography mask with the features shown schematically in Figure 4.23. We designed square and circular base pillars with sizes a = 90 nm, 150 nm, and with periodicities of d=225 nm, 300 nm, 450 nm, and 675 nm.

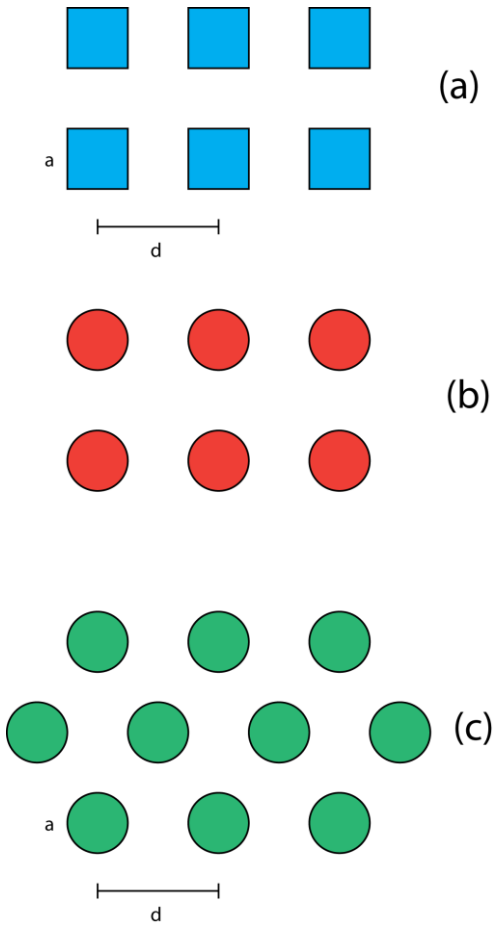

Figure 4.23: Three different trial etch masks, square pillars square array (a), circular pillars square array (b), and circular pillars triangular array (c).

In Figure 4.24 on the left, 90 nm Cr squares after metal lift-off process is shown. After etch, the different periodicity and pillar shapes (columns) and different doses (rows with x1, x1.2, x1.4, x1.6 doses) are shown.

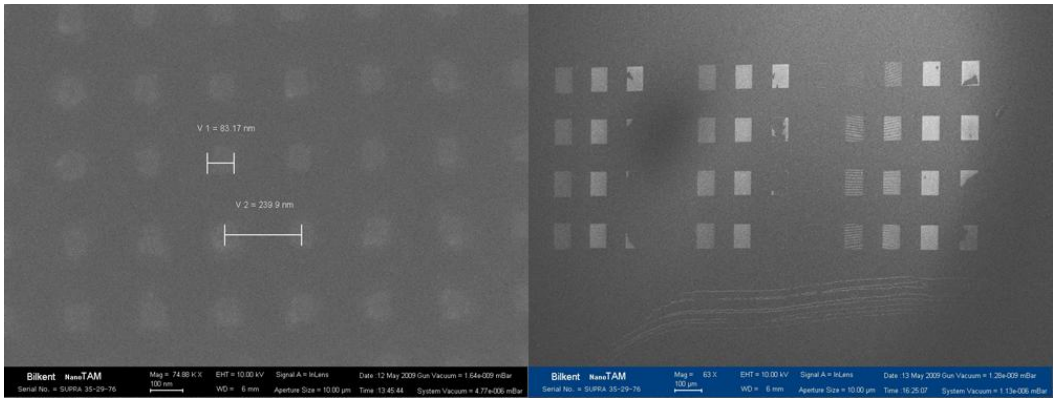

Figure 4.24: Sample surface after chrome lift-off (left), and after etch with zoom-out version (right).

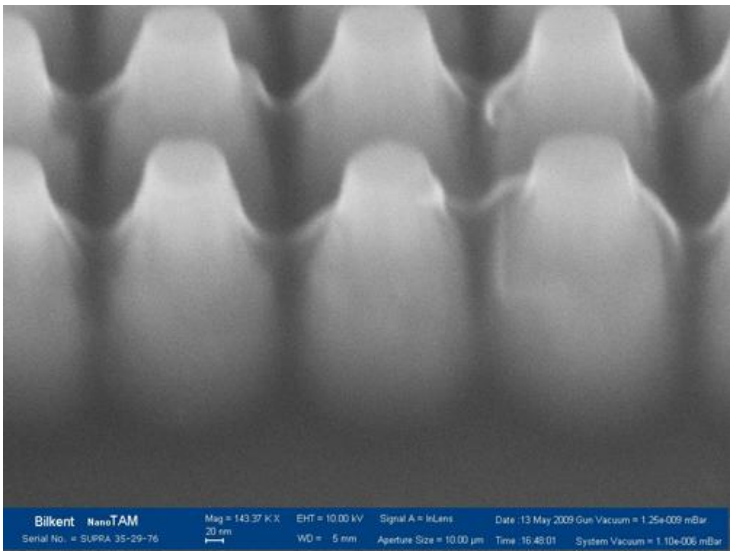

Figure 4.25: Square pillars with 90 nm width, 225 nm pitch and ~350 nm height.

In Figure 4.25, the close-up SEM image of pillars is shown. The sidewalls are not completely vertical. The reasons for this is that in RIE process, the ions are probably scattering from the points they impinge on, meaning sticking coefficient is not zero, and also the pressure inside affects the mean free path of ions with

collisions. Last reason that can be thought of is that the transfer of ions and resultant etched particles can not go away from the wells between pillars, i.e. the process is mass transfer limited. As the etch continues the sidewalls are less etched, resulting the structure as seen in above figure.

The samples are coated with AquaSave; a conducting thin film spun on samples which is soluble in water. This film seems to fill the array trenches, which is also visible in SEM image. To see better, it is possible to coat surface with a very thin Au layer, which is possible only after all measurements were done.

The other images from different arrays are shown in Figures 4.26, 27 and 28.

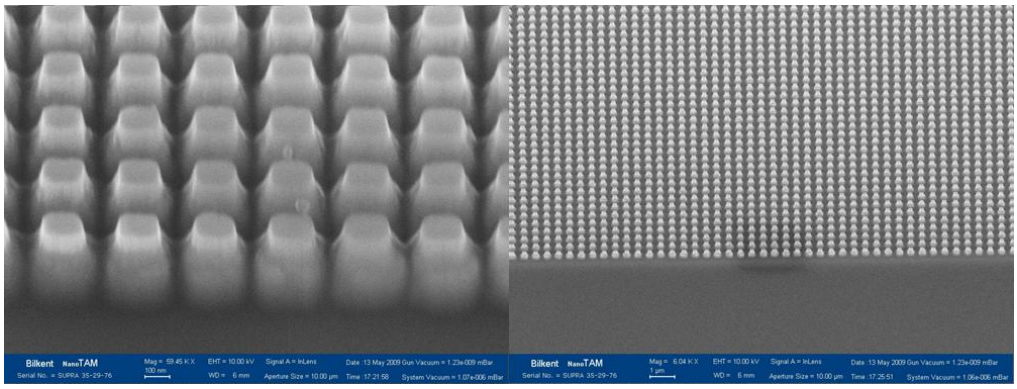

Figure 4.26: Square pillars with 150 width and 225 nm pitch.

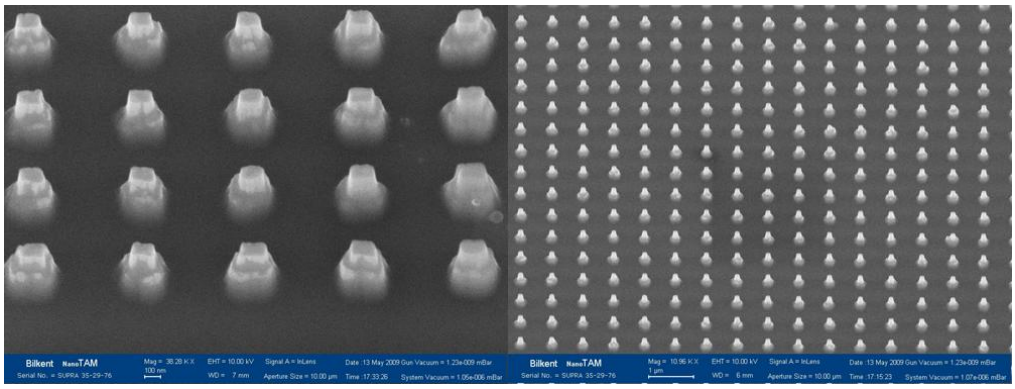

Figure 4.27: Square pillars with 150 nm width and 450 nm pitch.

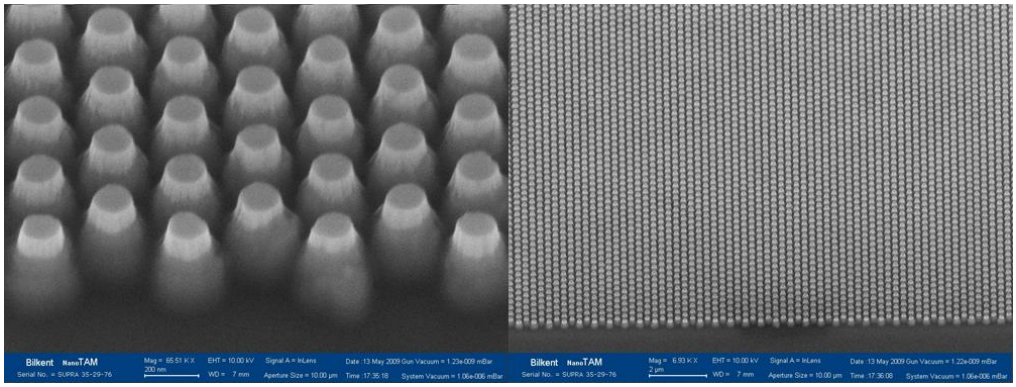

Figure 4.28: Cylindrical pillars with 90 nm width and 225 nm pitch values.

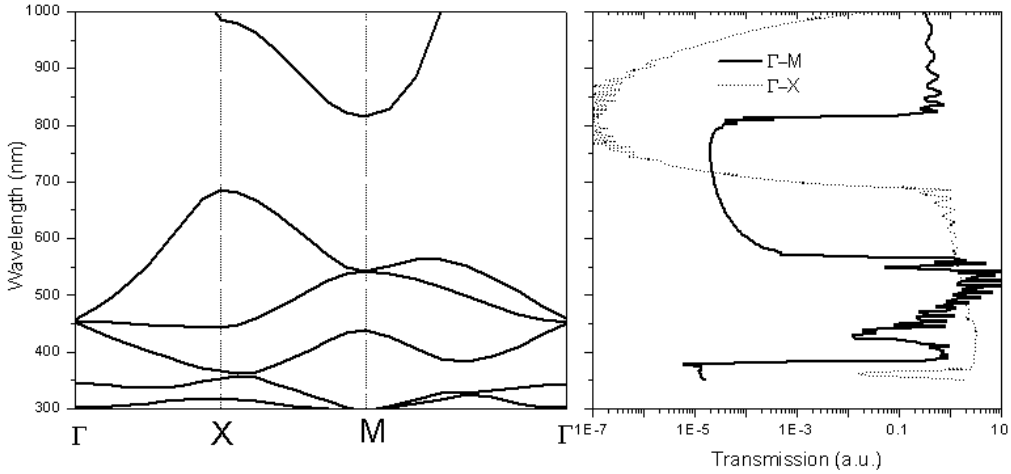

Figure 4.29: Photonic band diagram and transmission in crystal plane spectrum simulations of square lattice GaN pillars having 150 nm diameter and 300 nm pitch.

In Figure 4.29, photonic band diagram and transmission of square pillars are shown. The transmission here is simulated in the photonic crystal plane. The bandgap is simulated using RSOFT BandSOLVE [71] and transmission is simulated by Lumerical FDTD [72]. Looking at these graphs, we observe that there is a bandgap for wavelengths at 750 (±50) nm, so at this wavelength we expect light, incident perpendicularly to the sample surface, transmit completely. At 500 nm,

since all modes in crystal plane are supported to propagate, we expected to see a dip in perpendicular transmission spectrum.

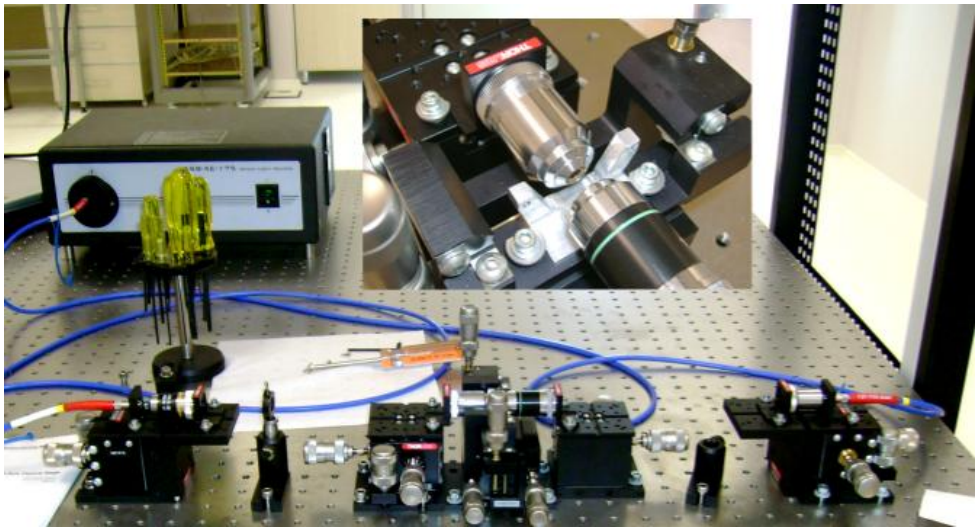

Figure 4.30: Transmission measurement set-up.

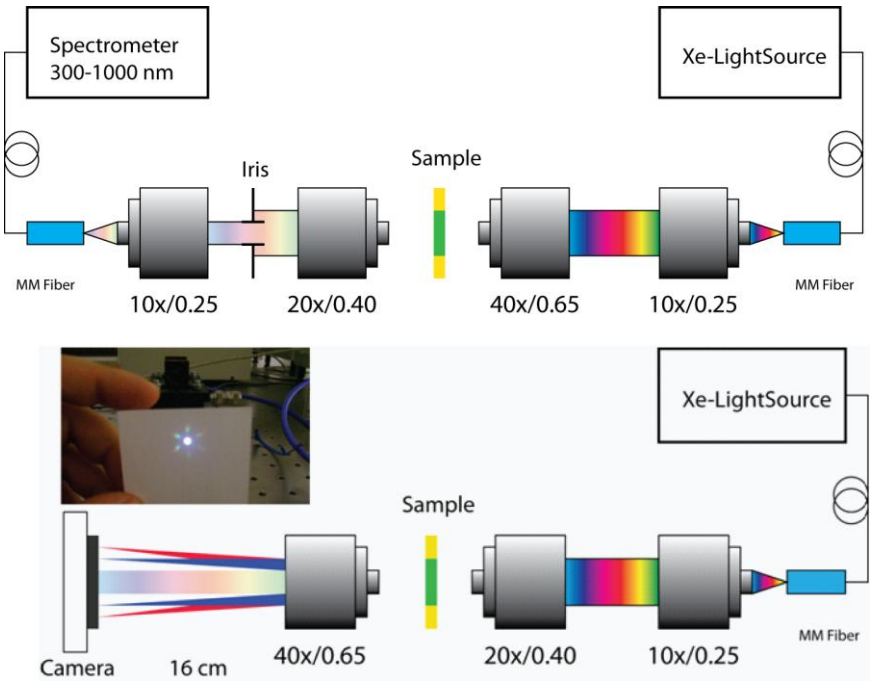

Figure 4.31: Transmission set-up schematics.

In Figure 4.30, the transmission and diffraction capturing set-up is shown. The schematics of set-up is given in Figure 4.31.

Figure 4.32: Transmission mode diffraction photograph of photonic crystals.

As discussed above, non-propagating modes in photonic crystals are expected to diffract and it is possible to see these waves using a simple imaging system. The set-ups shown in Figure 4.31 are used both for transmission measurements in the range 300-1000 nm, and used for imaging diffraction. The far field image of photonic crystals is also identical to the Fourier transform of photonic crystal geometry. Calculating the transformation parameters are straightforward once lens' (or objectives') focal length, screen (camera) distance and photonic crystal parameters known. It is also possible to extract crystal geometry with a high resolution using basic Fourier optics. In Figure 4.32, diffraction pattern photograph is

shown which is taken from a white screen. A camera is put instead of the screen and images in Figures 4.33 and 4.34 for triangular and square crystals are taken respectively. In Figure 4.35, surface-normal transmission measurement spectrum is shown.

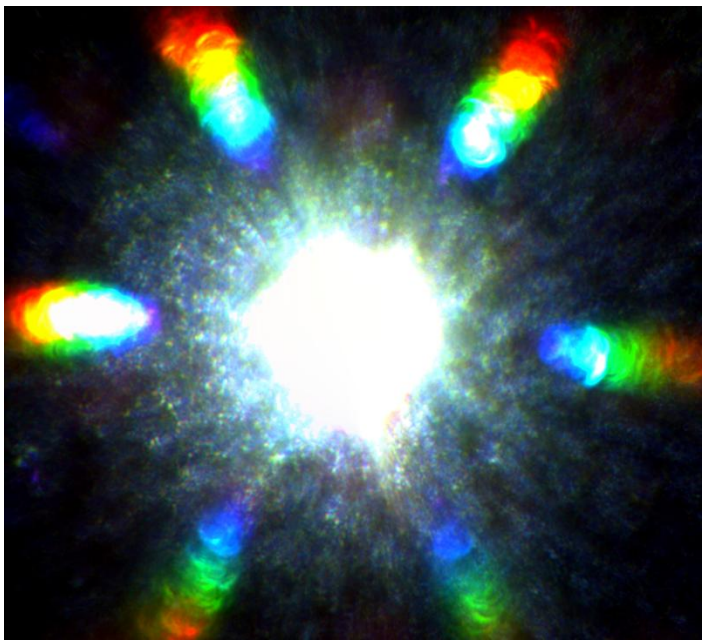

Figure 4.33: Diffraction pattern of GaN triangular lattice 150 nm diameter and 300 nm pitch.

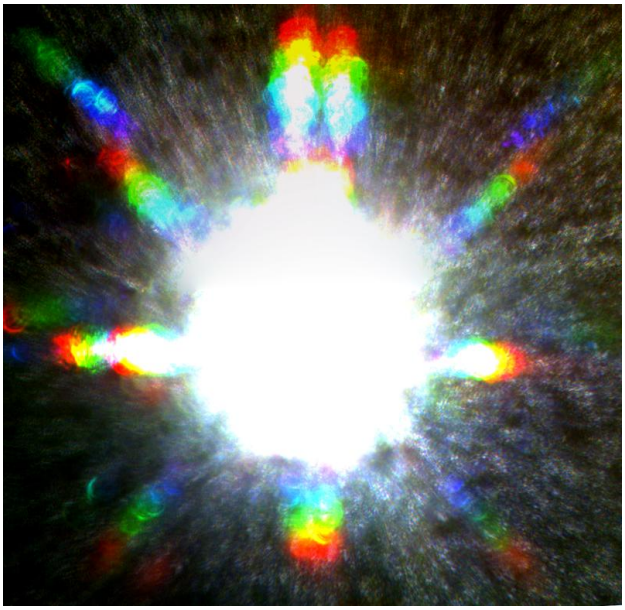

Figure 4.34: Diffraction pattern of GaN square lattice 150 nm diameter and 300 nm period.

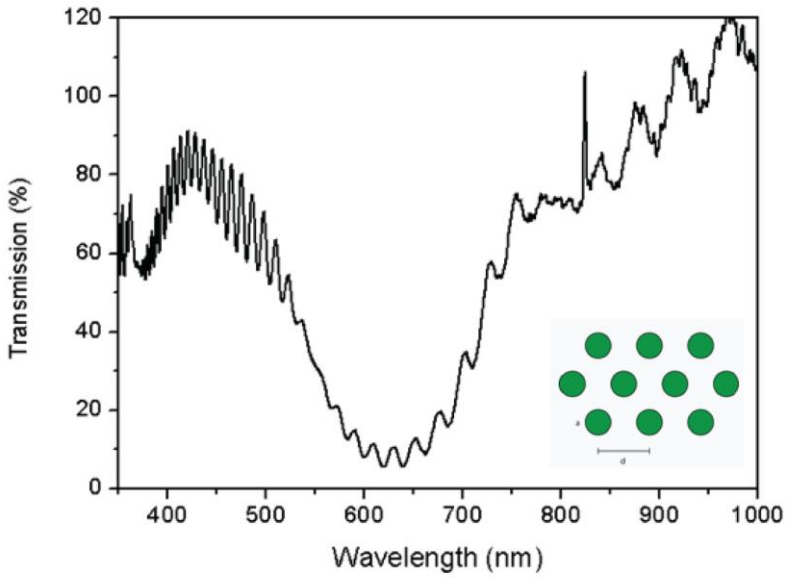

Figure 4.35: Transmission spectrum of triangular crystal pillars in surface-normal incidence.

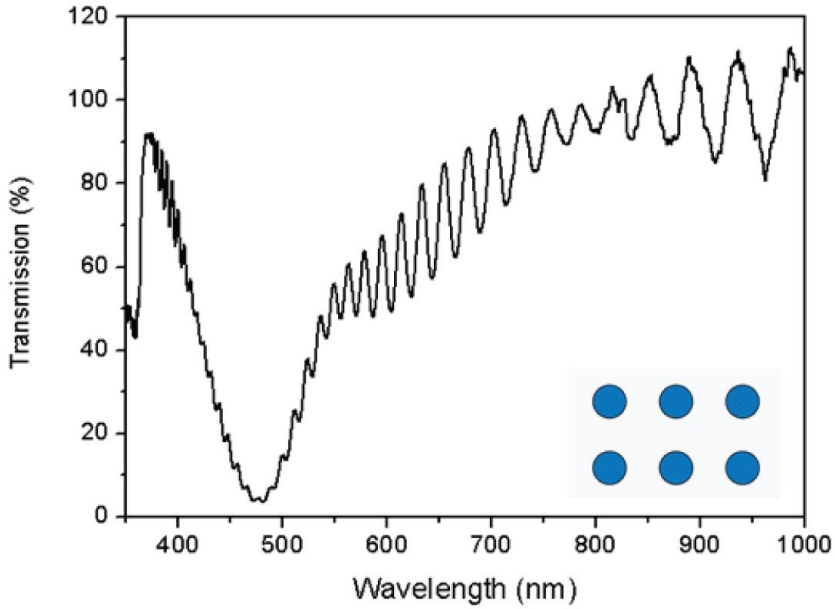

Figure 4.36: Transmission spectrum of square crystal pillars in surface-normal incidence.

The spectrum shown in Figure 4.36 is in complete agreement with Figure 4.29. This kind of structure is considered to be useful for wavelength multiplexing applications and surface normal laser actions. Also by putting these on an LED, it is possible to extract encapsulated light in the structure to air. Similar works have been demonstrated in the literature.

4.4 Towards Hybrid Nanophotonic Light Sources

We reported a compact light source that incorporates a semiconductor light emitting diode, nano-structured distributed feedback (DFB) Bragg grating, and spin coated thin conjugated polymer film. With this hybrid structure, we transferred electrically generated 390 nm ultra-violet light to an organic polymer via optical pumping and out-couple green luminescence to air through a second-order DFB grating. We

demonstrated the feasibility of electrically driven, hybrid, compact light emitting devices and lasers in the visible range.

In recent years, conjugated polymers have attracted much interest due to their high luminescence quantum yield [73], easy synthesis, broad and chemically-adjustable emission wavelength range in the visible spectrum [74], minimized self absorption due to very weak sub-band gap absorptions [75], and low cost [76]. Near zero self-absorption above the absorption edge and rather low energy thresholds for amplified spontaneous emission (ASE) makes them rather attractive for wavelength conversion with high throughput and novel laser devices. It is also possible to dope them with other chromophores [77] for multimode operation or to obtain tunable organic lasers via continuous modification of the grating used in the devices [78]. White light generation using a commercial light emitting diode (LED) as a pump and a polymer as the white light luminescent layer [79,80,81**]** was also reported.

Optically pumped laser action in conjugated polymers and copolymers has been demonstrated with an emission across the whole visible spectrum (blue, green, and red) and for different resonator geometries (microcavity, distributed feedback (DFB), distributed Bragg reflector (DBR), etc.) by several research groups [82**,**83,84,85,86,87]. Although high efficiency organic LEDs are now achievable, the development of electrically pumped organic lasers remains an outstanding and up to now unsolved challenge. One fundamental reason for the failure is, first, the high current density needed to realize an electrically pumped, amplified spontaneous emission, and second, the presence of metal contacts (electrodes) that cause a big portion of optical loss. Finally, the charged states of the organic materials (polarons, bipolarons) which are generated during the charge carrier injection at the electrodes also absorb light, and therefore, increase the energy threshold for amplified spontaneous emission. The realization of an organic material-based diode laser requires a complex optimization of optical and electrical properties of all components as well as of the device geometry. Regarding inorganic materials, epitaxially grown GaN-based inorganic semiconductor structures have found their

application as efficient, robust, visible- and ultraviolet (UV) light sources. GaN structures offer excellent electrical properties [88] but their spectral coverage is limited. However, down-conversion with phosphors enables access to other colors and white-light emission. Although blue emitting III-V semiconductor laser diodes (GaN, InGaN) have recently been proposed as a pump source for organic materials [81,89,90,91], it is noteworthy that there have been no reports to date of a compact, integrated device such as the one proposed in the present work that may pave the way towards color-tunable LEDs and inorganic/organic hybrid lasers. Hybrid light emitting devices incorporating GaN light sources with organic polymers was previously reported [79, 81]. Hide *et al.* used lenses to focus light emitted from a GaN LED [79]. Heliotis *et al.* stacked GaN LED and organic polymer coated on top of a quartz substrate [81]. Our structure is a compact light emitting device where organic polymer is coated on top of GaN LED and includes a filtering feedback mechanism based on distributed gratings.

Taking into account that lasing thresholds of polymer DFB lasers are now commonly low enough to be pumped by pulsed microchip lasers [92], we tested the combination of a GaN-based LED as light source and polymeric laser materials imbedded in a suitable grating structure in order to develop a compact light emitting device structure with a future potential for electrically pumped organic lasing. In the present work, we first grew and fabricated a UV-visible InGaN/GaN LED. We then patterned nanometer sized DFB gratings on top of the device by focused ion beam (FIB) milling technique, and coated the entire surface with the conjugated *para*-phenylene-type ladder polymer MeLPPP that is known for its low ASE threshold (A maximum ASE cross-section of ~1.5×10^{-16} cm^2 was observed at a wavelength of 490 nm). In this device configuration, the polymer was pumped by GaN-based LED, and the second order Bragg grating selectively coupled the down-converted photons to air.

4.4.1 LED Structure Growth and Fabrication

LED wafer was grown on a c-plane (0001) sapphire substrate by the AIXTRON RF200/4 Metal-Organic Chemical Vapor Deposition (MOCVD) system [93]. First, a GaN nucleation layer was grown followed by a 500 nm thick GaN buffer layer. Then, an n+ GaN layer was grown, and 5 pairs of InGaN/GaN were grown with a total thickness of 80-100 nm. To increase the charge recombination and enhance the light output, a 20 nm thick p-doped AlGaN layer was grown before the p-doped GaN top layer.

Diodes are fabricated standard micro-fabrication techniques [94]. Since GaN based structures are best processed via reactive ion etching (RIE) instead of wet etching techniques, all of the etching steps were performed before any metallization. First, wafer was etched down to the n+ layer, and with mesa mask. Later on, it was etched down to the GaN buffer. Thereafter, 10/100 nm thick Ti/Au metals for n+ ohmic contact, 75 nm thick Indium Tin Oxide (ITO) for p+ ohmic contact metals were deposited by evaporation and subsequently lifted off. The contacts were annealed at 650 °C for 2 minutes. The touch pad to p+ contact was 10/100 nm Ni/Au and the contact pads for the measurements were thick Ti/Au metals. Before the contact pad, the diode surfaces were coated with insulating dielectric films of SiO_2 using plasma enhanced chemical vapor deposition (PECVD) and etched by an HF/H_2O solution. The LEDs on the sample have areas ranging from 160x160 μm^2 to 480x480 μm^2. Fabricated LEDs have turn-on voltages of approx. 5 V with 1 mA forward current. At 6 and 7 V, the current levels were 9 mA and 29 mA, respectively. Figure 4.37 displays the electroluminescence (EL) spectrum of GaN LED device under test. The emission peak appears at 390 nm.

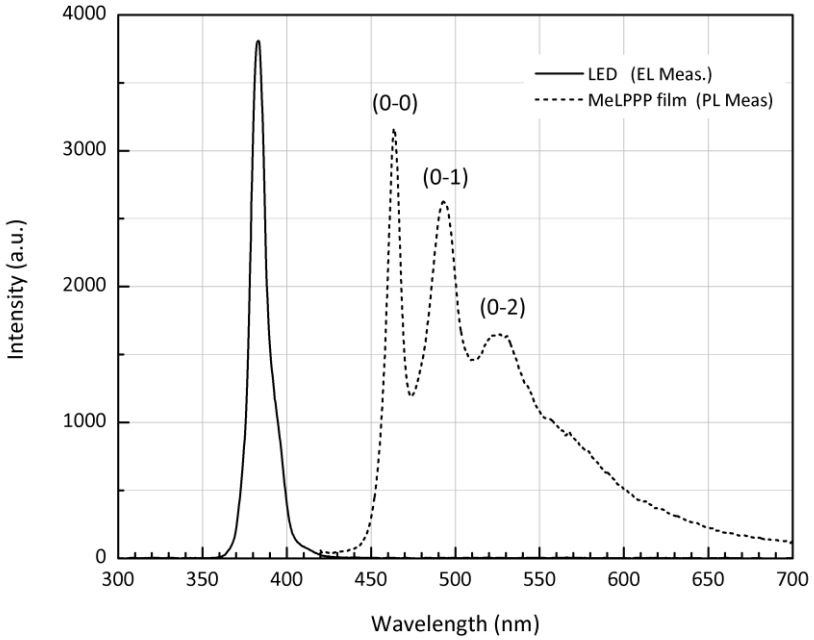

Figure 4.37: Electroluminescence spectrum of fabricated GaN LED and photoluminescence spectrum of organic MELPPP layer on top of a sapphire substrate.

4.4.2 Organic Polymers: Basic Physics, Synthesis and Application

The emitter polymer that was used in our study was a *para*-phenylene ladder polymer MeLPPP [73], which is a fully planarized, rigid conjugated polymer without any considerable conformational distortion. Together with its high fluorescence quantum yield in the solid state (approx. 40 – 50 %) and the fully amorphous solid state structure, it is currently one of the conjugated polymers with the highest gain value for stimulated emission. MeLPPP is an ideal candidate for basic energy transfer studies in inorganic-organic hybrid devices [74]. The absorption band is well resolved without significant inhomogeneous broadening with a (0-0) absorption maximum centered around 450 nm. The fluorescence emission peak (0-0) shows a

very small Stokes-shift (approx. 150 cm^{-1}) due to the very rigid ladder structure of the conjugated backbone. Due to the lack of self absorption in the spectral region > 470 nm the (0-1) emission band shows a much higher gain when compared to the higher energy (0-0) transition. MeLPPP has been extensively studied for its photo- and electroluminescence properties including its ASE and lasing behaviour in optically pumped solid state polymer lasers with DFB and DBR resonator geometry [74,87,95]. The photoluminescence spectrum is shown in Figure 4.37.

4.4.3 Grating Design

Grating design is approximately as shown in Figure 4.38. In one dimension 2nd order Bragg reflection condition results surface normal emission, or scattering, of guided mode.

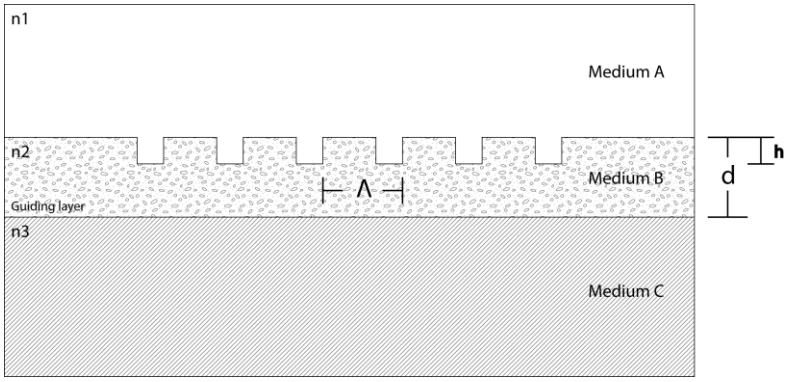

Figure 4.38: Asymmetric slab waveguide structure design parameters.

$$\Lambda = l \times \frac{\lambda_g}{2}, l = 1, 3, 5, \ldots \qquad \lambda_g = \frac{2\,\pi}{\beta} = \frac{\lambda}{\mathrm{n_{eff}}}$$

Effective index of MeLPPP film is calculated analytically as in Figure 4.39. As a result polymer thickness of 150 nm seemed to be optimized thickness.

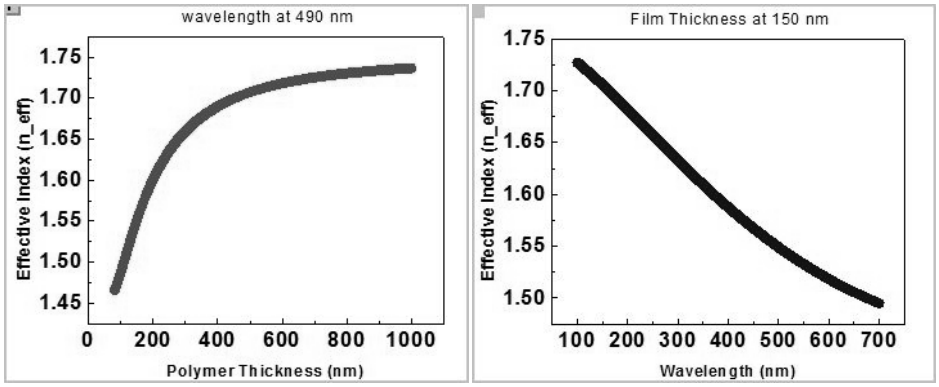

Figure 4.39: Effective index as functions of polymer thickness (left, for 490 nm light) and wavelength (right, for 150 nm slab thickness)

One method for enhancing photonic crystal action on SiO_2 surface for laser cavity, is using a high index material such as TiO_2 between SiO_2 and MeLPPP film. This thin layer increases the confinement of mode in polymer film.

We sputtered TiO_2 films on Si substrates and measured their refractive indices. The following Figure 4.40 shows the refractive index data and AFM image. The film parameter and quality meets our expectations.

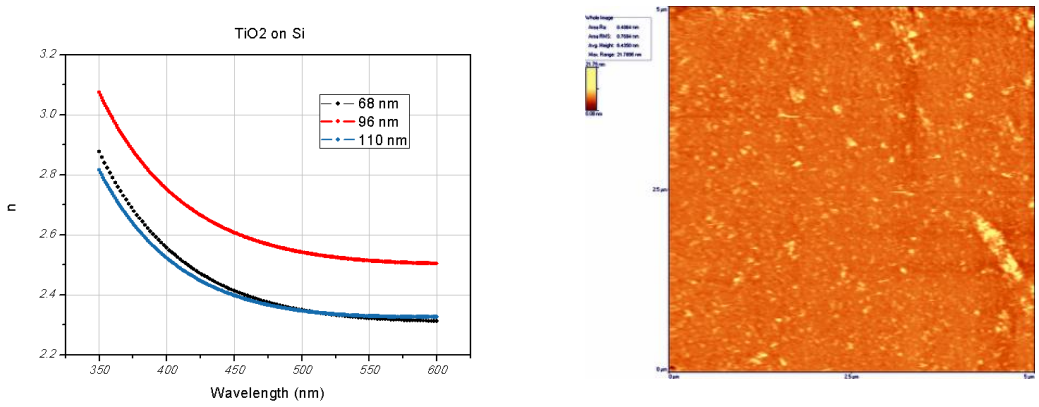

Figure 4.40: TiO_2 refractive index and AFM image, having RMS roughness 0.7 nm.

For Air/MeLPPP/SiO_2 based asymmetrical dielectric waveguide modeling, we performed FDTD simulations.

The simulation structure contains the following layers from top to bottom as in Figure 4.41.

Air

MeLPPP having n=1.75 at 494 nm, thickness varies 50-400 nm

SiO2, n=1.467 at 494 nm, 500 nm thick

Ni/Au: 5/5 nm

GaN with known/extracted n-k spectrum

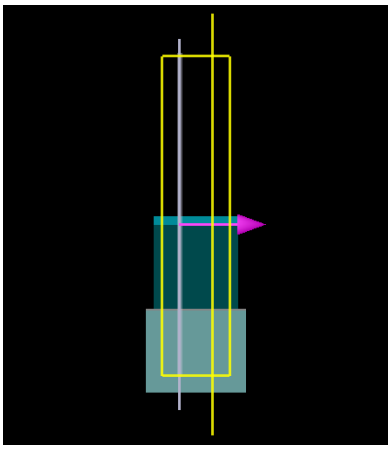

Figure 4.41: Simulation layout with injected mode source in horizontal-x direction.

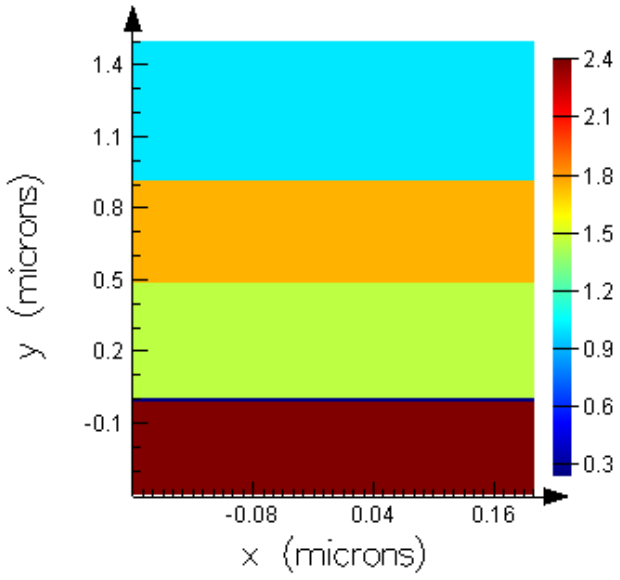

Figure 4.42: Refractive index distribution of simulation region.

In the Figure 4.42 effective index of propagating modes are shown as a function of film thickness. Since refractive index of polymer is 1.75, and of SiO_2 is 1.46, the mode is confined in film as the thickness increases. After ~150 nm, a TE mode is also supported, and after ~275 nm 2nd TM mode is started to propagate.

Actually, the asymmetric dielectric waveguide theory is straightforward, however, we took into account the extra layers below SiO_2, namely thin Ni/Au p-metal and InGaN/GaN layers, shown in Figure 4.43. Later on, as we use TiO_2 high index layer, these simulations will be of great help to analyze further.

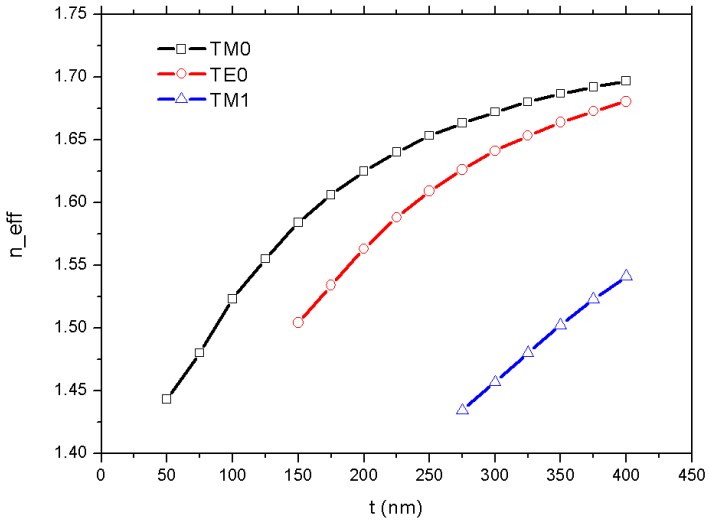

Figure 4.43: Effective index of first 3 modes at 494 nm of waveguide as a function of polymer film thickness.

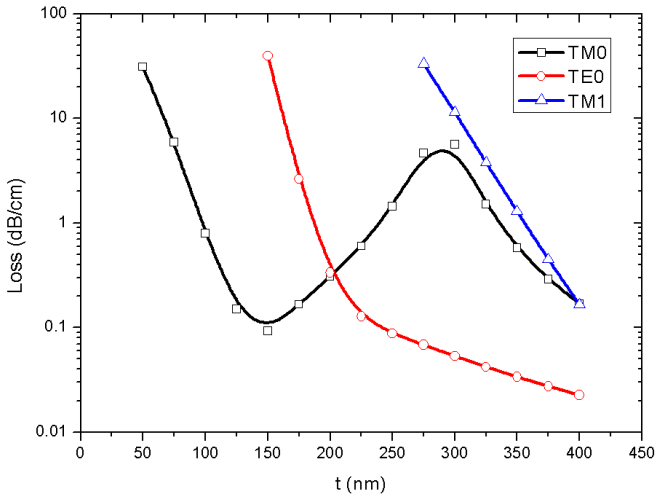

Figure 4.44: Losses of 3 modes as a function of film thickness.

In Figure 4.44, the loss coefficient of modes are shown. Interesting point here is that, after 150 nm film thickness, 0^{th} order TM mode loss increases, meaning that,

energy is being transferred into the 1st order TM mode. This is not acceptable for our case. We wish to have as much efficiency as possible, due to possible low exciation power coming from LED. Design should include bits and pieces of laser efficiency. It is apparent that ~150 nm film thickness is required for the efficient operation.

Previously we mentioned that typical cavity structures are to be designed from 2nd order Bragg grating based structures (feedback grating geometries). The absorption energy of MeLPPP polymer is at 2.71 eV (wavelength: 457 nm), and emission is at 2.51 eV (wavelength: 494 nm). The structures should be designed so that they have periods according to the mode's effective index.

In the following figures, the mode profiles and time snapshots of modes at steady state are given. As thickness increases, mode is propagating more in MeLPPP layer (n_{eff} increases.) This phenomenon is also clearly visible in time snapshots of modes.

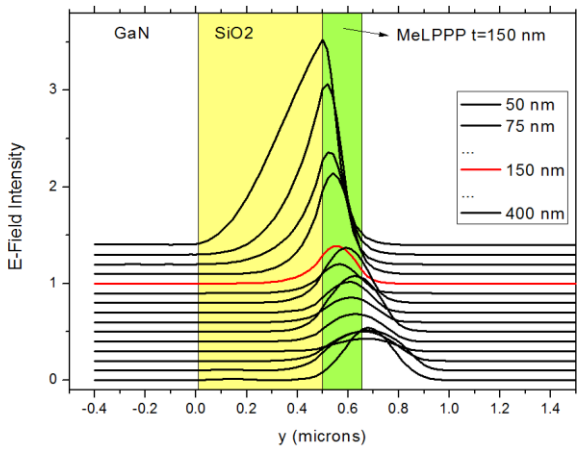

Figure 4.45: Mode profile evolution as a function of film thickness for 0th order TM mode. E-field intensities are shifted for easy viewing.

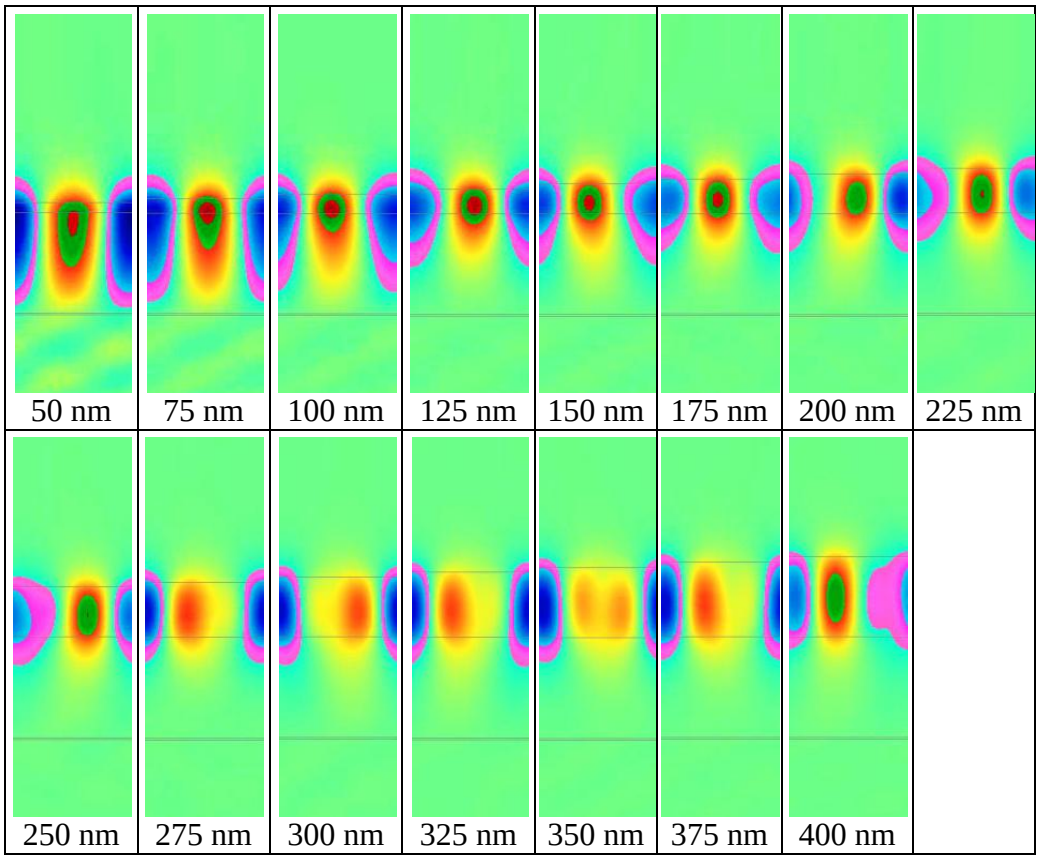

Figure 4.46: Snapshots of 0^{th} order TM mode as a function of MeLPPP film thickness. Shown here is E_z component for TM mode (z-directed out of page).

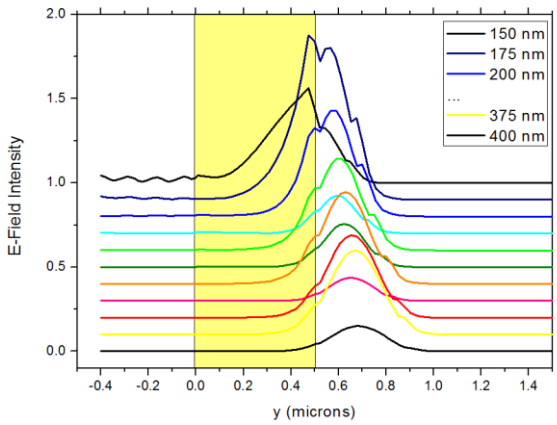

Figure 4.47: Mode profile evolution as a function of film thickness for 0th order TE mode.

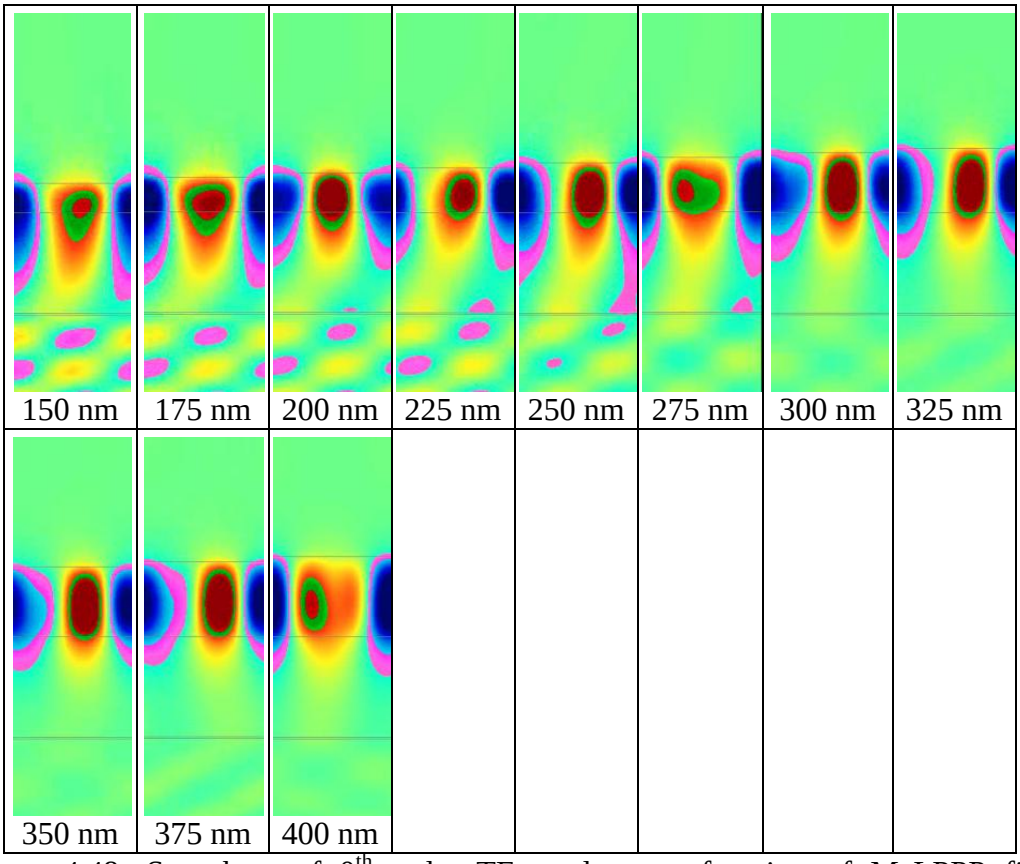

Figure 4.48: Snapshots of 0th order TE mode as a function of MeLPPP film thickness. Shown here is Hz component for TE mode (z-directed out of page).

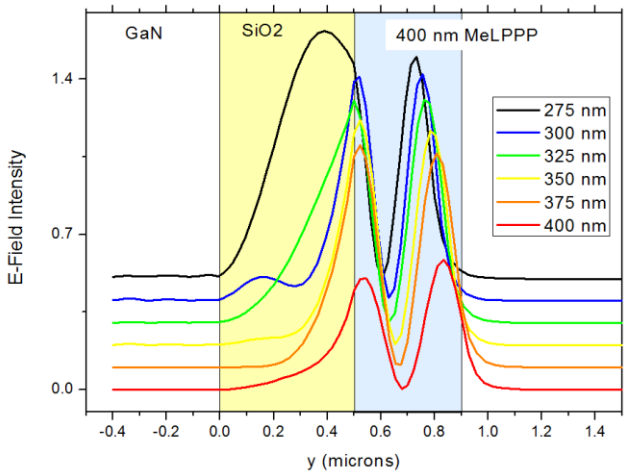

Figure 4.49: Mode profile evolution as a function of film thickness for 1st order TM mode.

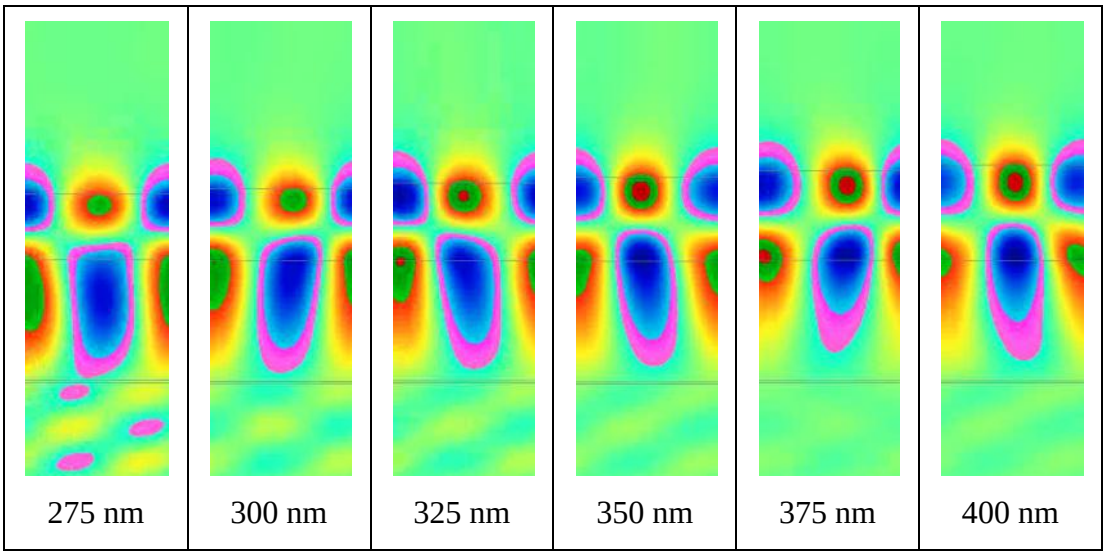

Figure 4.50: Snapshots of 1st order TM mode as a function of MeLPPP film thickness. Shown here is Ez component for TM mode (z-directed out of page).

4.4.4 Grating Process: Focused Ion Beam and e-Beam Lithography

The fabrication of the gratings on the GaN LED's top electrode was performed at ICFO in Barcelona, by using FIB system (FEI Strata DB235). A very thin layer of Au was evaporated on top of the devices in order to prevent charging effects. We fabricated one dimensional linear gratings of an area approx. 100 x 100 μm^2 by FIB milling, partially covering the LED surface (Figure 4.51). The gratings had 50 nm deep trenches with periods of Λ=300 nm and 310 nm. The milling time was approx. 2-to-3 hour long for a single patterning of 100x100 μm^2, using currents in the order of 100 pA.

The organic polymer was dissolved in toluene with a concentration of ~25 mg/ml with the help of an ultrasound bath and spin coated on the surface of the LED device at 2500 rpm (for 30 s) resulting in a 150 nm thick organic layer. The thickness of the organic layer was selected to be $>\lambda/2n$ of the emission wavelength of interest (~490 nm) to obtain an asymmetric waveguide, supporting only the first mode. The photoluminescence spectrum of the MeLPPP layer on top of sapphire substrate was shown in Figure 4.19. Three distinct emission peaks are present at wavelengths 460, 490 and 525 nm.

4.4.5 Results

Figure 4.51 shows the schematic structure of the complete device. The MeLPPP polymer (n=1.75) layer was sandwiched between air and a 450 nm-SiO_2 (n=1.46) layer in an asymmetric waveguide structure. In comparison to SiO_2, ITO shows a much higher refractive index of 2.05. The refractive index of GaN is ~2.35. Therefore, the SiO_2 layer should be as thick as possible in order to prevent evanescent wave losses. Emitted light corresponding to Bragg wavelength of 490 nm will be decoupled to air through the distributed feedback (DFB) grating. An SEM image of the SiO_2-based DFB grating is shown in Figure 4.51(b) demonstrating a highly uniform grating structure, which is rather important for a high light output of the device.

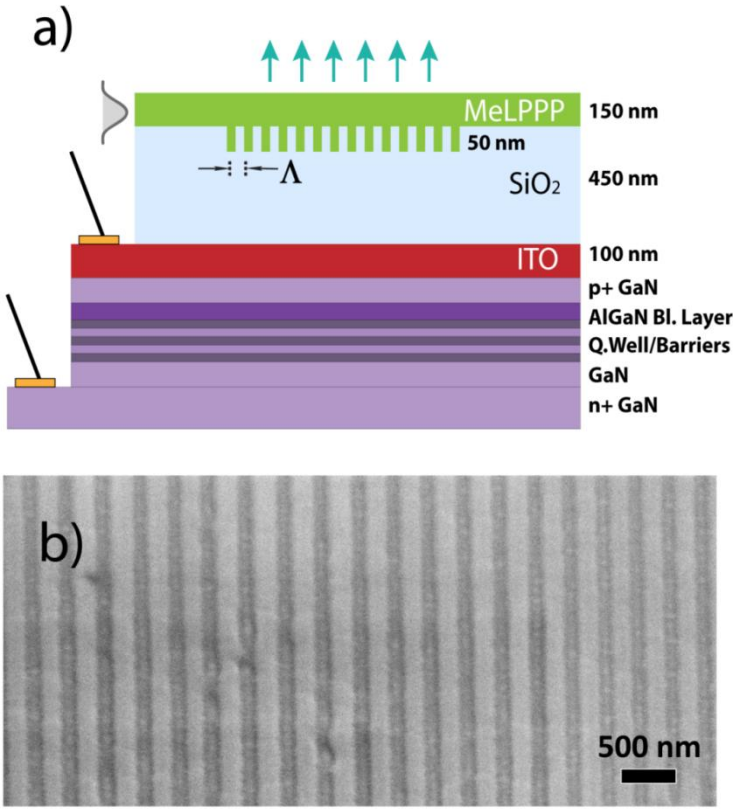

Figure 4.51: (a) Schematic diagram of a fabricated LED structure, SiO_2 DFB grating with MeLPPP layer. (b) SEM image of a patterned area after FIB milling process with a grating period of 310 nm.

In Figure 4.52(a), a CCD image of an LED device is shown under 6 V bias and 9 mA current. The white areas on the device mesa show that the combination of blue LED emission and optically pumped MeLPPP luminescence effectively produces a broad spectrum, mostly covering the blue and green components, which otherwise would be white light. The grating region in the middle of the device is not clearly visible since the image is mainly dominated by the LED emission. The far field image of the same sample without a filter is shown in Figure 4.52(b). Here, the GaN-LED emission is also apparent from the edges of the device due to the total internal

reflection. A similar image through a high-pass filter with cut-off at 400 nm is shown in Figure 4.52(c). The 390 nm emission of the LED is now blocked with the filter. The emitted light now originates from the organic layer indicating a uniform absorption of the LED emission by the organic layer. We performed transmission and reflection measurements of MeLPPP/SiO_2 (150 nm/450 nm) coated sapphire samples using Ocean Optics spectrometer around 400 nm. We obtained the absorption of polymer film approximately 12 %. Since ideally a complete absorption by the polymer would be preferred, either a thicker MeLPPP layer or a pump LED with an emission near the absorption maximum of MeLPPP (~450 nm) should be utilized.

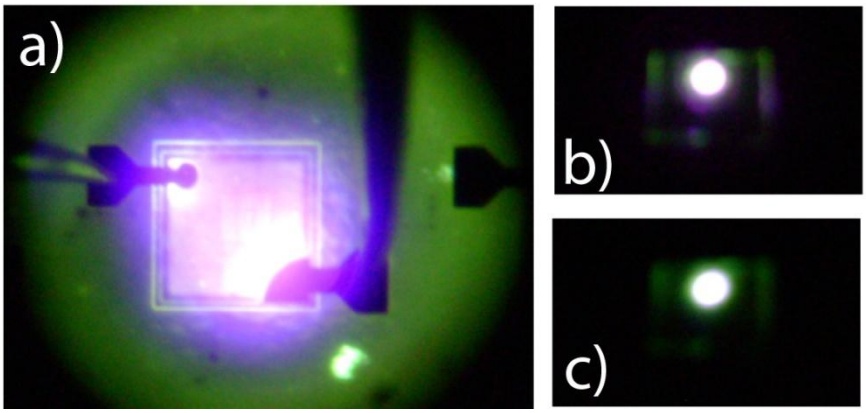

Figure 4.52: (a) Photograph of a hybrid LED device in electroluminescence, (b) far-field image (c) and far-field image with a 400 nm-cut-off high pass filter.

To characterize the hybrid devices, we performed electroluminescence (EL) and photoluminescence (PL) measurements on the patterned and non-patterned areas and with/without spin-coated organic material. Emission from the grating was collected with a 125 μm diameter multimode fiber probe connected to a spectrometer in the wavelength range of 400-650 nm.

We first performed photoluminescence measurements on the hybrid device with a grating period of 310 nm. We optically pumped the MeLPPP layer close to the grating with a 325 nm continuous wave (CW) HeCd laser and collected the decoupled light with the fiber probe.

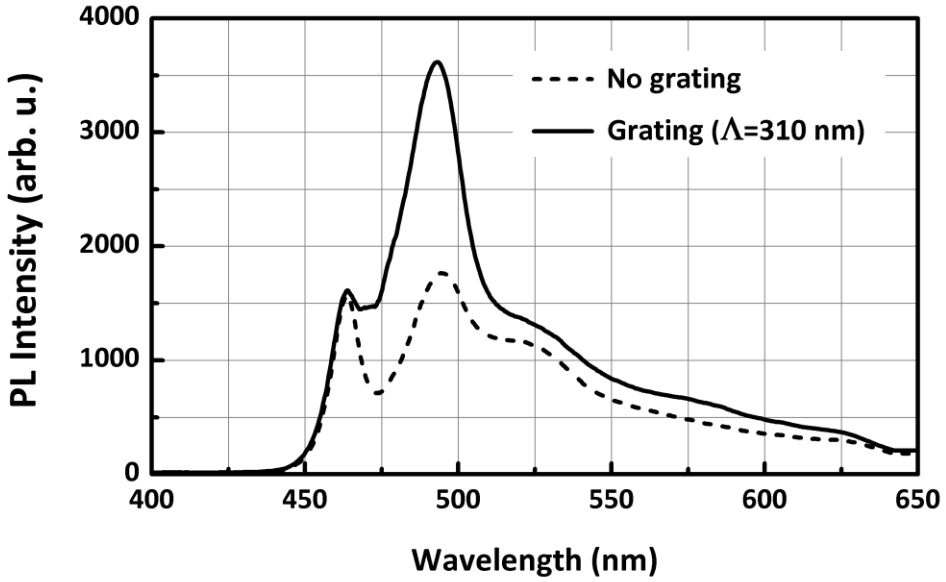

Figure 4.53: PL of a hybrid LED device with a grating period of 310 nm using a fiber probe for light collection.

Figure 4.53 shows the PL spectra of hybrid LED device without grating and with 310 nm periodicity grating. We observed a 2.06-fold increase in the intensity of the (0-1) MeLPPP emission band (490 nm emission peak) within the grating region. The Bragg condition is given as $\Lambda = m\lambda/2n_{eff}$, where Λ is the grating period, m is the order of the grating and λ is the Bragg wavelength. n_{eff} denotes the effective refractive index of the supported waveguide mode. In this work, we utilized second

order Bragg grating, to have a vertical emission of light. In order to match the 2nd order Bragg condition with the equation **[**76**]** $\Lambda=\lambda/n_{eff}$ the grating period should be around Λ=314 nm. We calculated n_{eff} to be around 1.57 using the device parameters, thicknesses of the organic and dielectric layers and grating depth and periods [96]. For a grating with a periodicity of 310 nm, the Bragg wavelength corresponds to 487 nm, which clearly is within the (0-1) emission band.

We then performed electroluminescence measurements. We applied voltage to the LED device and measured light outgoing from the organic surface. Here, the idea is to use the inorganic light emitting device to convert its emission energy down to higher wavelengths, namely the wavelength of the (0-1) emission band of the conjugated polymer MeLPPP. The EL spectra of devices without and with a grating period of 310 nm is given in Figure 4.54. Different from the PL spectra, we observed another emission wavelength that is around 400 nm. This corresponds to the emission of the GaN-LED structure as plotted in Figure 4.19. It is apparent that a part of the GaN UV emission is converted down to the lower energy MeLPPP emission region. The LED structure has an emission peak at 390 nm and MeLPPP absorbs the light at 390 nm and emits at higher wavelengths. LED emission was measured to be considerably higher than the MeLPPP emission due to low absorption of thin polymer film (%12). LED emission could be suppressed by using thicker organic polymer films. This result shows the feasibility of incorporating inorganic light emitting sources with organic materials in order to produce hybrid light emitting devices. It is worthy of note that the device does not yield lasing in the polymer. The long-wavelength emission bands in MeLPPP especially in electroluminescence have been related to the formation of keto defect states in photo- or electro-oxidatively degraded MeLPPP layers that act as charge and exciton traps [97].

The electroluminescence enhancement in the region of the MeLPPP emission for a grating period of 310 nm and a surface depth of 50 nm is illustrated in Figure 4.54. The enhancement factor at 490 nm is measured to be 1.85. We also observed

EL enhancement at longer wavelengths (> 520 nm), but the amount enhancement is not significant compared to the wavelengths of interest (around 490 nm). The fluorescence component at higher wavelength is caused by energy transfer (Foerster transfer) of the initial excitation to emissive keto defects. Enhancement in the emission at longer wavelengths may be related to the coupling of both processes (fluorescence enhancement and energy transfer). The enhancement factor could further be increased by matching the Bragg wavelength more exactly to the (0-1) emission peak of MeLPPP (490 nm). One could also fabricate deeper gratings in order to increase the amount of Bragg reflections taking place within the grating region.

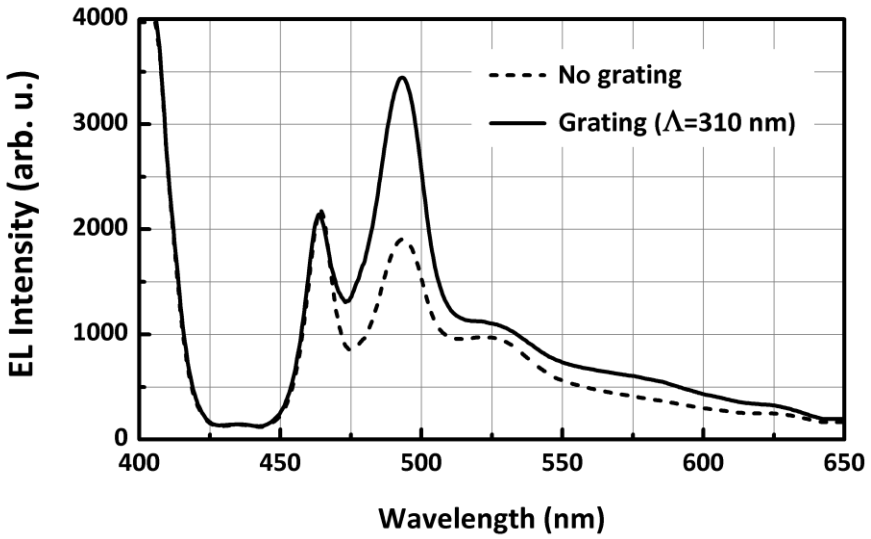

Figure 4.54: EL of the hybrid device with a grating period of 310 nm.

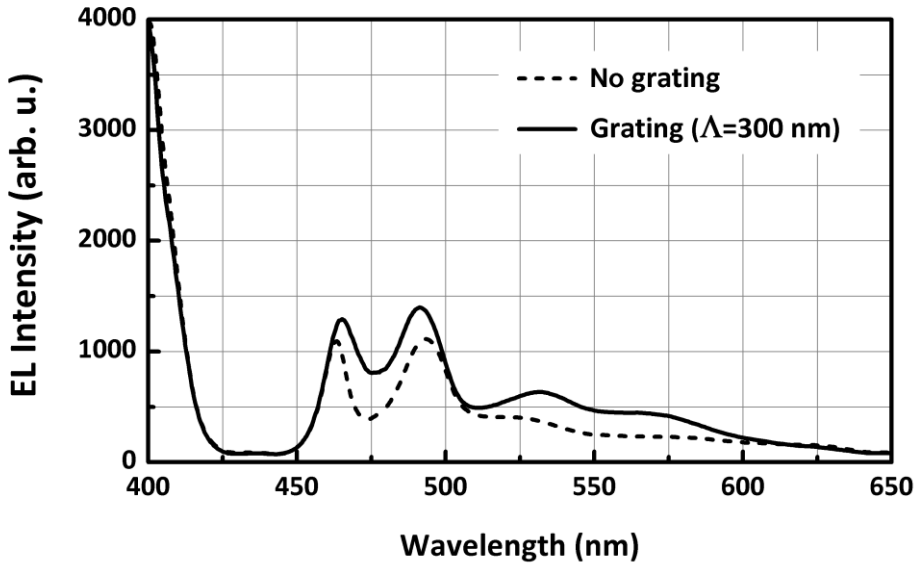

Figure 4.55: EL of the hybrid device with a grating period of 300 nm.

We also fabricated another device with a different periodicity of Bragg grating, 300 nm. In Figure 4.55, EL emission spectra from the grating and flat area (area on the diode mesa but outside the grating) was recorded for a grating period of 300 nm. For the emission at 490 nm wavelength the enhancement factor in the grating region was 1.27, amplification was also observed for higher wavelengths > 500 nm. This measurement shows that the increased deviation of the grating period from the preferred value (~314 nm) causes a decrease in the enhancement factor, as expected. The Bragg wavelength for a grating period of 300 nm is calculated to be 471 nm in the local minimum between the (0-0) and (0-1) emission features of MeLPPP. At shorter wavelengths outside the polymer emission feature the intensities of the emission bands with and without grating match perfectly indicating that the EL enhancement only exclusively originates from the DFB grating.

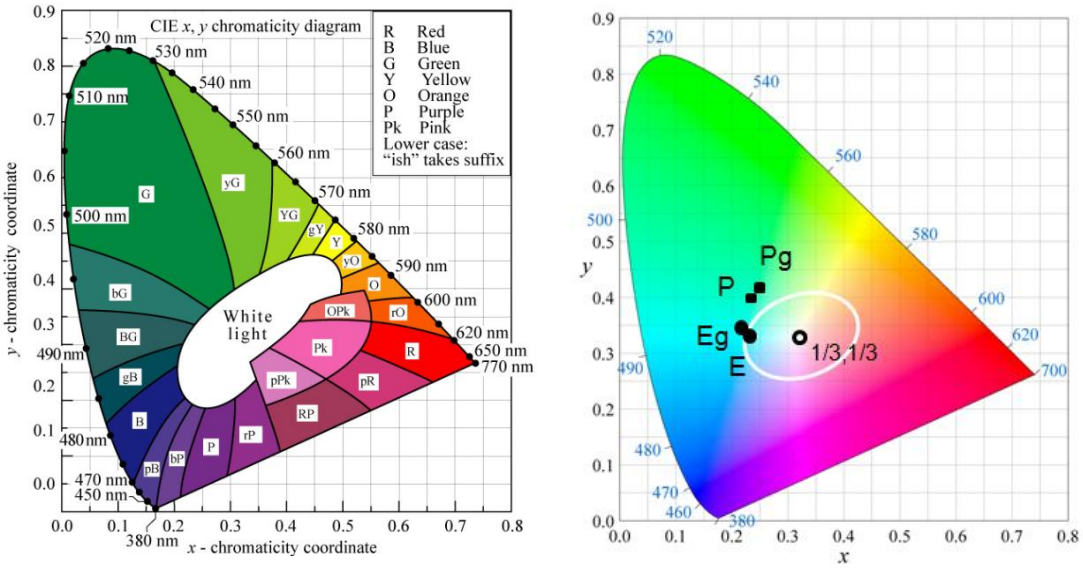

Figure 4.56: CIE Color chromaticity diagram [24, 98],. E: EL, Eg:EL on grating, P:PL, Pg:PL on grating.

Since we are extending a single wavelength emission from an LED to a wider spectrum using a coating it is helpful to locate the hybrid LED's white-lightness on chromaticity diagram, called CIE x-y chromaticity diagram as in Figure 4.56. This method relies on human eye's physiology and brain. A more complete treatment of different color indices can be found elsewhere [99, 100]. There are a few important point here to be mentioned regarding the diagram: i) circumference of color diagram represents the monochromatic, or laser, light sources, ii) x-y coordinates are obtained by integrating emission spectrum by three response curves of three different kinds of cone cells in the eye, iii) EL spectrum contains strong emission from LED at a wavelength where eye is not very sensitive, iv) emission does require a red component for being a true white light source. This is also apparent in the spectrum.

Required component can be obtained by using red chromophores, for example nanocrystal solutions mixed with organic polymer.

As a summary, we fabricated a high performance InGaN/GaN based LED with 390 nm emission and combined it with an emissive conjugated polymer (MeLPPP) nano-structured grating for wavelength down-conversion with high wavelength selectivity and out-coupling efficiency. The grating with 310 nm periodicity showed a nearly two-fold amplification factor for an emission wavelength of 490 nm corresponding to the (0-1) emission band of the polymer. We showed the feasibility of a compact hybrid light emitting device, which is electrically operated and may be easily modified for tunable wavelength emission, white light generation, and multimode operation. The structure combines the superior characteristics of electrical (LED) and optical (conjugated polymer MeLPPP) components for, most importantly, future compact laser sources for the UV-visible range based on DFB or DBR resonator structures.

Next, we worked on fabricating circular gratings using e-beam lithography tool, on SiO2 coated samples. The different samples consisted of 500 or 1000 nm SiO_2 coated on sapphire, quartz, TiO_2 coated sapphire, silicon and LED devices. Although LED devices showed no laser action, we observed scattering at 490 nm from MeLPPP coated SiO2 samples. In the following Figures 4.57-61, SEM and AFM images, and dark field optical microscope images are given. Period of grating is 318 nm, with effective index of 1.55, the wavelength of surface to normal scattering is between 450-490 nm. AFM measurement shows the grove having depth in the range 80-110 nm which is enough for laser action in future work.

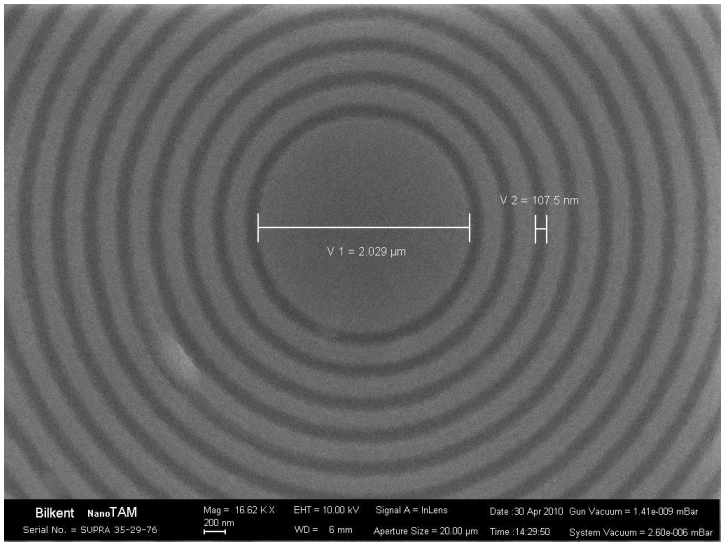

Figure 4.57: SEM image of circular grating structure. Central disk diameter is 6 times the period of grating.

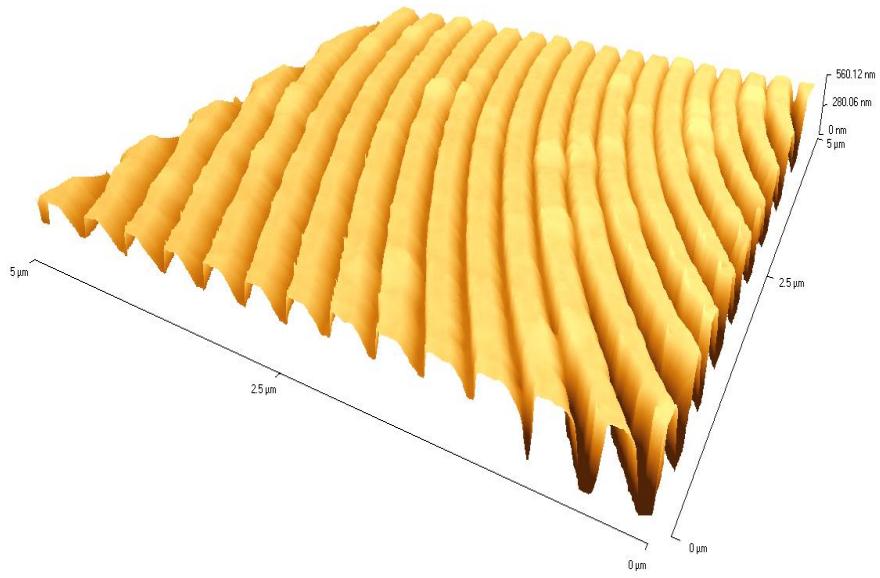

Figure 4.58: AFM image of gratings. Groove depth is close to 120 nm in this structure.

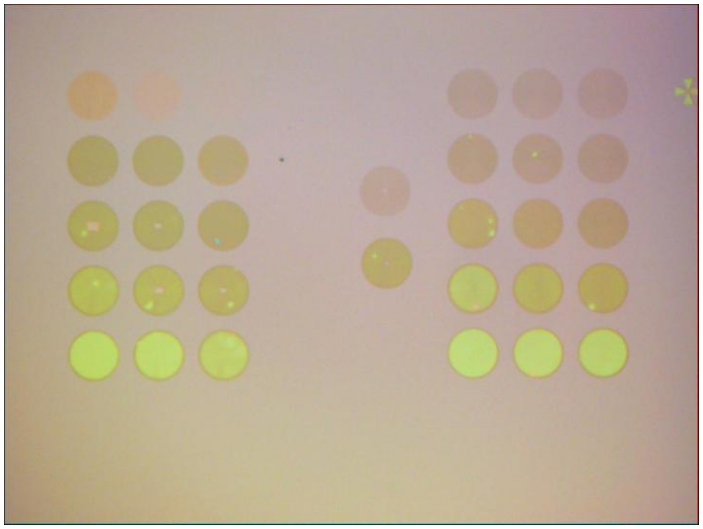

Figure 4.59: Bright field (normal mode) image of gratings under optical microscope.

In Figure 4.59, the color tone changing throughout array due to the different electron dose during lithography. This corresponds to different filling ratio of grooves in the grating.

Dark field image microscopy yields scattering response of surfaces, not reflection. In this case, for example epitaxial boundaries of LEDs, and grating structures are clearly seen which is not clear under bright field microscope operation.

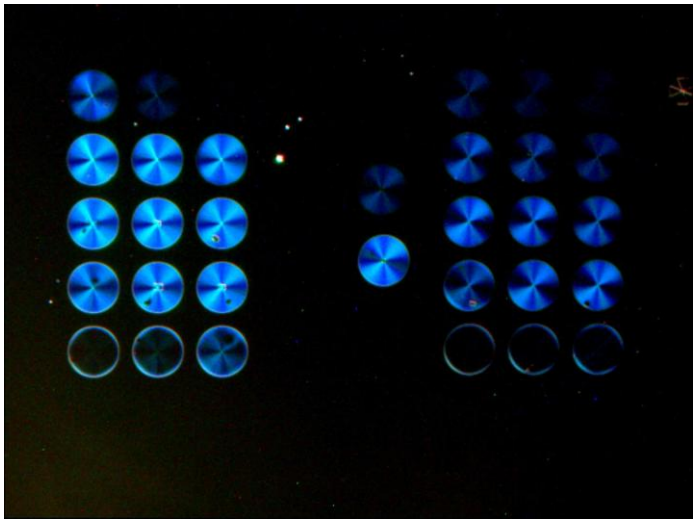

Figure 4.60: Dark field image of gratings under optical microscope.

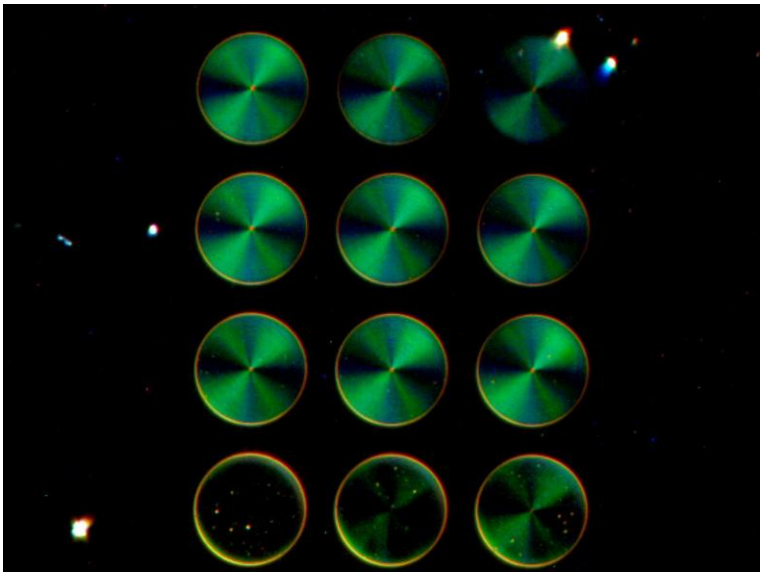

Figure 4.61: Dark field image of gratings in closer look.

The gratings' center scatters red light which is visible in Figure 4.61. This is due to large diameter of center disc, compared to the grating period. This way we made sure that gratings are fabricated successfully. Next work is to put these on LEDs to have normal mode laser action with hybrid structures mentioned above.

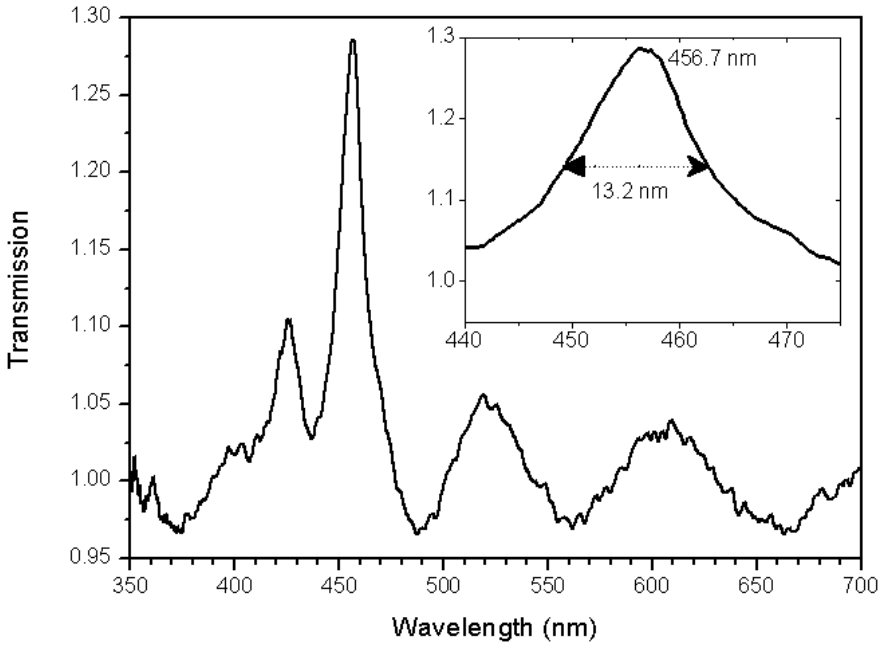

Figure 4.62: Transmission spectrum of grating structures illuminated by white light source.

Then, we coated TiO_2 coated and patterned sample with MeLPPP polymer. A solution with MeLPPP:Toluene =25mg:1.25ml is prepared, and spin coated on the sample 4000 rpm x 1s + 2275 rpm x 30 s. Resulting film thickness is measured by profilometer as 150±5nm from one corner of sample to the other, but within one grating area, the roughness is much smaller than 5 nm.

We illuminated grating structures by white light source and collected transmitted light from the other side, setup shown in Figure 4.31. As it is seen in Figure 4.62, at 456 nm, the collected light throughout the grating area are beamed to forward direction and scattered light is enhanced. Since this grating structures are in a way cavities for captured light, a Q factor can be calculated using the data given in Figure 4.62 by:

$$Q=f_0/\Delta f$$

where

$$\Delta f=\Delta\lambda\ c/\lambda_0^2.$$

Estimated Q-factor is found to be about 35, which shows quite a leaky waveguide for a circular cavity.

The estimated Q factor can be compared with simulations which are based on TMM analysis considering circular grating structures. Solution of Maxwell's equations for TE or TM modes in circularly symmetric geometry leads to Bessel function expansions. Applying boundary conditions on groove interfaces, which are simply continuity of tangential E and H fields for non-absorbing dielectric media, gives transfer matrices for each groove. This was developed similarly in Chapter 2 for 1D case, and more detailed treatment can be found in the literature [101, 102].

After this analysis, circular grating structure can be redesigned and measured for vertically emitting lasers or white-light sources with various coating ingredients.

Chapter 5

Conclusions and Suggestions for Further Research

III-Nitride based materials and devices are having very high potential for UV and visible wavelengths. Need for highly efficient detectors and light sources, may be modulators which exploit their performances similar to that of GaAs based devices will always be present. Therefore worldwide research efforts are concentrated into this area.

In the current thesis, detectors with high performances are fabricated in about 100 μm sizes. However, there is a need for smaller detectors for integrated optoelectronics, all optical circuits. They need to be compatible to photonic crystal and plasmonic components. Therefore these kind of devices need to be considered and be pursued in the future.

Similar need is valid for light sources too. The importance of detectors is equal to the importance of LEDs and lasers, because one is almost always completely useless without the other. Smaller, highly radiation efficient, low energy consuming and compatible with plasmonic and photonic crystal structures is an urgent need.

Space applications, worldwide energy concerns, white light sources and many similar areas are waiting for these devices.

From the subjects investigated in this thesis, nanopillar based photonic crystal LED structures may be the one that should certainly be pursued more in the future. It contains potentials for developing nano laser diodes, diode/laser arrays, all optical modulators utilizing nonlinear coatings, and optical multiplexing applications, to name a few.

Appendix A: TMM Simulation Program

TMM code for reflection, transmission and absorption calculations in 1D.

```
function tmm(medium_structure,acLayer,W1,W2)
% layered structure; absorbtion, reflection powers, etc. ;
% using Transfer Matrix Method
% NOTE: QEff calculation may need two air interfaces 0nm long
% at two sides of the active region.

%function [waveLength,PAbs,R]=tmm(medium_structure,acLayer,W1,W2)
%function [waveLength,R]=tmm(medium_structure,acLayer,W1,W2)

% USAGE
% m_in: surrounding medium code number; generally air
% m_out: exit material code number; air or substrate
% m#: layer code number
% d#: layer thickness in nm
% assume active layer is the kth layer
% ******************************************************
% tmm([m_in m1 d1 m2 d2 m3 d3 ... mn dn m_out],k,start_wavelength,stop_wavelength)
% ******************************************************



nod=1001;% number of points
acc=0;% active layer absorption calculation? (0=no, 1=yes)

Medium=medium_structure;
MedSize=length(Medium);

%put material codes into a vector.
Mat(1,1)=Medium(1,1);
for h=1:(MedSize/2)
   Mat(h+1,1)=Medium(2*h);
end
MatSize=length(Mat);

acL=acLayer;
%if acL>MatSize-2
%    error('active layer is not within the layers')
```

```
%end

%put layer thicknesses into a vector
dLayers(1)=0;
for z=1:(MedSize/2-1)
   dLayers(z+1)=Medium(2*z+1);
end



% take the n values of layer materials,
% corresponding to number_of_points_much wavelengths
% given within the interval [W1,W2].
[waveLength,N,W1,W2]=nval(nod,Mat,W1,W2);

% create the PT, PA, PR, QEff vectors.
Rs=zeros(length(waveLength),1);
Trs=Rs;

for s=1:length(waveLength),

   %initialise the Transfer matrices
   T=eye(2,2);
   T1=T;
   T2=T;

   for m=1:(MatSize-1),

      T=T*TMatrix(waveLength(s),dLayers(m),N(s,m),N(s,m+1));

      if acc,
         if m==acL,
            T1=T*inv(TMatrix(waveLength(s),0,N(s,m),N(s,m+1)));
            n1=N(s,m);
         end
         if m==acL+1,
            T2=T;
            n2=N(s,m+1);
         end
      end
   end



   %now process is at the last medium, which was
   % assumed to be infinite.

   A=T(1,1);
   B=T(1,2);
   C=T(2,1);
   D=T(2,2);

   %find reflected and transmitted E fields.

   nIn=N(s,1);
   nOut=N(s,MatSize);
   G=1; %a constant; normally 1/377 ohms.

   Et=1/A;
   Er=C*Et;
```

```
    %Pi=G*(1)^2;
    %Pr=G*(abs(Er))^2;
    %Pt=G*(abs(Et))^2;

    Pi=G*abs(nIn)*(1)^2;
    Pr=G*abs(nIn)*(abs(Er))^2;
    Pt=G*abs(nOut)*(abs(Et))^2;

     %quantum eff. at the active layer
     if acc,
       MM1=inv(T1)*[1;Er];
       EinAcf=MM1(1,1);
       EinAcb=MM1(2,1);
       MM2=inv(T2)*[1;Er];
       EoutAcf=MM2(1,1);
       EoutAcb=MM2(2,1);

       %PinAcf=G*(abs(EinAcf))^2;
       %PinAcb=G*(abs(EinAcb))^2;
       %PoutAcf=G*(abs(EoutAcf))^2;
       %PoutAcb=G*(abs(EoutAcb))^2;

       PinAcf=G*abs(n1)*(abs(EinAcf))^2;
       PinAcb=G*abs(n1)*(abs(EinAcb))^2;
       PoutAcf=G*abs(n2)*(abs(EoutAcf))^2;
       PoutAcb=G*abs(n2)*(abs(EoutAcb))^2;
       PAbs(s)=(PinAcf+PoutAcb-PinAcb-PoutAcf)/Pi;
     end

      %reflectance and transmittance on whole medium
      R(s)=Pr/Pi;
      Tr(s)=Pt/Pi;

       %ABSs(s,1)=1-Rs(s,1)-Trs(s,1);
       %Resp(s)=PAbs(s)*waveLength(s)/(1.24*1000);

end

%Total=R+Tr+PAbs;


%[waveL1,abs1]=textread(['C:\work\ganpin.txt'],'%f %f', -1);% to be used
% for comparison



plot(waveLength,R,'b-','LineWidth',3)
hold on
plot(waveLength,PAbs,'r-','LineWidth',3)
plot(waveLength,Tr,'k-','LineWidth',2)
hold off
axis([W1 W2 0 1])
xlabel('Wavelength (nm)','FontSize',14)
ylabel('-','FontSize',14)
grid on
%legend('measurement','simulation',2)
legend('reflection','absorption','transmission',2)
```

```
function [waveLength,NN,W1,W2]=nval(point,materialvector,W1,W2)
% W1 beginning wavelength value
% W2 ending wavelength value


%given material vector and #of data points
%takes the material n,k values and returns all n, k in two matrices.

waveLength=(linspace(W1,W2,point))';

%construct n k vectors
for m=1:length(materialvector),
   [A,B,C]=data(materialvector(m));
   N(:,m)=pchip(A,B,waveLength);
   K(:,m)=pchip(A,C,waveLength);
end
NN=complex(N,-K);
```

```
function T=TMatrix(lambda,d, ncurr,nnext)
% transmission matrix of slab with thickness d
t=2*ncurr/(ncurr+nnext);
r=(ncurr-nnext)/(ncurr+nnext);
delta=2*pi*ncurr*d/lambda;
T=(1/t).*[exp(i*delta)  r*exp(i*delta) ; r*exp(-i*delta)  exp(-i*delta)];
```

```
function v=dbr2(med1, d1, med2, d2, noOfLay)
% given two materials and their thicknesses and #of layers
% creates a DBR vector. with air insides
% accepts x.5 pair.

n=floor(noOfLay);
for k=1:n,
   v(1,8*k-7)=med1;
   v(1,8*k-6)=d1;
   v(1,8*k-5)=1;
   v(1,8*k-4)=0;
   v(1,8*k-3)=med2;
   v(1,8*k-2)=d2;
   v(1,8*k-1)=1;
   v(1,8*k)=0;
end
if mod(noOfLay,1)==0.5,
   v(1,8*n+1)=med1;
   v(1,8*n+2)=d1;
   v(1,8*n+3)=1;
   v(1,8*n+4)=0;
end
```

```
function [waveL,n,k]=data(materialno)
%gives wave length versus n and k values of given numbered
%material.
```

```
if materialno==0,
   [waveL,n,k]=textread('database/dummy.dat','%f %f %f', -1);
elseif materialno==1,
   [waveL,n,k]=textread('database/air.dat','%f %f %f', -1);
elseif materialno==2,
   [waveL,n,k]=textread('database/al.dat','%f %f %f', -1);
elseif materialno==7,
   [waveL,n,k]=textread('database/al20gan.dat','%f %f %f', -1);
elseif materialno==10,
   [waveL,n,k]=textread('database/aln.dat','%f %f %f', -1);
elseif materialno==12,
   [waveL,n,k]=textread('database/au.dat','%f %f %f', -1);
elseif materialno==14,
   [waveL,n,k]=textread('database/gan.dat','%f %f %f', -1);
elseif materialno==24,
   [waveL,n,k]=textread('database/ito.dat','%f %f %f', -1);
elseif materialno==28,
   [waveL,n,k]=textread('database/sapphire.dat','%f %f %f', -1);
elseif materialno==29,
   [waveL,n,k]=textread('database/si.dat','%f %f %f', -1);
elseif materialno==30,
   [waveL,n,k]=textread('database/si3n4.dat','%f %f %f', -1);
elseif materialno==31,
   [waveL,n,k]=textread('database/sin.dat','%f %f %f', -1);
elseif materialno==32,
   [waveL,n,k]=textread('database/sio.dat','%f %f %f', -1);
elseif materialno==33,
   [waveL,n,k]=textread('database/sio2.dat','%f %f %f', -1);
elseif materialno==36,
   [waveL,n,k]=textread('database/quartz.dat','%f %f %f', -1);
elseif materialno==37,
   [waveL,n,k]=textread('database/glass.dat','%f %f %f', -1);
else
   error('material data is not found in the data base')
end
```

Appendix B: List of Publications

1. **B. Butun**, K. Aydin, E. Ulker, S. Cheylan, G.Badenes, M. Forster, U. Scherf, and E.Ozbay, "A hybrid light source with integrated inorganic light-emitting diode and organic polymer distributed feedback grating," *Nanotechnology*, vol. 19, 195202 (2008).
2. **B. Butun**, T. Tut, E. Ulker, T. Yelboga, and E. Ozbay "High-performance visible-blind GaN-based p-i-n photodetectors," *Applied Physics Letters*, vol. 92, 033507 (2008).
3. **B. Butun**, J. Cesario, S. Enoch, R. Quidant and E. Ozbay, "InGaN green light emitting diodes with deposited nanoparticles," *Photonics and Nanostructures*, vol. 5, 86 (2007).
4. T. Tut, **B. Butun**, M. Gokkavas, and E. Ozbay, "High performance AlGaN-based avalanche photodiodes," *Photonics and Nanostructures*, vol. 5, 140 (2007).
5. T. Tut, M. Gokkavas, **B. Butun**, S. Butun, E. Ulker, and E. Ozbay, "Experimental evaluation of impact ionization coefficients in $Al_xGa_{1-x}N$ based avalanche photodiodes," *Applied Physics Letters*, vol. 89, 183524 (2006).
6. M. Gokkavas, S. Butun, H.B. Yu, T. Tut, **B. Butun**, and E. Ozbay, "Dual-color ultraviolet metal-semiconductor-metal AlGaN photodetectors," *Applied Physics Letters*, vol. 89, 143503 (2006).

7. S. Butun, T. Tut, **B. Butun**, M. Gokkavas, H.B. Yu, and E. Ozbay, "Deep-Ultraviolet $Al_{0.75}Ga_{0.25}N$ Photodiodes with Low Cut-off Wavelength and Low Leakage Current," *Applied Physics Letters*, vol. 88, 123503 (2006).
8. T. Tut, S. Butun, **B. Butun**, M. Gokkavas, H.B. Yu, and E. Ozbay, "Solar-blind AlGaN-based avalanche photodiodes," *Applied Physics Letters*, vol. 87, 223502 (2005).
9. N. Biyikli, I. Kimukin, **B. Butun**, O. Aytur, and E. Ozbay, "ITO-Schottky Photodiodes for High-Performance Detection in the UV–IR Spectrum", *IEEE Journal of Selected Topics in Quantum Electronics*, vol. 10, issue 4, p. 759 (2004).
10. **B. Butun**, N. Biyikli, I. Kimukin, O. Aytur, and E. Ozbay "High-speed 1.55 mm operation of low-temperature-grown GaAs-based resonant-cavity-enhanced p–i– n photodiodes," *Applied Physics Letters*, vol. 84, 4185 (2004).
11. Kimukin, N. Biyikli, **B. Butun**, O. Aytur, and E. Ozbay, "InGaAs Based High Performance p-i-n Photodiodes," *IEEE Photonics Technology Letters*, vol. 14, 366 (2002).

Bibliography

[1] www.plunkettresearch.com/Telecommunications/TelecommunicationsStatistics/tabid/96/Default.aspx, last accessed on 07.08.2010.

[2] D. Ehrentraut, E. Meissner, M. Bockowski, Eds., "Technology of Gallium Nitride Crystal Growth," Springer (2010).

[3] J. Orton, "The Story of Semiconductors," Oxford University Press (2004).

[4] F. Ren and J. C. Zolper, "Wide Energy Bandgap Electronics," World Scientific (2003).

[5] S. J. Pearton, Cammy R. Abernathy and F. Ren, "Gallium Nitride Processing for Electronics, Sensors and Spintronics," Springer (2006).

[6] http://apps.isiknowledge.com

[7] W. C. Johnson, J. B. Parson, M. C. Crew, J. Phys. Chem., 36, 2561 (1932).

[8] H.Morkoc, "Nitride Semiconductors and Devices," Springer (1999).

[9] Z. C. Feng, "III-Nitride Devices and Nanoengineering," Imperial College Press (2008).

[10] M. Razeghi, M. Henini, "Optoelectronic Devices: III-Nitrides," Elsevier-Oxford (2004).

[11] Muhammed A. Acar, "Fabrication, modeling and characterization of GaN HEMTs, and design of high power MMIC amplifiers," M.S. Thesis, Bilkent University, Department of Electrical and Electronics Engineering (2009).

[12] K. Takahashi, A. Yoshikawa, and A. Sandhu (eds.), "Wide bandgap semiconductors: Fundamental properties and modern photonic and electronic devices," Springer-Verlag, Berlin (2007).

[13] W. A. Harrison and J. Tersoff, "Tight-binding theory of heterojunction band lineups and interface dipoles," *J. Vac. Sci. Technol. B* **4**, 1068 (1986).

[14] J. Piprek (ed.), "Nitride Semiconductor Devices: Principles and Simulation," Wiley-VCH (2007).

[15] Y. N. Xu, W. Y. Ching, "Electronic, optical, and structural properties of some wurtzite crystals," *Phys Rev. B* **48**, 4335 (1993).

[16] M. Suzuki and T. Uenoyama, "Strain effect on electronic and optical properties of GaN/AlGaN quantum-well lasers," J. Appl. Phys. 80, 6868 (1996).

[17] B. Butun, "Low Temperature Grown GaAs Based Resonant Cavity Enhanced Photodiodes," M.S. Thesis, Bilkent University, Department of Electrical and Electronics Engineering (2004).

[18] B. A. E. Saleh, M. C. Teich, "Fundamentals of Photonics" Wiley-Interscience (1991).

[19] S. Donati, "Photodetectors: Devies, Circuits and Applications," Prentice Hall (1999).

[20] S. M. Sze, "Physics of Semiconductors," Wiley-Iterscience, 2nd ed. (1981).

[21] S. K. Ghandhi, "VLSI Fabrication Principles: Silicon and Gallium Arsenide", Wiley-Interscience 2nd ed. (1984).

[22] S. L. Chuang, "Physics of Optoelectronic Devices," Wiley-Interscience (1995).

[23] E. Ozbay, "Breaking world records in high speed microelectronics using resonant tunneling diodes and schottky photodiodes," PhD. Thesis, Stanford University (1992).

[24] E. F. Schubert, "Light Emitting Diodes," Cambridge Univ. Press (2006).

[25] H. P. Maruska and J. J. Tietjen, "The preparation and properties of vapour-deposited single-crystalline GaN," *Appl. Phys. Lett.* **15**, 327 (1969).

[26] H. Amano, M. Kito, K. Hiramatsu, and I. Akasaki, "P-type conduction in Mg-doped GaN treated with low energy electron beam irradiation (LEEBI)," *Jpn. J. Appl. Phys.* **28**, L2112 (1989).

[27] S. Nakamura, N. Iwasa, and M. Senoh "Method of manufacturing p-type compound semiconductor," US Patent 5306662 (1994).

[28] B. E. A. Saleh and M. C. Teich, "Fundamentals of Photonics," 2nd Ed., Wiley-Interscience (2007).

[29] M. Bass (Ed.), "Handbook of Optics," 2nd Ed., McGraw Hill (1995).

[30] E. Rosencher and B. Vinter, “Optoelectronics,”Cambridge Univ. Press (2004).

[31] S. M. Sze and K. K. Ng, “Physics of Semiconductor Devices,” 3rd Ed., Wiley Interscience (2007).

[32] http://cie.co.at/, last accessed on 01.06.2010.

[33] S. Nakamura, G. Fasol , “The Blue Laser Diode,” Springer (1997).

[34] H. Yu, M. K. Ozturk, S. Ozcelik, and E. Ozbay, “Optimization of semi-insulating GaN grown on an AlN/sapphire template by metalorganic chemical vapor deposition,” *Journal of Crystal Growth*, **293**, 273 (2006).

[35] H. Yu, W. Strupinski, S. Butun, E. Ozbay, "Mg-doped AlGaN grown on an AlN/sapphire template by metalorganic chemical vapour deposition," *Phys. Stat. Solidi A* **203** , 868 (2006).

[36] M. Razeghi and A. Rogalski, “Semiconductor ultraviolet detector*s,” J. Appl. Phys.* **79**, 7433 (1996).

[37] E. Ozbay, N. Biyikli, I. Kimukin, T. Tut, T. Kartaloglu, and O. Aytur, “High-Performance Solar-Blind Photodetectors Based on $Al_xGa_{1-x}N$ Heterostructures,” *IEEE J. Quantum Electron.* **10**, 742 (2004).

[38] S. J. Pearton, J. C. Zolper, R. J. Shul, and F. Ren, “GaN: Processing, defects, and devices,” *J. Appl. Phys.* **86**, 1 (1999).

[39] J. C. Campbell, S. Demiguel, F. Ma, A. Beck, X. Guo, S. Wang, X. Zheng, X. Li, J. D. Beck, M. A. Kinch, A. Huntington, L. A. Coldren, J. Decobert, and N. Tscherptner, “Recent advances in avalanche photodiodes,” *IEEE J. Select Topics Quantum Electron.* **10**, 777 (2004).

[40] N. Biyikli, I. Kimukin, T. Tut, O. Aytur, and E. Ozbay, "Solar-blind AlGaN-based Schottky photodiodes with low noise and high detectivity," *Appl. Phys. Lett.* **81**, 3272 (2002).

[41] N. Biyikli, I. Kimukin, O. Aytur, M. Gokkavas, M. S. Unlu, and E. Ozbay, "High-speed visible blind GaN-based indium tin oxide Schottky photodiodes," *Appl. Phys. Lett.* **79**, 2838 (2001).

[42] J. B. Limb, D. Yoo, J. H. Ryou, W. Lee, S. C. Shen, R. D. Dupuis, M. L. Reed, C. J. Collins, M. Wraback, D. Hanser, E. Preble, N. M. Williams, and K. Evans, "GaN ultraviolet avalanche photodiodes with optical gain greater than 1000 grown on GaN substrates by metal-organic chemical vapor deposition," *Appl. Phys. Lett.* **89,** 011112 (2006).

[43] B. Yang, T. Li, K. Heng, C. Collins, S. Wang, J. C. Carrano, R. D. Dupuis, J. C. Campbell, M. J. Schurman, and I. T. Ferguson, "Low dark current GaN avalanche photodiodes," *IEEE J. Quantum Electron.* **36**, 1389 (2000).

[44] K. A. McIntosh, R. J. Molnar, L. J. Mahoney, K. M. Molvar, N. Efremov, and S. Verghese, "Ultraviolet photon counting with GaN avalanche photodiodes," *Appl. Phys. Lett.* **76,** 3938 (2000).

[45] Q. Chen, J. W. Yang, A. Osinsky, S. Gangopadhyay, B. Lim, M. Z. Anwar, and M. Asif Khan, D. Kuksenkov and H. Temkin, "Schottky barrier detectors on GaN for visible–blind ultraviolet detection," *Appl. Phys. Lett.* **70,** 2277 (1997).

[46] W. Yang, T. Nohova, S. Krishnankutty, R. Torreano, S. McPherson, and H. Marsh, "Back-illuminated GaN/AlGaN heterojunction photodiodes with high quantum efficiency and low noise," *Appl. Phys. Lett.* **73,** 1086 (1998).

[47] J. C. Carrano, T. Li, D. L. Brown, P. A. Grudowski, C. J. Eiting, R. D. Dupuis, and J. C. Campbell, "Very high-speed metal-semiconductor-metal ultraviolet photodetectors fabricated on GaN," *Appl. Phys. Lett.* **73,** 2405 (1998).

[48] J.C. Carrano, T. Li, D.L. Brown, P.A**.** Grudowski, C.J. Eiting, R.D. Dupuis and J.C. Campbell, "High-speed pin ultraviolet photodetectors fabricated on GaN," *Electron. Lett.* **34,** 1779 (1998).

[49] N. Biyikli, I. Kimukin, T. Tut, T. Kartaloglu, O. Aytur, and E. Ozbay, "High-speed characterization of solar-blind AlxGa1-xN p-i-n photodiodes," *Semicond. Sci. Technol.* **19**, 1259 (2004).

[50] N. Biyikli, I. Kimukin, O. Aytur, and E. Ozbay, "Solar-blind AlGaN-based p-i-n photodiodes with low dark current and high detectivity," *IEEE Photon. Technol. Lett.* **16**, 1718 (2004).

[51] B. Butun, N. Biyikli, I. Kimukin, O. Aytur, and E. Ozbay, "High-speed 1.55 mm operation of low-temperature-grown GaAs-based resonant-cavity-enhanced p– i– n photodiodes," *Appl. Phys. Lett.* **84**, 4185 (2004).

[52] F. A. Ponce, and D. P. Bour, "Nitride-based semiconductors for blue and green light-emitting devices," *Nature* **386**, 351 (1997).

[53] M. Asif Kahn, M. Shatalov, H. P. Maruska, H. M. Wang, and E. Kuoktis, "III–Nitride UV Devices," *Jpn. J. Appl. Phys.* **44**, 7191 (2005).

[54] C. Huh, Kug-Seung Lee, Eun-Jeong Kang, and Seong-Ju Park, "Improved light-output and electrical performance of InGaN-based light-emitting diode by microroughening of the p-GaN surface," *J. Appl. Phys.* **93**, 9383 (2003).

[55] H. W. Huang, C. C. Kao, J. T. Chu, H. C. Kuom S. C. Wang and C. C. Yu, "Improvement of InGaN-GaN light-emitting diode performance with a nano-roughened p-GaN surface," *IEEE Photon. Tech. Lett.* **17**, 983 (2005).

[56] T. Nishida, H. Saito, and N. Kobayashi, "Efficient and high-power AlGaN-based ultraviolet light-emitting diode grown on bulk GaN," *Appl. Phys. Lett.* **79**, 711 (2001).

[57] S. M. Pan, R. C. Tu, Y. M. Fan, R. C. Yeh, and J. T. Hsu, "Improvement of InGaN-GaN light-emitting diodes with surface-textured indium-tin-oxide transparent ohmic contacts," *IEEE Photon. Tech. Lett.* **15**, 649 (2003).

[58] W. N. Carr, and G. E. Pittman, "One-watt GaAs p-n junction infrared source," *Appl. Phys. Lett.* **3**, 173 (1963).

[59] H. W. Choi, C. W. Jeon, C. Liu, I. M. Watson, M. D. Dawson, P. R. Edwards, R. W. Martin, S. Tripathy and S. J. Chua, "InGaN nano-ring structures for high-efficiency light emitting diodes," *Apl. Phys. Lett.* **86**, 021101 (2005) .

[60] H. G. Hong, S. S. Kim, D. Y. Kim, T. Lee, J. O. Song, J. H. Cho, C. Sone, Y. Park, T. Y. Seong, "Enhancement of the light output of GaN-based ultraviolet light-emitting diodes by a one-dimensional nanopatterning process," *Appl. Phys. Lett.* **88**, 103505 (2006).

[61] H. R. Stuart, and D. G. Hall, "Island size effects in nanoparticle-enhanced photodetectors," *Appl. Phys. Lett.* **73**, 3815 (1998).

[62] C. C. Kao, H. C. Kuo, H. W. Huang, J. T. Chu, Y. C. Peng, Y. L. Hsieh, C. Y. Luo, S. C. Wang, C. C. Yu, C. F. Lin, "Light-output enhancement in a nitride-based

light-emitting diode with 22° undercut sidewalls," *IEEE Photon. Tech. Lett.* **17**, 19 (2005).

[63] J. Vuckovic, M. Loncar, and A. Scherer, "Surface plasmon enhanced light-emitting diode," *IEEE J. Quantum Electron.* **36**, 1131 (2000).

[64] K. Okamoto, I. Niki, A. Shvartser, Y. Narukawa, T. Mukai, and A. Scherer, "Surface-plasmon-enhanced light emitters based on InGaN quantum wells," *Nature Materials*, **3**, 601 (2004).

[65] S. Pillai, K. R. Catchpole, T. Trupke, G. Zhang, J. Zhao, and M. A. Green, "Enhanced emission from Si-based light-emitting diodes using surface plasmons," *Appl. Phys. Lett.* **88**, 161102 (2006).

[66] I. Gontijo, M. Boroditsky, E. Yablonovitch, S. Keller, U. K. Mishra and S. P. DenBaars, "Coupling of InGaN quantum-well photoluminescence to silver surface plasmons," *Phys. Rev. B* **60**, 11564 (1999).

[67] E. Ozbay, "Plasmonics: Merging Photonics and Electronics at Nanoscale Dimensions," *Science*, **311**, 189 (2006).

[68] P. B. Johnson, and R. W. Christy, "Optical Constants of the Noble Metals," *Phys. Rev. B*, **6**, 4370 (1972).

[69] A. Liebsch, "Surface plasmon dispersion of Ag," *Phys. Rev. Lett*, **71**, 145 (1993).

[70] J. Cesario, R. Quidant, G. Badenes, and S. Enoch, "Electromagnetic coupling between a metal nanoparticle grating and a metallic surface," *Opt. Lett.* **30**, 3404 (2005).

[71] http://www.rsoftdesign.com/, last accessed on 01.06.2010.

[72] http://www.lumerical.com/, last accessed on 01.06.2010.

[73] B. Schweitzer, G. Wegmann, H. Giessen, D. Hertel, H. Bassler, R. F. Mahrt, U. Scherf, and K. Mullen, "The optical gain mechanism in solid conjugated polymers," *Appl. Phys. Lett.* **72**, 2933 (1998).

[74] U. Scherf, "Ladder-type materials," *J. Mater. Chem.* **9**, 1853 (1999).

[75] F. Hide, M. A. Díaz-García, B. J. Schwartz, M. R. Andersson, Q. Pei, and A. J. Heeger, "Semiconducting Polymers: A New Class of Solid-State Laser Materials," *Science* **273**, 1833 (1996).

[76] C. Bauer, H. Giessen, B. Schnabel, E.-B. Kley, C. Schmitt, U. Scherf, and R. F. Mahrt, "A surface-emitting circular grating polymer laser," *Adv. Mater.* **13**, 1161 (2001).

[77] F. Sobel, D. Gindre, J.-M. Nunzi, C. Denis, V. Dumarcher, C. Fiorini-Debuisschert, K. P. Kretsch, L. Rocha, "Multimode distributed feedback laser emission in a dye-doped optically pumped polymer thin-film," *Optical Materials* **27**, 199 (2004).

[78] J. Wang, T. Weimann, P. Hinze, G. Ade, D. Schneider, T. Rabe, T. Riedl, and W. Kowalsky, "A continuosly tunable organic DFB laser," *Microelectronic Eng.* **78-79**, 364 (2005).

[79] F. Hide, P. Kozody, S. P. DenBaars, and A. J. Heeger, "White Light Generation From InGaN/conjugated Polymer Hybrid Light-Emitting Diodes," *Appl. Phys. Lett.* **70**, 2664 (1997).

[80] F. Hide, S. P. DenBaars, and A. J. Heeger "Hybrid Light –Emitting Sources For Efficient And Cost Effective White Lightning And For Full-Color Applications," US Patent 5966393 (1999).

[81] G. Heliotis, P. N. Stavrinou, D. D. C. Bradley E. Gu, C. Griffin, C. W. Jeon, and M. D. Dawson , "Spectral conversion of InGaN ultraviolet microarray light-emitting diodes using fluorene-based red-, green-, blue-, and white-light-emitting polymer overlayer films," *Appl. Phys. Lett.* **87,** 103505 (2005).

[82] N. Tessler, G. J. Denton, and R. H. Friend, "Lasing from conjugated-polymer microcavities," *Nature* **382**, 695 (1996).

[83] C. Kallinger, M. Hilmer, A. Haugeneder, M. Perner, W. Spirkl, U. Lemmer, J. Feldmann, U. Scherf, K. Müllen, A. Gombert, and V. Wittwer, "A flexible conjugated polymer laser," *Adv. Mater.* **10**, 920 (1998).

[84] C. Bauer, H. Giessen, B. Schnabel, E.-B. Kley, C. Schmitt, U. Scherf, and R. Mahrt, "Realization of a circular-grating surface-emitting DBR laser with a polymeric emitter," *Adv. Mater.* **13**, 1161 (2003).

[85] J. Stehr, J. Crewett, F. Schindler, R. Sperling, G. von Plessen, U. Lemmer, J. M. Lupton, T. A. Klar, J. Feldmann, A. W. Hohleitner, M. Forster, and U. Scherf, "A low threshold polymer laser based on metallic nanoparticle gratings," *Adv. Mater.* **15**, 1726 (2003).

[86] C. Rothe, F. Galbrecht, U. Scherf, and A. Monkman, "The β-Phase of Poly(9,9-dioctylfluorene) as a Potential System for Electrically Pumped Organic Lasing," *Adv. Mater.* **18**, 2137 (2006).

[87] U. Scherf, S. Riechel, U. Lemmer, and R. Mahrt, "Conjugated Polymers: Lasing and Stimulated Emission," *Current Opinion in Solid State & Materials Science (COSSMS)* 5, 143 (2001).

[88] S. Nakamura, "InGaN-based blue light-emitting diodes and laser diodes," *J. Cryst. Growth* **202**, 290 (1999).

[89] A. E. Vasdekis, G. Tsiminis, J.-C. Ribierre, Liam O' Faolain, T. F. Krauss, G. A. Turnbull, and I. D. W. Samuel, "Diode pumped distributed Bragg reflector lasers based on a dye-to-polymer energy transfer blend," *Opt. Expr.* **14**, 9212 (2006).

[90] C. Karnutsch, C. Gaertner, V. Haug, U. Lemmer, T. Farrell, B. S. Nehls, U. Scherf, G. Heliotis, C. Pflumm, J. C. deMello, and D. D. C. Bradley, "Low threshold blue conjugated polymer lasers with first- and second order distributed feedback," *Appl. Phys. Lett.* **89**, 201108 (2006).

[91] T. Riedl, T. Rabe, H.-H. Johannes, W. Kowalsky, J. Wang, T. Weimann, P. Hinze, W. Nehls, T. Farrell, and U. Scherf, "Tunable organic thin-film laser pumped by an inorganic violet diode laser," *Appl. Phys. Lett.* **88**, 241116 (2006).

[92] G. A. Turnbull, P. Andrew, W. L. Barnes, and I. D. W. Samuel, "Operating characteristics of a semiconducting polymer laser pumped by a microchip laser," *Appl. Phys. Lett.* **82**, 313-315 (2003).

[93] H. B. Yu, M. K. Ozturk, S. Ozcelik, and E. Ozbay, "Optimization of semi-insulating GaN grown on an AlN/sapphire template by metalorganic chemical vapor deposition," *Journal of Crystal Growth* **293**, 273 (2006).

[94] B. Butun, J. Cesario, S. Enoch, R. Quidant, and E. Ozbay, "InGaN green light emitting diodes with deposited nanoparticles," *Photonics and Nanostructures: Fundamentals and Applications* **5**, 86 (2007).

[95] G. Lanzani, S. De Silvestri, G. Cerullo,S. Stagira, M. Nisoli, W. Graupner, G. Leising, U. Scherf, and K. Müllen, in *Semiconducting Polymers* ed. by G. Hadziioannou and P. F. van Hutten, Wiley-VCH: Heidelberg, 235 (1999).

[96] C. R. Pollock, "Fundamentals of Optoelectronics," Richard D. Irwin Inc.: USA (1995).

[97] L. Romaner, G. Heimel, H. Wiesenhofer, P. S. de Freitas, U. Scherf, J.-L. Brédas, E. Zojer, and E. J. W. List, "Ketonic Defects in Ladder-type Poly(p-phenylene)s," *Chem. Mater*. 16, 4667 (2004).

[98] http://en.wikipedia.org/wiki/CIE_1931_color_space, retrieved on 22.06.2010.

[99] R. G. Kuehni, "Color, An Introduction to Practice and Principles," Wiley-Interscience 2nd Ed. (2005).

[100] S. K. Shevell, Ed., "The Science of Color," Elsevier & OSA, 2nd Ed. (2003).

[101] R. Harbers, "Lasing in organic photonic-crystal structures," PhD. Thesis, University of Twente (2005).

[102] A. J. Bay, "Optical integrated devices with circular-grating resonators," Dissertation, ETH Zurich (2006).